INHIBITION OF ABL FAMILY KINASES PRODUCES A PROFOUND CHANGE IN CELL SHAPE AND MIGRATION

Zaozao Chen

A dissertation submitted to the faculty of the University of North Carolina at Chapel Hill in partial fulfillment of the requirements for the degree of Doctor of Philosophy in the Department of Cell Biology and Physiology.

Chapel Hill
2012

Approved by:

Ken Jacobson, Ph.D.

Keith Burridge, Ph.D.

James E. Bear, Ph.D.

Edward D. Salmon, Ph.D.

Maryna Kapustina, Ph.D.

ABSTRACT

ZAOZAO CHEN: Inhibition of Abl family kinases produces a profound change in cell
shape and migration.
(Under the direction of Ken Jacobson)

Cell migration is fundamental to establishing and maintaining the proper organization
of multi-cellular organisms. In this dissertation we reviewed and discussed the biological
process of single cell migration in two-dimensional and three-dimensional environments. We
reported that Gleevec (Imatinib), an Abl family kinase inhibitor, produces a profound change
in the shape and migration of rat bladder tumor cells (NBT-II) plated on collagen-coated
substrates. Cells treated with Gleevec adopt a highly spread D-shape (similar to fish
keratocytes) and migrate more rapidly with greater persistence. Our finding indicate integrin
mediated adhesion changes happened with the inhibition of Abl-family kinases, while RhoA
activity increased in this cases, which via myosin activation, led to an increase in the
magnitude of total traction force applied to the substrate. We also discovered a special band
of small punctate, rapidly turning over adhesions near the leading margin of spread D-shape
NBT-II cells. Our results taken as a whole indicate Abl family kinases play an important role
in the regulation of cell adhesion and migration in that their inhibition produces a profound
change in cell adhesions, morphology and migration. In this dissertation, we also elucidated

the mechanism of protein inactivation mediated by fluorescent protein chromophore-assisted light inactivation (FP-CALI). Our finding indicates the involvement of a reactive oxygen species (ROS) in the CALI effect. The progress towards a Bio-Field Effect Transistor (FET)-based detector of local cell adhesion in single cell was also included. Lastly, how the NBT-II cell may become a model for rapidly migrating cells and how the tools we developed may advance our current understanding of cell adhesion and migration is discussed.

DEDICATION

To my parents and grandma, who supported and encouraged me all the time.

And to my wife, Lily, who gives endless love and support to me.

I love you all!

ACKNOWLEDGMENTS

The work presented in this thesis would not have been possible without the supports from following people. I'd like to express my deepest gratitude and sincere appreciation to all of them.

First of all, I would like to thank my advisor Dr. Ken Jacobson for his patient guidance during my study and research in UNC. My previous background was Biomedical Engineering. Under his supervision, I made a successful transition from an engineering student to a real Cell Biologist. Dr. Ken Jacobson has been a role model for me, and has undeniably been the driving force to positively shape me into the scientist I am today. I am particularly grateful for his unwavering supports for the project and my career, and for making possible all of the incredible collaborations and opportunities I have had throughout my graduate career. It has been an honor and a privilege studying under him.

My warmest thanks also go to all my committee members: Dr. Keith Burridge, Dr. James Bear, Dr. Ted Salmon, and Dr. Maryna Kapustina. Thank you for your enthusiasm, guidance, and support. I feel so fortunate to have a committee composed of scientists that I have great admiration for.

I would like to show my gratitude to all of my other colleagues and collaborators, too numerous to name. Your support has been particularly meaningful to my graduate career. Thanks to all faculty and staff of the Department of Cell and Developmental Biology.

And finally, I want to express my gratitude for the daily and unconditional support I receive from my wife Lili Xu. We have been together as lovers and partners for almost 10 years. In the past, long distance, illness, and other difficulties never departed us but made us even stronger. We will be happily together forever.

TABLE OF CONTENTS

LIST OF FIGURES

LIST OF ABBREVIATIONS AND SYMBOLS

% – percent

° – degree

BSA – bovine serum albumin

C – Celsius

Ca^{2+} – calcium cation

CALI – chromophore-assisted light inactivation

cm – centimeter

C-terminus, C-term – carboxy terminus

DIC – differential interference contrast

DMEM – Dulbecco's modified eagle medium

DNA – deoxyribonucleic acid

DPBS – Dulbecco's phosphate-buffered saline

EGFP – enhanced green fluorescent protein

EM – electron-multiplying

EMCCD – electron-multiplying charge coupled device

Fab – fragment, antigen-binding

FBS – fetal bovine serum

FET – Field Effect Transistor

FRET – Förster resonance energy transfer

g – gram

g – gravitational acceleration
GST – Glutathione-S-transferase

h – hour

Hz – hertz

kHz – kilohertz

L – liter

LC – light chain

M – molar

mg – milligram

μ – micro

μg – microgram

μL – microliter

μm – micron

μM – micromole

μW – microwatt

min – minutes

mL – milliliters

mm – millimeter

mM – millimole

mFP – monomeric fluorescent protein

ms – millisecond

mW – milliWatt

n – number of trials

N.A. – numerical aperature

NBT-II – Nara Bladder Tumor No. 2

ng – nanogram

NIH – National Institutes of Health

nL – nanoliter

n_{lines} – number of lines

nm – nanometer

nM – nanomole

n_{px} – number of pixels

OD – optical density

PBS – phosphate-buffered saline

PFA – para-formaldehyde

pH – negative log (base 10) of the molar concentration of hydronium ions

PSF – point spread function

RPMI – Roswell Park Memorial Institute

s – seconds

SEM – standard errors of the means

SNR – signal-to-noise ratio

3D – three dimensional

3T3 – mouse embryonic fibroblast

TIR – total internal reflection

TIRF – total internal reflection fluorescence

v – volume

WT – wild type

CHAPTER 1

Introduction

This first chapter contains an overview of the doctoral work described in the six chapters of this dissertation. The work presented in this dissertation focuses on cell adhesion and cell migration research. The dissertation starts with a review of single cell migration, and then presents a detailed study of the migration of a particular rat bladder carcinoma cell that is regulated by Abl family kinases. Two techniques for the study of cell adhesion and cell migration have been developed by our group and my contribution to these efforts are described. Finally, a conclusion is presented.

The biological process of single cell migration in two-dimensional and three-dimensional environments is discussed in Chapter 2. Several representative examples of migrating cells are discussed: the migration of fibroblasts, the unusual movement of fish or amphibian keratocytes, and the amoeboid locomotion of leukocytes. Adhesions types, function, and their regulation are also reviewed. In addition, measurements of tractions in single migrating cells are reviewed. The work in Chapter 2 is reproduced/adapted with permission from an article in publication that was a part of the Comprehensive Physiology (Xavier Trepat, Zaozao Chen, and Ken Jacobson**. Cell Migration**. *Comprehensive Physiology*. 2012)

In Chapter 3, we report that Gleevec (Imatinib), an Abl family kinase inhibitor, produces a profound change in the shape and migration of rat bladder tumor cells (NBT-II) plated on collagen-coated substrates. Cells treated with Gleevec adopt a highly spread D-shape and migrate more rapidly with greater persistence. We found this more spread state is integrin mediated and is coupled with increases in the size and number of discrete adhesions. To be noted is a band of small punctate, rapidly turning over adhesions near the leading margin of the cell. Overall, inhibition of Abl-family kinases led to an increase in global cell-substrate adhesion. Gleevec-treated cells have greater RhoA activity which, via myosin activation, led to an increase in the magnitude of total traction force applied to the substrate. Our results taken as a whole indicate Abl family kinases play an important role in the regulation of cell adhesion and migration in that their inhibition produces a profound change in cell adhesions, morphology and migration. The work in Chapter 3 is under revision by PLoS ONE (Zaozao Chen et al. **PLoS ONE,** in revision. 2012)

The work presented in Chapter 4 elucidates the mechanism of protein inactivation mediated by fluorescent protein CALI (FP-CALI). Our finding indicates the involvement of a reactive oxygen species (ROS) in the CALI effect. The GST enzyme activity of purified Glutathione-S-transferase-FP (GST-EXFP) fusions was measured vitro before and after laser irradiation. We found different FP mutants fused to GST vary in their CALI efficiency in the order EGFP>EYFP>ECFP, while a GST construct that binds FlAsH results in significantly higher CALI efficiency than any of the XFPs tested. The work in this chapter is reproduced/adapted with permission from a paper published in the

Analytical Chemistry (Mark A. McLean, Zenon Rajfur, Zaozao Chen, David Humphrey, Bing Yang, Stephen G. Sligar, and Ken Jacobson. 2009. **Mechanism of chromophore assisted laser inactivation employing fluorescent proteins.** *Anal Chem.* 2009 Mar 1;81(5):1755-61. PMID: 19199572).

Progress towards a Field Effect Transistor (FET)-based detector of local cell adhesion in signal cells is presented in Chapter 5. This work was conducted in collaboration with Dr. Veena Misra's laboratory in the Department of Electrical & Computer Engineering at North Carolina State University. The devices were fabricated in the clean room of Nano-fabrication Center of NCSU. Cell experiments and device measurements were done either at UNC or NCSU. The final FET devices had a minimum dimension 2 microns. With these devices, we demonstrated the potential feasibility of this approach to resolve the adhesions of single cells to substrates but extensive further development work is required. Several abstracts were generated describing this work.

The last Chapter presents the conclusions from my work, providing an outlook of how the NBT-II cell may become a model for rapidly migrating cells and how the tools we developed may advance our current understanding of cell adhesion and migration.

CHAPTER 2

The review of single cell migration[1]

2.1 SUMMARY

Cell migration is fundamental to establishing and maintaining the proper organization of multi-cellular organisms. Morphogenesis can be viewed as a consequence, in part, of cell locomotion, from large-scale migrations of epithelial sheets during gastrulation, to the movement of individual cells during development of the nervous system. In an adult organism, cell migration is essential for proper immune response, wound repair, and tissue homeostasis, while aberrant cell migration is found in various pathologies. Indeed, as our knowledge of migration increases, we can look forward to, for example, abating the spread of highly malignant cancer cells, retarding the invasion of white cells in the inflammatory process, or enhancing the healing of wounds. This chapter is devoted to the single cell migrating in isolation such as occurs when leukocytes migrate during the immune response or when fibroblasts squeeze through connective tissue. Our research on NBT-II cell migration (in Chapter 3) is closely related to the topics reviewed here.

2.2 INTRODUCTIONS AND CONTEXT

In this section, some representative migrating cells will be introduced citing appropriate reviews, as there is by now a vast literature on cell migration. As examples, we will focus on fibroblast migration, the unusual movement of fish or amphibian keratocytes, and amoeboid locomotion as exemplified by leukocytes. Generally, in cell migration, cells must first adhere at some point. In this review, we will focus on various types of cell adhesions, highlighting some of the structural and signaling proteins involved. It is through adhesions that the tractions required for movement are applied to the substrate and we will outline the measurement of tractions in single, migrating cells. While, we focus on migration principles for cells moving on two-dimensional substrates, there is now a great deal of interest in single cell movement in three dimensional tissue environments (1, 2). However, detailed mechanisms are more difficult to dissect in these environments as the imaging tools available provide lower resolution at this juncture.

2.3 TYPES OF SINGLE CELL MIGRATION AND RELATED PHENOMENA

2.3.1. FIBROBLASTS

In vivo, fibroblasts are typically found in connective tissue where they synthesize collagens, glycosaminoglycans, and other important glycoproteins of the extracellular matrix (ECM) including fibronectin, for example. *In vitro*, these cells have been objects of extensive study because of the ease of culturing them (Figure 2.1A). Fibroblasts cultured on glass have a spread or spindle-shaped morphology, often characterized by

several extending processes (3, 4). In cell culture, fibroblasts move slowly with an average speed less than 1μm/min and often change direction. It is from fibroblast cell migration that the textbook paradigm for the classic steps of locomotion is derived. The locomotory cycle (e.g. Alberts et al, pp 965-1051. Molecular Biology of the Cell 5th Edition) consists of cells protruding and subsequently adhering at the leading margin, developing contractile forces between the front and trailing margins, and finally releasing trailing adhesions due to the applied tension and/or enzymatic action. Retraction generates excess dorsal surface to sustain the protrusion in a process termed retraction induced spreading (5, 6). Over the past several decades considerable work has been devoted to understanding the mechanistic steps of cell migration as exemplified by fibroblasts (7, 8).

Fibroblasts play a critical role in wound healing. *In vivo* (9), and *in vitro* (10), fibroblasts migrate into wounds, in the process cell acquiring cues that enable them to secrete ECM proteins and proliferate. However, they migrate *in vitro* with different speeds and morphology when compared to single fibroblasts in cell culture. Fibroblasts migrating into a wound tend to have a large lamellipod extending into the wound with few stress fibers in the cell; by contrast, stationary fibroblasts have smaller lamellipodia, and are characterized by multiple stress fibers. A typical wound healing assay is shown in figure 2.1B. It is known that many of the growth factors presented at a wound site act either as mitogens or as chemotactic factors for fibroblasts (11); these include, for example, epidermal growth factor (EGF) (12) and platelet derived growth factor (PDGF)

6

(13). Stimulation by growth factors can increase single fibroblast migration speed up to 3-fold, at the same time increasing changes in cell migration direction (12).
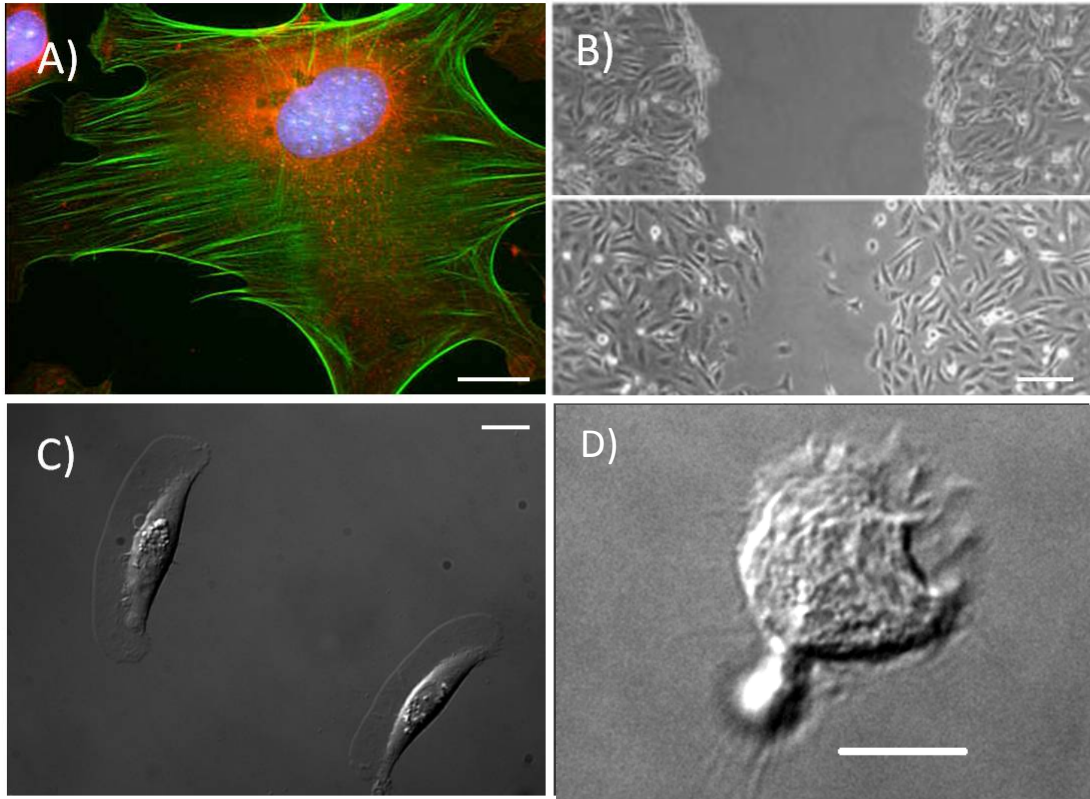
Figure 2.1. Different types of cell migration. (A) A stationary, spread C3H10T1/2 fibroblast triple stained with DAPI (Blue) for DNA, MitoTracker (Red) for mitochondria, and Alexa Fluor phalloidin (Green) for F-actin. (B) Fibroblasts migrating into wound. Top: initially, a wound was made in a confluent monolayer of MDA-MB-231cells by scratching using a pipette tip. Bottom: after 15 hours, migrating cells began to fill in the wound (14). (C) Migrating zebrafish keratocytes with large fan-like lamellipodia. (D) An HL-60 cell (Human promyelocytic leukemia cell) migrating on a glass substrate after differentiation with DMSO to exhibit leukocyte-like behavior on glass substrate. (Image in 1A and 1D are courtesy of Bing Yang and Zenon Rajfur, respectively.) Scale bars in A,C,D are 10μm, in B is 100um.

2.3.2 KERATOCYTES

At the other end of the spectrum of cell locomotion, fish or amphibian keratocytes migrate in rapid, highly persistent mode in which protrusion, contraction and retraction

are smoothly coordinated so that the cell maintains a nearly constant shape. Keratocytes are terminally differentiated epithelial cells in fish and amphibians that make good models for several aspects of migrating cells. In primary cultures of scales, keratocytes from goldfish (15, 16) were found to move away from the scale with high velocities (typically 10-15 μm/min but occasionally up to 60 μm/min). The highly directional movement of isolated keratocytes may originate from their ability to move as sheets to close wounds at the surface of the scale. Indeed they are robust migration machines, migrating for days under proper culture conditions. Even keratocytes lacking the nucleus and microtubules can migrate following a stimulus (17).

2.3.2.1 Lamellipodium structure:

Keratocytes have a large fan-like lamellipodium (figure 2.1C). The cell body at the base of lamellipodium is pulled (laterally) into to an elongated shape by actin bundles; in keratocytes microtubules and intermediate filaments do not penetrate the thin, actin-rich lamellipodium but are confined to the perinuclear region. Light, fluorescence and electron microscope images of f-actin in the lamellipodium can be reconciled and all show an oriented f-actin network (18); this presumably reflects the underlying branched actin network as described by the Dendritic Nucleation Model (7). The issue of the predominant f-actin structure is not completely settled, however, and an alternate view is offered by Urban et al (19).

2.3.2.2 Cytoskeletal dynamics and migration:

Considerable work has been devoted to the cytoskeletal mechanisms involved in keratocyte migration (20-22). Actin polymerization, treadmilling, retrograde actin network flow and myosin II-based contractility all play major roles in migrating keratocytes (21, 22). Indeed, the force required to stall a protruding keratocyte is consistent with an actin polymerization ratchet model (23); however, the shape of the force-velocity curve is not--indicating additional factors come into play when the elastic ratchet model (24, 25) is placed in a cellular context. Careful examination of actin flows using fluorescence speckle microscopy (FSM) reveals retrograde actin flow, smaller at the leading edge and larger at the wings (sides) of the keratocyte (26). The difference between protrusion and retrograde actin flow rates represents the net actin polymerization rate which is highest at center of the leading margin and falls off towards the wings. These flows are related to tractions exerted on the substratum (see below).

Interestingly, the myosin II network moves relative to the actin network (27). Since the myosin II inhibitor, blebistatin, reduces keratocyte locomotion, cell body translocation involves both actomyosin contraction as well as actin assembly. In fact, Theriot and coworkers (28) demonstrated a novel role for myosin II in addition to its well-known role powering contraction: by accelerating network disassembly, myosin II activity leads to network shrinkage via tension induced actin filament breakage. This action will not only directly lead to retraction but it also recycles monomeric actin for new polymerization at the front.

One effect of myosin II based contraction is to drive a forward flow of cytoplasm in migrating keratocytes (29). By measuring the front to rear gradient (higher in the front) in the concentration of quantum dots that had been introduced into the cytoplasm and fitting this data to a simple model for flow driven accumulation at the front, anterograde flow velocities in the cell frame of reference that were about 1/3 that of the keratocyte velocity (~0.1 μm/s vs ~0.3 μm/s) were obtained. Such flows could augment migration by feeding more actin monomer to the growing network at the leading edge and perhaps even providing pressure on the cell surface at the leading margin making network growth via actin polymerization more facile.

2.3.2.2 Shape and migration:

Recently, the shape and movement of keratocytes has been described in detail following an initial description by Lee et al (30) termed the Graded Radial Extension Model. Based on a shape and speed analysis of hundreds of cells, Theriot and coworkers proposed a model for observed keratocyte morphology and crawling behavior (29). Their model is based on the notion that actin polymerization and treadmilling drives migration but is it is resisted by the constant tension of an inextensible membrane surrounding cells of constant area. Spatial differences in the density of growing actin filament network, namely that the density of filaments is graded with highest values at the center of the leading edge, give rise to characteristic shape of the dominant modes of keratocyte locomotion. Thus, cells with higher actin density at the center than at the sides will have a larger aspect ratio defined as the ratio of the long axis (width) to short axis (length) of the keratocyte. In this model, global integration of spatially varying actin polymerization

powered protrusion is provided by membrane tension to specify cell shape. In addition, the model predicts that cell speed will be positively related to the aspect ratio of the cells; thus, canoe-shaped keratocytes, with a larger aspect ratio, move faster than D-shaped cells, with a smaller aspect ratio.

Mogilner and colleagues (31) have constructed *in silico* models of keratocyte locomotion in which several qualitative notions are incorporated mathematically. At the front of the cell, the dendritic nucleation model (7) is responsible for protrusion while at the rear, the dynamic network contraction model (21) is responsible for retraction. Recently, a model of a visco-elastic lamellipod was generated using a realistic geometry that correctly predicts measured centripetal flow of the actin network and the positive gradient of myosin II going from front to rear (32).

2.3.3 LEUKOCYTES

Leukocytes, or white blood cells (WBCs), are cells of the immune system defending the body against infecting organisms and foreign materials. They are highly motile cells found throughout the body, including tissues, blood and the lymphatic system. The recruitment of leukocytes to the site of bacterial and viral infection involves initial attachment to vascular endothelium, rolling, weak and firm adhesion, transendothelial migration and chemotaxis (33). Leukocyte chemotaxis in *vivo* and *vitro* occurs at speeds around 4 μm/min (34). Leukocytes migrate on different substrates through adhesions that involve the integrins β_2, and $\alpha_4\beta_1$ (35). However, recently it has been reported that leukocytes can adhere and migrate in an integrin independent manner

(34), indicating that leukocytes employ additional mechanisms for adhesion and migration. A view of differentiated migrating HL-60 leukemia-like cell is shown in figure 2.1D.

2.3.4. SINGLE CELL MIGRATION IN THREE DIMENSIONS

Although cell migration has been studied extensively in essentially two-dimensional (2D) cell culture conditions where cells grow on a substrate, increasing attention has been paid to the movement of cells in 3D environments. The 3D matrix acts as a scaffold that produces physical support for cells which can affect cell morphology and induce cell growth or migration (36, 37). In addition, the matrix can induce variation in signaling cascades in cells via adhesions and tensile forces (see for example, (38)).

2.3.4.1. Cell morphology and migration in 3D environments:

Most migration modes previously observed in 2D environments also occur in 3D tissue environments. However, because the distribution of ligands in 2D is generally much more uniform than in 3D matrix models where, for example, clustered ligands may exist on fibrils, cell morphology is quite different in the two environments (36). In 2D cell culture, fibroblasts have large lamellipodia and filopodia. By contrast, fibroblasts in 3D collagen gels exhibit both smaller and fewer lamellipodia and filopodia (39). Due to extensive adhesion to a flat substratum, cells in 2D show very broad, flat and thin lamellipodia whereas cells in 3D show a less exaggerated appearance. Three motile morphologies can be delineated in a 3D matrix (37): amoeboid blebby (macrophages,

some stem cells on soft/loose connective tissue); amoeboid pseudopodal (leukocytes, dictyostelium on loose connective tissue); and, mesenchymal (fibroblasts, and some cancer cells on loose or dense connective tissue).

2.3.4.2. Regulation of cell migration in 3D matrices:

Three important factors regulate 3D cell migration: cell-matrix adhesions, the Rho family of small GTPases, and proteases. In 2D culture, integrins are primarily responsible for cell adhesions to ECM in the form of focal adhesions, focal contacts, podosomes, etc. However, in 3D cell culture, a reduction in the number of focal adhesions and their component integrins occurs. Thus, for example, αVβ3 integrin, which is highly expressed in 2D cell culture, was not detected in the 3D-matrix adhesions of fibroblasts, and the level of FAK phosphorylation was reduced (40). Changes in the nature and strength of adhesions in 3D and 2D environments will result in differences in cell tension, morphology, and migration type (41).

The Rho family of small GTPases play a prominent role in regulating cell migration in 3D. Leukocytes employ amoeboid migration that is based on the Rho/ROCK pathway maintaining contractility at the posterior end and Rac1 mediating protrusion at the leading margin (42). However, other reports indicate that Rac1 activity is suppressed in fibroblasts and neurons in 3D culture, thus decreasing leading edge ruffling and axonal branching, respectively (43, 44).

The role of proteolysis in 3D migration in tissue has been actively investigated. Multiple proteases have collagenolytic activity but the emphasis has been on matrix-

13

metallo proteases (MMP) and these have been reported to affect both normal and cancer cell migration *in vitro* (see also collective cell migration below). However, clinical trials of MMP inhibitors did not impair metastasis suggesting that metastatic cells may switch from mesenchymal to ameboid locomotion (45-47).

2.4 ADHESIONS IN MIGRATING CELLS

Cells adhere to ECM or other cells by both non-specific electrostatic interactions and specific binding of cell adhesion molecules such as selectins, integrins, and cadherins to extracellular matrix ligands and to cadherins on other cells. We will focus on cell-ECM adhesions, and divide such adhesions into focal adhesions, podosomes, focal complexes, and close contacts.

2.4.1. Focal adhesions: composition and structure

Focal adhesions were first identified in chicken heart fibroblasts by electron microscopy, as dense plaques between the cell's ventral surface and the substrate (4). Focal adhesions are usually found at the ends of stress fibers; they have a dimension on the order of a micron, and a lifetime ranging between minutes and hours. They have been visualized by epifluorescence microscopy (Figure 2.2A), by total internal fluorescence microscopy (TIRFM), or by interference reflection contrast microscopy (IRM) (Figure 2.2B). In the past, terms such as adhesion plaques (4), or focal contacts (48) were employed, but now the field appears to have settled on the term focal adhesion (FA) (49). Focal adhesion components can be divided into four general categories: (1) ECM components, of which fibronectin, laminin, vitronectin, and the collagens are important

examples; (2) transmembrane proteins, of which integrins are the most prominent class; (3) structural proteins that both stabilize the FA and provide scaffolding functions; and (4) signaling proteins (50, 51). The number of proteins found in focal adhesions is now exceeds160, and the possible interactions between these components is described in what is colloquially called the "Geiger diagram" (49) which evolves as new components are identified (51, 52).

Integrins are the transmembrane proteins that recognize ECM proteins containing short amino acid sequences, such as the Arginine-Glycine-Aspartic acid (RGD), Asp-Gly-Glu-Ala (DGEA) and Glycine-Phenylalanine-Hydroxyproline-Glycine-Glutamate-Arginine (GFOGER) motifs (53, 54). Functional integrins are heterodimers containing two distinct (α and β) subunits. Currently, there are more than 24 types of α and β integrin subunits characterized in mammals (55, 56). Each type of integrin heterodimer binds distinct ligands, e.g. α5β1 integrin binds fibronectin, and α3β1 bind to laminin (57). Focal adhesions in different fibroblasts and epithelial cells that are adherent to distinct ECM materials contain integrins with various combinations of α and β subunits (58).

One function of cytoskeletal proteins, including talin (59), α-actinin (60), filamin (61) and tensin (62), is to link integrins to the actin cytoskeleton. Other adaptor proteins directly or indirectly interact with integrin cytoplasmic tails and form protein complexes; examples include FAK (63, 64)], vinculin (65), paxillin (66, 67), dynamin (68), and Ena/VASP (69). As an example, an epi-fluorescence image of antibody labeled paxillin is given in Figure 2.2A and shows the extensive array of FAs in murine fibroblasts adherent to a serum coated glass substrate.

Signaling proteins are recruited to FA and regulate their assembly and disassembly; examples include the Src family of non-receptor tyrosine kinases (NRPTK) (70), the Abl family NRPTK (71) and the Rho family of small GTPases (72), and p21-activated kinase (73) (74). In addition, phosphorylation of paxillin by c-Jun amino-terminal kinase (JNK) or cdk 5 has been found essential for maintaining the labile adhesions required for rapid migration in both fibroblasts and neurons (14, 75). Some proteins and signaling pathways involved in FA structure and regulation and their relationship to cell adhesion and migration are diagrammed schematically in Figure 2.2C. FA appear to be an amorphous collection of interacting proteins making 3D structure determinations difficult be either light or electron microscopy. However, recently progress has been made employing photoactivation localization microscopy (PALM) in 2D (76, 77) and by iPALM, in 3D (78). Such studies are revealing the 3D organization of individual FA proteins (79).
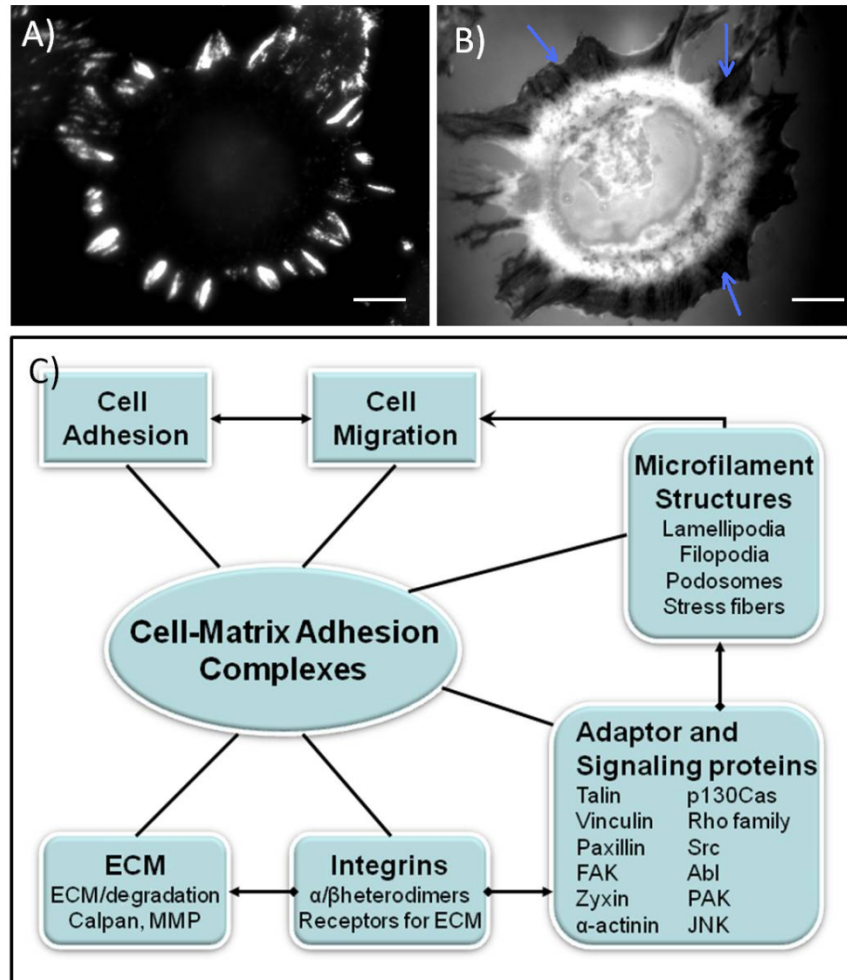
Figure 2.2. Adhesion structure and function in cells

(A) An immunofluorescence image of focal adhesions in an NIH 3T3 cell stained with anti-paxillin; (B) an interference reflection microscopy (IRM) image of focal focal adhesions in a similar NIH 3T3 fibroblast on a FN coated substrate; the very dark regions (arrows) are focal adhesions; (C) Schematic figure for the relationship between cell adhesion, cell migration, and some of the corresponding adaptor and signal proteins. Cell matrix adhesion complexes are depicted a key component in single cell adhesion and migration. After activation, integrins bind ECM and provide a link to the actin cytoskeleton. Cytoplasmic adaptor proteins bind integrin cytoplasmic domains, stabilize FA, and provide scaffolding functions. Integrin activation also initiates downstream signaling. Such signaling may regulate cell adhesion turnover, internal force development, and cytoskeletal rearrangements including formation of stress fibers, lamellipodia, filopodia and podosomes. Cell migration also involves both ECM degradation and proteolysis and adhesion complex internalization (see section on focal adhesion dynamics). Scale bars in A & B are 10μm.

2.4.2. Focal adhesion dynamics

FAs are dynamic structures that undergo cycles of assembly and disassembly; indeed, regulated FA turnover is integral to cell migration. Thus, here we will review some the key aspects of FA dynamics.

Focal adhesion assembly: The role of integrin activation in FA assembly and in initiating downstream signaling has been extensively investigated. With stimulation, for example, by growth factors, integrin β subunit cytoplasmic domains bind the talin phosphotyrosine-binding (PTB) domain causing integrin activation (80, 81). Activated integrins then bind ECM components and the cytoplasmic domain recruits signaling proteins; this process initiates downstream signaling, including FAK phosphorylation, MAP kinase activation, paxillin binding, and the formation of a complex containing vinculin, FAK, α-actinin, WASP, tensin, Src and zyxin (51, 82, 83). Knockouts of key recruited signaling components have demonstrable effects on cell adhesion and migration. Thus, for example, FAK null fibroblasts exhibit increased numbers of adhesions and consequent reduced cell motility (84). In addition, kinase dead Src mutants promoted both the number and size of cell adhesions, reducing the speed of cell migration. Webb et al found that Src, paxillin and FAK formed complexes in *vitro* and *vivo*; in this study, FAK and Src were speculated to regulate cell adhesion disassembly via paxillin and the downstream ERK and MLCK pathways (85). Abl knockdown cells also exhibited an increase in cell adhesion size and stability, and rescue of Abl kinase activity restored the cell adhesion disassembly rate (86). Rho family GTPases have also

been reported as key regulators of focal adhesion dynamics, e.g. active RhoA changed small peripheral adhesions (focal complexes) into elongated focal adhesions (87). External stretch induced nascent adhesions to mature into focal adhesions via a RhoA-ROCK pathway (87).

Focal adhesion disassembly: Compared with extensive studies on FA formation, the disassembly process is not as clear. Several related pathways may contribute to focal adhesion disassembly: i) adhesion release produced by ECM degradation; ii) adhesion turnover mediated by the cytoskeleton and internalization; and iii) disassembly mediated by kinases and proteases (88, 89). It has been reported that ECM degradation is, in part, responsible for cell adhesion disassembly, cell migration, and invasion (90); thus, for example, ECM degradation by matrix metalloproteinases (MMPs) could induce the release of cell adhesions resulting in an increase cell motility and invasion (91, 92). Cytoskeletal components are an important regulatory factor in adhesion disassembly. Microtubules (MTs) have been observed to target focal adhesions promoting their disassembly (93, 94). Moreover, MTs have been speculated to induce cell adhesion disassembly via dynamin and clathrin dependent integrin endocytosis (95, 96). Caveolin-1 was also reported to regulate FA turnover and cell migration directionality possibly via internalization (97, 98). In addition, cellular contractile machinery may also induce focal adhesion disassembly; for example, RhoA, and myosin II were found to positively regulate adhesion disassembly and cause cell rear detachment (99, 100).

Proteases and kinases have also been reported to regulate cell adhesion. Calpain, a calcium-dependent protease cleaves talin, FAK, and paxillin in FA(91). Cleavage of these proteins leads to disassembly of the FA and the detachment of the tail of the cell (101, 102). Moreover, recent studies have demonstrated that, Smurf1, an E3 ubiquitin ligase, degrades the talin head and controls cell adhesion stability (103). Other ubiquitin ligases, including Cbl, Smurf2, HDM2, BCA2, also play an important role in regulating cell adhesion and migration through ubiquitination of their specific substrates (89).

Methods have been developed to study the dynamics of focal adhesions. Studies using FRAP and GFP-fusion proteins or labeled microinjected proteins have shown that protein components of focal adhesions including α-actinin, vinculin and FAK slowly exchange between the cytosol and the adhesion with half-times for recovery on the order of minutes. More recently, Horwitz and co-workers measured adhesion disassembly rates of fluorescent protein (FP) conjugated -paxillin, -FAK and -zyxin; these studies indicated that the FAK-Src complex could interrupt focal adhesion maturation by promoting disassembly through the downstream ERK and MLCK pathways (85). Using the techniques of image correlation microscopy, Gratton, Wiseman, Horwitz and their co-workers measured FAK, Vinculin (Vn) and Paxillin (Pax) diffusion and binding to adhesions in mouse embryonic fibroblasts. No FAK, Vn and Pax complexes were preassembled in cytoplasm, but when the adhesions disassembled, these proteins disassociated in complexes (104, 105). Waterman and colleagues studied FA dynamics using speckle microscopy and advanced image analysis; they found that the retrograde F-actin network velocity is a fundamental regulator of traction force at FAs via the Rho and

20

myosin II pathways (106). These investigators also demonstrated that the interplay between actomyosin and FA dynamics results in a balance between adhesion and contraction in order to induce maximal migration velocity. Such studies indicated a relationship between force and FA assembly and disassembly and predicted how under certain circumstances the FA slide (83, 107).

2.4.3. Podosomes

Podosomes are specialized integrin-mediated adhesions often found in highly migratory monocytic cells that mediate the inflammatory response (92, 108). They also have the capacity for matrix degradation. Linking the ECM to the actin cytoskeleton, podosomes have a fairly uniform dimension of around 0.5um, a half-life of 2 to 20 min and are abundant (20-100 per cell) (92, 109). An image of podosomes is shown in figure 2.3B.

Podosomes have a dense actin core surrounded by a rosette-like structure containing integrins, such as $\alpha_v\beta_3$, FA proteins including talin and vinculin that play a major structural role, other actin-associated proteins (gelsolin, alpha-actinin and actin-related protein 2/3 (Arp2/3)), tyrosine kinases (Src, Pyk2) and phosphoinositide-3 kinase (PI3K)) and also the Rho-family GTPases (108). The podosome core also contains proteins involved in regulating actin polymerization including WASP (Wiskott-Aldrich Syndrome Protein) (92, 108). A larger, more stable but related structure, the invadopodia, plays an important role in invasive cancer cells and has been thoroughly reviewed (110-112).

2.4.4. Focal complexes

The term, "focal complex", describes small adhesions that form at the leading margin of migrating cells, typically fibroblasts. Focal complexes are significantly smaller in area (<0.25μm²), and are shorter lived (often <5min but some have even shorter lifetimes) than focal adhesions (113). Focal complexes contain integrins, talin and paxillin, but fewer actin filaments are associated with them (49, 101). Migrating cells often have a large number of focal complexes at the protruding edge. Most of these focal complexes never mature, and are likely disassembled when the lamellipodium retracts. Some investigators have suggested that focal complexes might be precursors of FA because applied contractile forces can convert focal complexes into larger oval shape adhesions (114-117).

2.4.5. Close contacts in migrating cells

Close contacts appear as broad grey areas in interference reflection microscopy (IRM) (Figure 2.3A). The original definition of close contacts was based on IRM images and indicated that the separation between the ventral surface of the cell and the substratum was about 20 to 50 nm (48). By contrast, the ventral surface and substratum is separated by 10–15 nm or less in FA. Compared to FA, little is known about these adhesions. They predominate in fast moving cells such as keratocytes (118, 119) although regions of close contact also exist in fibroblasts and epithelial cells in culture. (120).

The composition of close contacts was investigated by immunofluorescence staining of fish keratocytes using antibodies against known FA components. The close

contact areas at the rim of leading edge were found enriched in β1-integrin and talin, with little paxillin and FAK (118). In general, close contacts appear to be mediated by integrins. Forward movement of the Xenopus keratocyte lamella could be halted by adding RGD peptide or an anti-integrin mAb while the rear of cell continued to retract (121).

Anderson and Cross (119) performed a detailed study of more mature vinculin-containing adhesions using microinjected fluorescent vinculin and combined confocal and IRM imaging. They found that these contacts formed behind the leading edge and matured beneath the lamellipodium and remained stationary while the cell passed over them. By contrast, vinculin-containing contacts in the wings of the cell grew larger before sliding inward. These large contacts are presumably transmitting the large lateral traction in keratocytes that are used for retraction of the wings. The actual mechanism for disassembly of released contacts remains an open question.

There are really no structural models for close contacts. A possible model would consist of finger-like projections of a small diameter that contact the surface using the usual repertoire of focal adhesions molecules (Figure 2.3C). In this respect, these projections would be a cross between podosomes and filopodia. The net result would be to draw the surface closer to the substratum such that the region appears grey in IRM yet the adhesion itself could be readily remodeled to accommodate rapid cell migration.
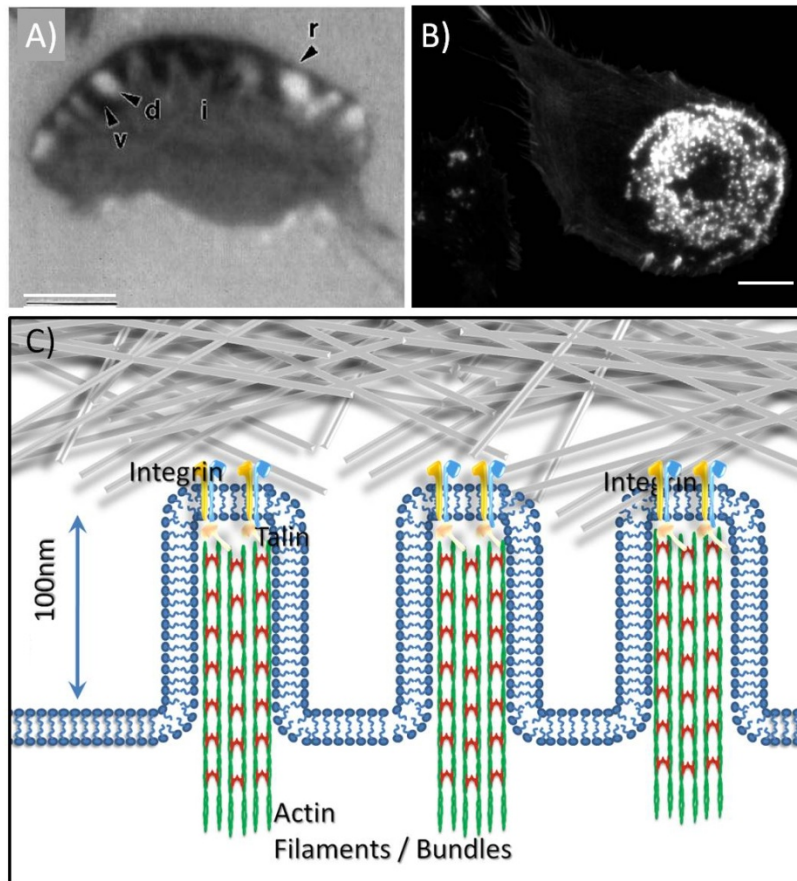
Figure 2.3. Different type of cell adhesions

(A) IRM image of close adhesion in migrating fish keratocytes, the adhesion pattern consists of an outer rim (r) of very close contact skirting a crescent-shaped band of alternating very close (v) and distant contacts (d). B) Epi-fluorescent image of podosomes in a human dendritic cell with F-actin labeling. C) A hypothetical view of close contacts in which small diameter projections attach to the substrate and serve to draw the ventral surface closer to the substrate such that it appears grey in IRM. Integrin, talin, F-actin have been reported to be in close adhesions (in this schematic, the actin network is depicted like that in a microvillus with parallel actin bundles but it could also be in the form of a dendritic actin network (not shown)); however, paxillin and FAK are not found in initial close contacts. Scale bars are 10μm. Image in panel A is from Lee and Jacobson 1997; image in panel B is courtesy of Aaron Neumann.

2.4.6. Outlook

In addition to the extensive cataloging of adhesion components, there are recent developments in super-resolution microscopy (79) and several live cell fluorescence microscopy methods that promise to enhance our understanding of structure-function relationships in the adhesive structures that enable the cell to exert traction on its environment (106, 122, 123). Also, recent developments in Rho family biosensors and detailed analysis of such data, promise to provide detailed mapping of the localization and activation pattern of these GTPases in relation to the regulation of dynamic adhesive behavior, tractions and cell migration (124-126). Overall, it appears that the next decade will produce important advances in our understanding of cell-substratum adhesions.

2.5 MEASUREMENTS OF TRACTIONS IN SINGLE MIGRATING CELLS

2.5.1. Elastic substrate traction measurements

The effects of tractions exerted by migrating chick heart fibroblasts plated on a deformable silicone substrate (a thin film of silicone cross-linked by means of glow-discharge) were visualized as visible wrinkles in the film under the cell body and perpendicular to the direction of cell movement (73). Such compression wrinkles qualitatively reflect the strong contractile forces exerted by fibroblasts on their environment but do not give the actual distribution of traction stresses under the cell.

Spatially resolved information on the distribution of tractions has been obtained in the past 15 years by following the displacements of fiduciary markers embedded in

deformable substrata (Figure 2.4) or the response of individual force sensing elements. This approach was first applied to fish scale keratocytes migrating on silicone rubber substrata in which small polystyrene latex beads had been embedded (120). When the tractions were calculated from the bead displacements (127), it was found, surprisingly, that the major propulsive tractions were applied in the wings of the keratocyte (128).
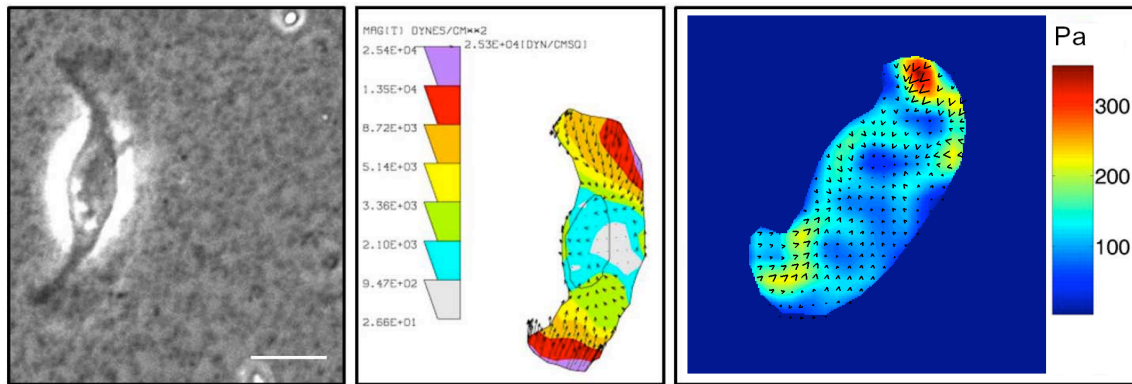
Figure 2.4. Use of elastic substrates to map tractions in migrating cells
A. Phase image showing a fish keratocytes crawling on an elastic polyacrylamide substrate. B. Tractions mapped on the same cell shown in A. The Dembo Boundary element method algorithm (127) was used to calculation of cell traction force from beads displacement; the units in the map are in Dynes/ cm^2 (1 dyne=10^{-5}N). 4C. The Fourier-transform traction cytometry (FTTC) algorithm (129) was used to calculate tractions for another keratocyte; the right scale of color bar represents stress in units of Pa (1Pa=1N/m^2). Scale bar is 10μm. Images are courtesy of Zenon Rajfur.

However, with silicone rubber films, matching the compliance to the tractions exerted by the cells and providing a defined surface coating on the film for optimal adhesion is not always easy. These difficulties were circumvented by developing polyacrylamide gel substrates with variable degrees of cross-linking onto which extracellular matrix proteins could be conjugated (130-135). An example of the use of

polyacrylamide substrates for examining the tractions exerted by locomoting keratocytes in seen in Figure 2.4. Moreover, these films are optically tractable so that when fluorescent beads are used as the fiduciary markers in the gel, dual channel fluorescence microscopy permits the correlation of tractions in relation to the spatial localization of fluorescently-labeled focal adhesion proteins (115).

Another approach employs special microfabricated substrates that contain an array of force sensing elements. These are flexible cantilevers of known bending stiffness so that the forces exerted by moving cells on these pads can be computed directly from the deflection of the cantilever beams (136-138). An alternate approach employs an elastomeric substrate (silicone film) that is micropatterned to give rise to a regular array of either surface indentations or projections of sub-micron dimensions (117, 139). An algorithm allows the surface distortion of the micropattern caused by cells to be directly translated to the cellular forces. Thus, a number of methods now exist that are similar in overall concept and permit calculation of traction stresses and the correlation of those stresses with the molecular constituents of the force-transmitting adhesive structures.

2.5.2. Force, cell adhesions, and cell migration

There is a clear interplay between contractile force generated by the cell, adhesion to the substrate and the traction applied to the substrate that is beginning to be investigated in detail. As stated above, force can induce focal complexes to mature into large focal adhesions near the leading edge of migrating cells; at the trailing edge, contractile forces regulate adhesion disassembly and cell detachment. Also, MT induced

27

adhesion disassembly has been observed as mentioned previously and it was speculated that the growth of stiff microtubule growth into adhesions can release the force originally exerted by the actomyosin cytoskeleton, thus promoting adhesion disassembly (87, 94).

The relationship between adhesion, traction applied to the substrate, and cell migration is under active investigation. At the outset, it is important to note that the net traction to move the cell through a low viscosity buffer is effectively zero. This leads to the conclusion that the typical tractions measured, which are much larger than what are required to move the cell, must be used to break adhesions in spatiotemporal patterns that dictate both the speed and direction of the cell.

Using keratocytes as a model, Lee and her colleagues reported that slowly migrating keratocytes are more fibroblast-like in their migration and characterized by slipping of adhesions that are coupled with retrograde actin flow; in fast moving keratocytes, adhesions have more gripping character to sustain the rapid protrusion powered by the fast-paced polymerizing actin network; these cells exhibit a much smaller rearward actin flow (140). Recently, maps of actin–substrate coupling were used to quantify differences in force transmission efficiency between different cell regions (20). Thus, a more detailed scenario about the substrate adhesion-traction-migration relationship could be proposed: At the leading edge, traction was transmitted in a manner partially independent of actin velocity (gripping) but at the cell flanks, the force transmission was mediated by the high friction between the actin network and the substrate; at the cell body, little traction was transmitted, because of low friction.

Undoubtedly, this relationship will be further investigated both experimentally and theoretically (32) as it is key to achieving a global understanding of how cells move.

2.6 CREDITS

2.7 REFERENCES

1.   Gligorijevic B and Condeelis J. (2009). Stretching the timescale of intravital imaging in tumors. *Cell Adh Migr* 3(4): p. 313-5

2.   Friedl P and Wolf K. (2010). Plasticity of cell migration: a multiscale tuning model. *J Cell Biol* 188(1): p. 11-9

3.   Puck TT, Cieciura SJ, and Fisher HW. (1957). Clonal growth in vitro of human cells with fibroblastic morphology; comparison of growth and genetic characteristics of single epithelioid and fibroblast-like cells from a variety of human organs. *J Exp Med* 106(1): p. 145-58

4.   Abercrombie M, Heaysman JE, and Pegrum SM. (1970). The locomotion of fibroblasts in culture. 3. Movements of particles on the dorsal surface of the leading lamella. *Exp Cell Res* 62(2): p. 389-98

5.   Chen W-T. (1979). Induction of spreading during fibroblast movement. *J. Cell Biol.* 81: p. 684-691

6.   Dunn GA. (1980). Mechanisms of fibroblast locomotion. *Cell Adhes. Mot.*: p. 409-424

7.   Pollard TD and Borisy GG. (2003). Cellular motility driven by assembly and disassembly of actin filaments. *Cell* 112(4): p. 453-65

8.   Ridley AJ, Schwartz MA, Burridge K, Firtel RA, Ginsberg MH, Borisy G, Parsons JT, and Horwitz AR. (2003). Cell migration: integrating signals from front to back. *Science* 302(5651): p. 1704-1709

9.   Martin P. (1997). Wound healing--aiming for perfect skin regeneration. *Science* 276(5309): p. 75-81

10.   Schreier T, Degen E, and Baschong W. (1993). Fibroblast migration and proliferation during in vitro wound healing. A quantitative comparison between various growth factors and a low molecular weight blood dialysate used in the clinic to normalize impaired wound healing. *Res Exp Med (Berl)* 193(4): p. 195-205

11.   Werner S and Grose R. (2003). Regulation of wound healing by growth factors and cytokines. *Physiol Rev* 83(3): p. 835-70

12.   Ware MF, Wells A, and Lauffenburger DA. (1998). Epidermal growth factor alters fibroblast migration speed and directional persistence reciprocally and in a matrix-dependent manner. *J Cell Sci* 111 (Pt 16): p. 2423-32

13.   Suetsugu S, Yamazaki D, Kurisu S, and Takenawa T. (2003). Differential roles of WAVE1 and WAVE2 in dorsal and peripheral ruffle formation for fibroblast cell migration. *Dev Cell* 5(4): p. 595-609

14.   Huang C, Rajfur Z, Borchers C, Schaller MD, and Jacobson K. (2003). JNK phosphorylates paxillin and regulates cell migration. *Nature* 424(6945): p. 219-23

15.   Goodrich HB. (1924). Cell behaviour in tissue cultures. . *Biol. Bull (Woods Hole).* (46): p. 252-262.

16.   Radice GP. (1980). Locomotion and cell-substratum contacts of Xenopus epidermal cells in vitro and in situ. *J Cell Sci* 44: p. 201-23

17.   Verkhovsky AB, Svitkina TM, and Borisy GG. (1999). Self-polarization and directional motility of cytoplasm. *Curr Biol* 9(1): p. 11-20

18.   Verkhovsky AB, Chaga OY, Schaub S, Svitkina TM, Meister JJ, and Borisy GG. (2003). Orientational order of the lamellipodial actin network as demonstrated in living motile cells. *Mol Biol Cell* 14(11): p. 4667-75

19.   Urban E, Jacob S, Nemethova M, Resch GP, and Small JV. (2010). Electron tomography reveals unbranched networks of actin filaments in lamellipodia. *Nat Cell Biol* 12(5): p. 429-35

20.   Fournier MF, Sauser R, Ambrosi D, Meister JJ, and Verkhovsky AB. (2010). Force transmission in migrating cells. *J Cell Biol* 188(2): p. 287-97

21.   Svitkina TM, Verkhovsky AB, McQuade KM, and Borisy GG. (1997). Analysis of the actin-myosin II system in fish epidermal keratocytes: mechanism of cell body translocation. *J Cell Biol* 139(2): p. 397-415.

22.   Small JV, Herzog M, and Anderson K. (1995). Actin filament organization in the fish keratocyte lamellipodium. *J Cell Biol* 129(5): p. 1275-86

23.   Prass M, Jacobson K, Mogilner A, and Radmacher M. (2006). Direct measurement of the lamellipodial protrusive force in a migrating cell. *J Cell Biol* 174(6): p. 767-72

24.   Mogilner A and Oster G. (1996). Cell motility driven by actin polymerization. *Biophys J* 71(6): p. 3030-45

25.   Mogilner A and Oster G. (2003). Force generation by actin polymerization II: the elastic ratchet and tethered filaments. *Biophys J* 84(3): p. 1591-605

26.   Vallotton P, Danuser G, Bohnet S, Meister JJ, and Verkhovsky AB. (2005). Tracking retrograde flow in keratocytes: news from the front. *Mol Biol Cell* 16(3): p. 1223-31

27.   Schaub S, Bohnet S, Laurent VM, Meister JJ, and Verkhovsky AB. (2007). Comparative maps of motion and assembly of filamentous actin and myosin II in migrating cells. *Mol Biol Cell* 18(10): p. 3723-32

28.   Wilson CA, Tsuchida MA, Allen GM, Barnhart EL, Applegate KT, Yam PT, Ji L, Keren K, Danuser G, and Theriot JA. (2010). Myosin II contributes to cell-scale

actin network treadmilling through network disassembly. *Nature* 465(7296): p. 373-7

29. Keren K, Yam PT, Kinkhabwala A, Mogilner A, and Theriot JA. (2009). Intracellular fluid flow in rapidly moving cells. *Nat Cell Biol* 11(10): p. 1219-24

30. Lee J, Ishihara A, Theriot JA, and Jacobson K. (1993). Principles of locomotion for simple-shaped cells. *Nature* 362(6416): p. 167-71

31. Rubinstein B, Jacobson K, and Mogilner A. (2005). Multiscale Two-Dimensional Modeling of a Motile Simple-Shaped Cell. *Multiscale Model Simul* 3(2): p. 413-439

32. Rubinstein B, Fournier MF, Jacobson K, Verkhovsky AB, and Mogilner A. (2009). Actin-myosin viscoelastic flow in the keratocyte lamellipod. *Biophys J* 97(7): p. 1853-63

33. Hynes RO and Lander AD. (1992). Contact and adhesive specificities in the associations, migrations, and targeting of cells and axons. *Cell* 68(2): p. 303-22

34. Lammermann T, Bader BL, Monkley SJ, Worbs T, Wedlich-Soldner R, Hirsch K, Keller M, Forster R, Critchley DR, Fassler R, and Sixt M. (2008). Rapid leukocyte migration by integrin-independent flowing and squeezing. *Nature* 453(7191): p. 51-5

35. Laudanna C, Campbell JJ, and Butcher EC. (1996). Role of Rho in chemoattractant-activated leukocyte adhesion through integrins. *Science* 271(5251): p. 981-3

36. Even-Ram S and Yamada KM. (2005). Cell migration in 3D matrix. *Curr Opin Cell Biol* 17(5): p. 524-32

37. Friedl P and Gilmour D. (2009). Collective cell migration in morphogenesis, regeneration and cancer. *Nat Rev Mol Cell Biol* 10(7): p. 445-57

38. Amatangelo MD, Bassi DE, Klein-Szanto AJ, and Cukierman E. (2005). Stroma-derived three-dimensional matrices are necessary and sufficient to promote desmoplastic differentiation of normal fibroblasts. *Am J Pathol* 167(2): p. 475-88

39. Heath JP and Peachey LD. (1989). Morphology of fibroblasts in collagen gels: a study using 400 keV electron microscopy and computer graphics. *Cell Motil Cytoskeleton* 14(3): p. 382-92

40. Cukierman E, Pankov R, Stevens DR, and Yamada KM. (2001). Taking cell-matrix adhesions to the third dimension. *Science* 294(5547): p. 1708-12

41. Kole TP, Tseng Y, Jiang I, Katz JL, and Wirtz D. (2005). Intracellular mechanics of migrating fibroblasts. *Mol Biol Cell* 16(1): p. 328-38

42. Sanz-Moreno V and Marshall CJ. (2009). Rho-GTPase signaling drives melanoma cell plasticity. *Cell Cycle* 8(10): p. 1484-7

43. Hu H, Marton TF, and Goodman CS. (2001). Plexin B mediates axon guidance in Drosophila by simultaneously inhibiting active Rac and enhancing RhoA signaling. *Neuron* 32(1): p. 39-51

44. Pankov R, Endo Y, Even-Ram S, Araki M, Clark K, Cukierman E, Matsumoto K, and Yamada KM. (2005). A Rac switch regulates random versus directionally persistent cell migration. *J Cell Biol* 170(5): p. 793-802

45. Wolf K, Mazo I, Leung H, Engelke K, von Andrian UH, Deryugina EI, Strongin AY, Brocker EB, and Friedl P. (2003). Compensation mechanism in tumor cell migration: mesenchymal-amoeboid transition after blocking of pericellular proteolysis. *J Cell Biol* 160(2): p. 267-77

46. Wolf K, Wu YI, Liu Y, Geiger J, Tam E, Overall C, Stack MS, and Friedl P. (2007). Multi-step pericellular proteolysis controls the transition from individual to collective cancer cell invasion. *Nat Cell Biol* 9(8): p. 893-904

47. Niggemann B, Drell TLt, Joseph J, Weidt C, Lang K, Zaenker KS, and Entschladen F. (2004). Tumor cell locomotion: differential dynamics of spontaneous and induced migration in a 3D collagen matrix. *Exp Cell Res* 298(1): p. 178-87

48. Izzard CS and Lochner LR. (1976). Cell-to-substrate contacts in living fibroblasts: an interference reflexion study with an evaluation of the technique. *J Cell Sci* 21(1): p. 129-59

49. Zamir E and Geiger B. (2001). Molecular complexity and dynamics of cell-matrix adhesions. *J Cell Sci* 114(Pt 20): p. 3583-90

50. Lo SH and Chen LB. (1994). Focal adhesion as a signal transduction organelle. *Cancer Metastasis Rev* 13(1): p. 9-24

51. Zaidel-Bar R, Cohen M, Addadi L, and Geiger B. (2004). Hierarchical assembly of cell-matrix adhesion complexes. *Biochem Soc Trans* 32(Pt3): p. 416-20

52. Geiger B, Spatz JP, and Bershadsky AD. (2009). Environmental sensing through focal adhesions. *Nat Rev Mol Cell Biol* 10(1): p. 21-33

53. Reyes CD and Garcia AJ. (2003). Engineering integrin-specific surfaces with a triple-helical collagen-mimetic peptide. *J Biomed Mater Res A* 65(4): p. 511-23

54. Emsley J, Knight CG, Farndale RW, Barnes MJ, and Liddington RC. (2000). Structural basis of collagen recognition by integrin alpha2beta1. *Cell* 101(1): p. 47-56

55. Humphries MJ. (2000). Integrin structure. *Biochem Soc Trans* 28(4): p. 311-39

56. Barczyk M, Carracedo S, and Gullberg D. (2010). Integrins. *Cell Tissue Res* 339(1): p. 269-80

57.   Tavella S, Bellese G, Castagnola P, Martin I, Piccini D, Doliana R, Colombatti A, Cancedda R, and Tacchetti C. (1997). Regulated expression of fibronectin, laminin and related integrin receptors during the early chondrocyte differentiation. *J Cell Sci* 110 (Pt 18): p. 2261-70

58.   Alberts B, Wilson JH, and Hunt T, (2008). Molecular biology of the cell. 5th ed. 2008, New York: *Garland Science*. xxxiii, 1601, 90 p.

59.   Burridge K and Connell L. (1983). A new protein of adhesion plaques and ruffling membranes. *J Cell Biol* 97(2): p. 359-67

60.   Choi CK, Vicente-Manzanares M, Zareno J, Whitmore LA, Mogilner A, and Horwitz AR. (2008). Actin and alpha-actinin orchestrate the assembly and maturation of nascent adhesions in a myosin II motor-independent manner. *Nat Cell Biol* 10(9): p. 1039-50

61.   Nagano T, Yoneda T, Hatanaka Y, Kubota C, Murakami F, and Sato M. (2002). Filamin A-interacting protein (FILIP) regulates cortical cell migration out of the ventricular zone. *Nat Cell Biol* 4(7): p. 495-501

62.   Lo SH, Janmey PA, Hartwig JH, and Chen LB. (1994). Interactions of tensin with actin and identification of its three distinct actin-binding domains. *J Cell Biol* 125(5): p. 1067-75

63.   Mitra SK, Hanson DA, and Schlaepfer DD. (2005). Focal adhesion kinase: in command and control of cell motility. *Nat Rev Mol Cell Biol* 6(1): p. 56-68

64.   Parsons JT. (2003). Focal adhesion kinase: the first ten years. *J Cell Sci* 116(Pt 8): p. 1409-16

65.   Feramisco JR, Smart JE, Burridge K, Helfman DM, and Thomas GP. (1982). Co-existence of vinculin and a vinculin-like protein of higher molecular weight in smooth muscle. *J Biol Chem* 257(18): p. 11024-31

66.   Turner CE. (2000). Paxillin interactions. *J Cell Sci* 113 Pt 23: p. 4139-40

67.   Schaller MD. (2001). Paxillin: a focal adhesion-associated adaptor protein. *Oncogene* 20(44): p. 6459-72

68.   Caswell PT, Vadrevu S, and Norman JC. (2009). Integrins: masters and slaves of endocytic transport. *Nat Rev Mol Cell Biol* 10(12): p. 843-53

69.   Krause M, Dent EW, Bear JE, Loureiro JJ, and Gertler FB. (2003). Ena/VASP proteins: regulators of the actin cytoskeleton and cell migration. *Annu Rev Cell Dev Biol* 19: p. 541-64

70.   Huveneers S and Danen EH. (2009). Adhesion signaling - crosstalk between integrins, Src and Rho. *J Cell Sci* 122(Pt 8): p. 1059-69

71. Hernandez SE, Krishnaswami M, Miller AL, and Koleske AJ. (2004). How do Abl family kinases regulate cell shape and movement? *Trends Cell Biol* 14(1): p. 36-44

72. Hall A. (1998). Rho GTPases and the actin cytoskeleton. *Science* 279(5350): p. 509-14

73. Harris A, Wild P, and Stopak D. (1980). Silicone rubber substrata: a new wrinkle in the study of cell locomotion. *Science* 208: p. 177-9

74. Edwards DC, Sanders LC, Bokoch GM, and Gill GN. (1999). Activation of LIM-kinase by Pak1 couples Rac/Cdc42 GTPase signalling to actin cytoskeletal dynamics. *Nat Cell Biol* 1(5): p. 253-9

75. Huang C, Jacobson K, and Schaller MD. (2004). A role for JNK-paxillin signaling in cell migration. *Cell Cycle* 3(1): p. 4-6

76. Shroff H, White H, and Betzig E. (2008). Photoactivated localization microscopy (PALM) of adhesion complexes. *Curr Protoc Cell Biol* Chapter 4: p. Unit 4 21

77. Shroff H, Galbraith CG, Galbraith JA, White H, Gillette J, Olenych S, Davidson MW, and Betzig E. (2007). Dual-color superresolution imaging of genetically expressed probes within individual adhesion complexes. *Proc Natl Acad Sci U S A* 104(51): p. 20308-13

78. Shtengel G, Galbraith JA, Galbraith CG, Lippincott-Schwartz J, Gillette JM, Manley S, Sougrat R, Waterman CM, Kanchanawong P, Davidson MW, Fetter RD, and Hess HF. (2009). Interferometric fluorescent super-resolution microscopy resolves 3D cellular ultrastructure. *Proc Natl Acad Sci U S A* 106(9): p. 3125-30

79. Kanchanawong P, Shtengel G, Pasapera AM, Ramko EB, Davidson MW, Hess HF, and Waterman CM. (2010). Nanoscale architecture of integrin-based cell adhesions. *Nature* 468(7323): p. 580-4

80. Wegener KL, Partridge AW, Han J, Pickford AR, Liddington RC, Ginsberg MH, and Campbell ID. (2007). Structural basis of integrin activation by talin. *Cell* 128(1): p. 171-82

81. Kim M, Carman CV, and Springer TA. (2003). Bidirectional transmembrane signaling by cytoplasmic domain separation in integrins. *Science* 301(5640): p. 1720-5

82. Laukaitis CM, Webb DJ, Donais K, and Horwitz AF. (2001). Differential dynamics of alpha 5 integrin, paxillin, and alpha-actinin during formation and disassembly of adhesions in migrating cells. *J Cell Biol* 153(7): p. 1427-40

83. Webb DJ, Parsons JT, and Horwitz AF. (2002). Adhesion assembly, disassembly and turnover in migrating cells -- over and over and over again. *Nat Cell Biol* 4(4): p. E97-100

84. Ilic D, Furuta Y, Kanazawa S, Takeda N, Sobue K, Nakatsuji N, Nomura S, Fujimoto J, Okada M, and Yamamoto T. (1995). Reduced cell motility and enhanced focal adhesion contact formation in cells from FAK-deficient mice. *Nature* 377(6549): p. 539-44

85. Webb DJ, Donais K, Whitmore LA, Thomas SM, Turner CE, Parsons JT, and Horwitz AF. (2004). FAK-Src signalling through paxillin, ERK and MLCK regulates adhesion disassembly. *Nat Cell Biol* 6(2): p. 154-61

86. Baruzzi A, Iacobucci I, Soverini S, Lowell CA, Martinelli G, and Berton G. (2010). c-Abl and Src-family kinases cross-talk in regulation of myeloid cell migration. *FEBS Lett* 584(1): p. 15-21

87. Small JV and Kaverina I. (2003). Microtubules meet substrate adhesions to arrange cell polarity. *Curr Opin Cell Biol* 15(1): p. 40-7

88. Broussard JA, Webb DJ, and Kaverina I. (2008). Asymmetric focal adhesion disassembly in motile cells. *Curr Opin Cell Biol* 20(1): p. 85-90

89. Huang C. (2010). Roles of E3 ubiquitin ligases in cell adhesion and migration. *Cell Adh Migr* 4(1): p. 10-8

90. Liotta LA, Steeg PS, and Stetler-Stevenson WG. (1991). Cancer metastasis and angiogenesis: an imbalance of positive and negative regulation. *Cell* 64(2): p. 327-36

91. Carragher NO, Levkau B, Ross R, and Raines EW. (1999). Degraded collagen fragments promote rapid disassembly of smooth muscle focal adhesions that correlates with cleavage of pp125(FAK), paxillin, and talin. *J Cell Biol* 147(3): p. 619-30

92. Linder S. (2007). The matrix corroded: podosomes and invadopodia in extracellular matrix degradation. *Trends Cell Biol* 17(3): p. 107-17

93. Krylyshkina O, Anderson KI, Kaverina I, Upmann I, Manstein DJ, Small JV, and Toomre DK. (2003). Nanometer targeting of microtubules to focal adhesions. *J Cell Biol* 161(5): p. 853-9

94. Kaverina I, Krylyshkina O, and Small JV. (1999). Microtubule targeting of substrate contacts promotes their relaxation and dissociation. *J Cell Biol* 146(5): p. 1033-44

95. Ezratty EJ, Bertaux C, Marcantonio EE, and Gundersen GG. (2009). Clathrin mediates integrin endocytosis for focal adhesion disassembly in migrating cells. *J Cell Biol* 187(5): p. 733-47

96. Ezratty EJ, Partridge MA, and Gundersen GG. (2005). Microtubule-induced focal adhesion disassembly is mediated by dynamin and focal adhesion kinase. *Nat Cell Biol* 7(6): p. 581-90

97.	Grande-Garcia A, Echarri A, de Rooij J, Alderson NB, Waterman-Storer CM, Valdivielso JM, and del Pozo MA. (2007). Caveolin-1 regulates cell polarization and directional migration through Src kinase and Rho GTPases. *J Cell Biol* 177(4): p. 683-94

98.	del Pozo MA, Balasubramanian N, Alderson NB, Kiosses WB, Grande-Garcia A, Anderson RG, and Schwartz MA. (2005). Phospho-caveolin-1 mediates integrin-regulated membrane domain internalization. *Nat Cell Biol* 7(9): p. 901-8

99.	Vicente-Manzanares M, Zareno J, Whitmore L, Choi CK, and Horwitz AF. (2007). Regulation of protrusion, adhesion dynamics, and polarity by myosins IIA and IIB in migrating cells. *J Cell Biol* 176(5): p. 573-80

100.	Even-Ram S, Doyle AD, Conti MA, Matsumoto K, Adelstein RS, and Yamada KM. (2007). Myosin IIA regulates cell motility and actomyosin-microtubule crosstalk. *Nat Cell Biol* 9(3): p. 299-309

101.	Huttenlocher A, Palecek SP, Lu Q, Zhang W, Mellgren RL, Lauffenburger DA, Ginsberg MH, and Horwitz AF. (1997). Regulation of cell migration by the calcium-dependent protease calpain. *J Biol Chem* 272(52): p. 32719-22

102.	Worthylake RA and Burridge K. (2001). Leukocyte transendothelial migration: orchestrating the underlying molecular machinery. *Curr Opin Cell Biol* 13(5): p. 569-77

103.	Huang C, Rajfur Z, Yousefi N, Chen Z, Jacobson K, and Ginsberg MH. (2009). Talin phosphorylation by Cdk5 regulates Smurf1-mediated talin head ubiquitylation and cell migration. *Nat Cell Biol* 11(5): p. 624-30

104.	Digman MA and Gratton E. (2009). Analysis of diffusion and binding in cells using the RICS approach. *Microsc Res Tech* 72(4): p. 323-32

105.	Digman MA, Wiseman PW, Choi C, Horwitz AR, and Gratton E. (2009). Stoichiometry of molecular complexes at adhesions in living cells. *Proc Natl Acad Sci U S A* 106(7): p. 2170-5

106.	Gardel ML, Sabass B, Ji L, Danuser G, Schwarz US, and Waterman CM. (2008). Traction stress in focal adhesions correlates biphasically with actin retrograde flow speed. *J Cell Biol* 183(6): p. 999-1005

107.	Gupton SL and Waterman-Storer CM. (2006). Spatiotemporal feedback between actomyosin and focal-adhesion systems optimizes rapid cell migration. *Cell* 125(7): p. 1361-74

108.	Buccione R, Orth JD, and McNiven MA. (2004). Foot and mouth: podosomes, invadopodia and circular dorsal ruffles. *Nat Rev Mol Cell Biol* 5(8): p. 647-57

109.	Linder S, Nelson D, Weiss M, and Aepfelbacher M. (1999). Wiskott-Aldrich syndrome protein regulates podosomes in primary human macrophages. *Proc Natl Acad Sci U S A* 96(17): p. 9648-53

110. Nakahara H, Otani T, Sasaki T, Miura Y, Takai Y, and Kogo M. (2003). Involvement of Cdc42 and Rac small G proteins in invadopodia formation of RPMI7951 cells. *Genes Cells* 8(12): p. 1019-27

111. Gimona M, Buccione R, Courtneidge SA, and Linder S. (2008). Assembly and biological role of podosomes and invadopodia. *Curr Opin Cell Biol* 20(2): p. 235-41

112. Chen WT and Wang JY. (1999). Specialized surface protrusions of invasive cells, invadopodia and lamellipodia, have differential MT1-MMP, MMP-2, and TIMP-2 localization. *Ann N Y Acad Sci* 878: p. 361-71

113. Geiger B, Bershadsky A, Pankov R, and Yamada KM. (2001). Transmembrane crosstalk between the extracellular matrix--cytoskeleton crosstalk. *Nat Rev Mol Cell Biol* 2(11): p. 793-805

114. Rottner K, Hall A, and Small JV. (1999). Interplay between Rac and Rho in the control of substrate contact dynamics. *Curr Biol* 9(12): p. 640-8

115. Beningo KA, Dembo M, Kaverina I, Small JV, and Wang YL. (2001). Nascent focal adhesions are responsible for the generation of strong propulsive forces in migrating fibroblasts. *J Cell Biol* 153(4): p. 881-8

116. Galbraith CG, Yamada KM, and Sheetz MP. (2002). The relationship between force and focal complex development. *J Cell Biol* 159(4): p. 695-705

117. Riveline D, Zamir E, Balaban NQ, Schwarz US, Ishizaki T, Narumiya S, Kam Z, Geiger B, and Bershadsky AD. (2001). Focal contacts as mechanosensors: externally applied local mechanical force induces growth of focal contacts by an mDia1-dependent and ROCK-independent mechanism. *J Cell Biol* 153(6): p. 1175-86

118. Lee J and Jacobson K. (1997). The composition and dynamics of cell-substratum adhesions in locomoting fish keratocytes. *J Cell Sci* 110 (Pt 22): p. 2833-44

119. Anderson KI and Cross R. (2000). Contact dynamics during keratocyte motility. *Curr Biol* 10(5): p. 253-60

120. Lee J, Leonard M, Oliver T, Ishihara A, and Jacobson K. (1994). Traction forces generated by locomoting keratocytes. *J Cell Biol* 127(6 Pt 2): p. 1957-64

121. de Beus E and Jacobson K. (1998). Integrin involvement in keratocyte locomotion. *Cell Motil Cytoskeleton* 41(2): p. 126-37

122. Chan CE and Odde DJ. (2008). Traction dynamics of filopodia on compliant substrates. *Science* 322(5908): p. 1687-91

123. Maruthamuthu V, Aratyn-Schaus Y, and Gardel ML. (2010). Conserved F-actin dynamics and force transmission at cell adhesions. *Curr Opin Cell Biol* 22(5): p. 583-8

124. Machacek M, Hodgson L, Welch C, Elliott H, Pertz O, Nalbant P, Abell A, Johnson GL, Hahn KM, and Danuser G. (2009). Coordination of Rho GTPase activities during cell protrusion. *Nature* 461(7260): p. 99-103

125. Nalbant P, Hodgson L, Kraynov V, Toutchkine A, and Hahn KM. (2004). Activation of endogenous Cdc42 visualized in living cells. *Science* 305(5690): p. 1615-9

126. Pertz O and Hahn KM. (2004). Designing biosensors for Rho family proteins--deciphering the dynamics of Rho family GTPase activation in living cells. *J Cell Sci* 117(Pt 8): p. 1313-8

127. Dembo M, Oliver T, and Jacobson K. (1996). Imaging the traction stresses exerted by locomoting cells with the elastic substratum method. *Biophysical Journal* 70: p. 2008-2022

128. Oliver T, Dembo M, and Jacobson K. (1999). Separation of propulsive and adhesive traction stresses in locomoting keratocytes. *The Journal of Cell Biology* 145(3): p. 589-604

129. Butler JP, Tolic-Norrelykke IM, Fabry B, and Fredberg JJ. (2002). Traction fields, moments, and strain energy that cells exert on their surroundings. *Am J Physiol Cell Physiol* 282(3): p. C595-605

130. Wang Y-L, Dembo M, Wang H-B, and Lo C-M. (2000). Cell Movement Is Guided by the Rigidity of the Substrate. *Biophysical Journal* 79: p. 144-152

131. Pelham RJ and Wang Y-L. (1997). Cell locomotion and focal adhesions are regulated by substrate flexibility. *Proc. Natl. Acad. Sci. USA* 94(25): p. 13661-13665

132. Pelham R and Wang Y. (1999). High resolution detection of mechanical forces exerted by locomoting fibroblasts on the substrate. *Mol. Biol. Cell* 10(4): p. 933-945

133. Lo CM, Wang HB, Dembo M, and Wang YL. (2000). Cell movement is guided by the rigidity of the substrate. *Biophysical Journal* 79(1): p. 144-152

134. Dembo M and Wang Y-L. (1999). Stresses at the cell-to-substrate interface during locomotion of fibroblasts. *Biophysical Journal* 76: p. 2307-2316

135. Wang YL and Pelhan RJ. (1998). Preparation of a flexible, porous polyacrylamide substrate for mechanical studies of cultured cells. *Methods in Enzymology* 298: p. 489-496

136. Galbraith CG and Sheetz MP. (1997). A micromachined device provides a new bend on fibroblast traction forces. *Proc Natl Acad Sci U S A* 94(17): p. 9114-8

137. Galbraith CG and Sheetz MP. (1999). Keratocytes pull with similar forces on their dorsal and ventral surfaces. *J Cell Biol* 147(6): p. 1313-24

138.   Tan JL, Tien J, Pirone DM, Gray DS, Bhadriraju K, and Chen CS. (2003). Cells lying on a bed of microneedles: an approach to isolate mechanical force. *Proc Natl Acad Sci U S A* 100(4): p. 1484-9

139.   Balaban NQ, Schwarz US, Riveline D, Goichberg P, Tzur G, Sabanay I, Mahalu D, Safran S, Bershadsky A, Addadi L, and Geiger B. (2001). Force and focal adhesion assembly: a close relationship studied using elastic micropatterned substrates. *Nat Cell Biol* 3(5): p. 466-72

140.   Jurado C, Haserick JR, and Lee J. (2005). Slipping or gripping? Fluorescent speckle microscopy in fish keratocytes reveals two different mechanisms for generating a retrograde flow of actin. *Mol Biol Cell* 16(2): p. 507-18

CHAPTER 3

A profound change in cell shape and migration induced by Abl family kinases inhibitor[1]

3.1 SUMMARY

The issue of how contractility and adhesion are related to cell shape and migration pattern remains largely unresolved. In this paper we report that Gleevec (Imatinib), an Abl family kinase inhibitor, produces a profound change in the shape and migration of rat bladder tumor cells (NBTII) plated on collagen-coated substrates. Cells treated with Gleevec adopt a highly spread D-shape and migrate more rapidly with greater persistence. Accompanying this more spread state is an increase in integrin-mediated adhesion coupled with increases in the size and number of discrete adhesions. In addition, both total internal reflection fluorescence microscopy (TIRFM) and interference reflection microscopy (IRM) revealed a band of small punctate adhesions with rapid turnover near the cell leading margin. These changes led to an increase in global cell-substrate adhesion, as assessed by laminar flow experiments. Gleevec-treated cells have

greater RhoA activity which, via myosin activation, led to an increase in the magnitude of total traction force applied to the substrate. These chemical and physical alterations upon Gleevec-treatment produce the dramatic change in morphology and migration that is observed.

3.2 INTRODUCTION

The study of cell migration is essential for understanding a variety of processes including wound repair, immune response and tissue homeostasis, and, importantly, aberrant cell migration can result in various pathologies (1-3). However, the relationship between cytoskeletal dynamics, including actin network growth, contractility, and adhesion to cell shape and migration remains incompletely understood.

Abl family tyrosine kinases are ubiquitous non-receptor tyrosine kinases (NRTKs) involved in signal transduction (4-6). They can interact with other cellular components through multiple functional domains for F and G actin binding, as well as through binding phosphorylated tyrosine's (SH2), polyproline rich regions (SH3), DNA (Abl), and microtubules (Abl Related Gene (Arg)) (7, 8). Abl family tyrosine kinases have also been found to regulate cell migration (8, 9). In some cases, Abl family kinases have been reported to promote actin polymerization and migration (10) as well as filopodia formation during cell spreading (11, 12). By contrast, in other studies Abl was found to restrain lamellipodia extension (13, 14) or inhibit initial cell attachment to the substrate (15). Abl family kinases have been suggested to regulate cell adhesion size and stress fiber formation (16); Li and Pendergast recently reported that the Abl family member Arg , could disrupt CrkII-C3G complex formation to reduce β1-integrin related adhesion formation (17). Thus, a complete understanding of how Abl family kinases regulate cell migration is lacking (8, 9).

43

In this study, we report that Gleevec (also called Imatinib/STI571), an Abl family kinase inhibitor that is used as a chemo-therapeutic agent for leukemia, produces a profound change in the shape and migration of the rat Nara bladder tumor (NBT-II) cells plated on collagen-coated substrates. Within 20min of Gleevec treatment the majority of NBT-II cells develop a new D-shaped morphology and start migrating more rapidly and with greater persistence. The new morphology is characterized by stronger cell-substrate adhesion and an increase in the size and number of discrete adhesions which at the leading margin turnover more rapidly. RhoA activity in Gleevec-treated cells was increased which, via myosin activation, led to an increase in the magnitude of total traction forces applied to the substrate. Upon Gleevec treatment, these chemical and physical alterations combined to produce the dramatic change in morphology and migration.

3.3 MATERIALS AND METHODS

3.3.1 Antibodies and Immunofluorescence

Antibodies: Integrin β-1 (CD29) blocking antibody anti-Mouse/Rat CD29 (HMβ1-1 BD. Biosciences Pharmingen, San Diego, CA), anti-α-Tubulin Antibody (#2144; Cell Signaling Technology, Beverly, MA), anti-phospho-myosin Light Chain II antibody (against Ser19, #3671, Cell Signaling Technology, Beverly, MA), anti-Rac1 antibody (#2465; Cell Signaling Technology, Beverly, MA), anti-Cdc42 antibody (#2462; Cell Signaling Technology, Beverly, MA), anti-RhoA antibody(sc-418; Santa Cruz Biotechnology, Santa Cruz, MA).

For immuno-staining, NBTII cells were fixed by using paraformaldehyde solution [4 % (w/v) in PBS, pH 7.4] for 20 minutes at 25°C. Cells were then permeabilized with PBS containing 0.05 % Triton-X-100 for 5 minutes at 25°C. Fluorescence labeling was carried out by treating with primary antibodies, washing with medium and then treating with fluorescent secondary antibodies followed by washing. Imaging was done as described below.

3.3.2 Cell culture and transfection

NBT-II cells were acquired from the ATCC (Manassas, VA) and maintained in DMEM/F-12 medium (Gibco, Grand Island, NY) containing 10% FBS, 100 units/ml penicillin and 100 μg/ml streptomycin. The EGFP-Paxillin-β and EGFP-Vinculin construct were generated by subcloning DNA fragments expressing wild-type paxillin and wild type vinculin into a pEGFP-C vector (Clontech, Mountain View, CA). NBT-II cells were transfected using the Lipofectamine Plus transfection reagent (Invitrogen, Carlsbad, CA) according to the manufacturer's protocol. Cells stably expressing either EGFP-Paxillin-β or EGFP-Vinculin were obtained by sorting for EGFP positive cells after G418 selection in the UNC Flow Cytometry Facility.

3.3.3 Cell migration, surface coating and drug treatment

For the experiments imaging the migration of NBT-II cells, glass bottom Petri dishes (35 mm) (MatTek) were coated by incubating with 10μg/ml type I collagen (BD Biosciences, Bedford, MA) overnight at 4°C. NBT-II cells were treated with trypsin and resuspended in DMEM/F12 medium (GIBCO) containing 10% fetal bovine serum, plated

at low density on the dishes, and cultured for 4-12 h in a CO_2 incubator. Cells were incubated with either no inhibitor, or various concentrations of the 20μM Abl family inhibitor Gleevec® (Novartis, Basel, Switzerland) by adding the inhibitor to culture media which was mixed by gently pipetting up and down. The cells were incubated for 30 minutes prior to imaging and imaging was performed in the continued presence of the inhibitor.

5μM ROCK inhibitor(Y-27632, Sigma, MO) or 2μg/ml of Rho inhibitor, C3 transferase (Cytoskeleton Inc., Denver, CO), was used to inhibit ROCK or Rho activity in Gleevec pre-treated NBTII cells for 30 minutes. 100μg/ml RGD-containing peptide (Gly-Arg-Gly-Asp-Thr-Pro) (G5646, SIGMA), or 1μg/ml anti-Mouse/Rat CD29 (Biosciences Pharmingen, CA) was used to block integrin related cell adhesion. Cell migration status was studied after one hour of incubation with these inhibitors.

3.3.4 Assay for active RhoA GTPases

Active RhoA pulldown experiments were done as described previously (18). For active RhoA pulldown cells were lysted in 300 μl 50 mM Tris, pH 7.4, 10 mM MgCl2, 500 mM NaCl, 1% Triton X-100, 0.1% SDS, 0.5% deozycholate, 1 mM PMSF, and 10 μg/ml each of aprotinin and leupeptin. Lysates were cleared by centrifugation at 14,000 g for 5 min. Supernatants were rotated for 20 minutes with 30-50 μg GST-RBD conjugated to glutathione–Sepharose beads (GE Healthcare). Beads were washed with in μl 50 mM Tris, pH 7.4, 10 mM MgCl2, 150 mM NaCl, 1% Triton X-100, 1 mM PMSF, and 10 μg/ml each of aprotinin and leupeptin. Active RhoA and total RhoA levels were analyzed by SDS-PAGE. Gel intensity results were quantified by analyzing inverted images using

ImageJ. The signal from protein bands was measured after background subtraction and the intensity of each image was then normalized according to the average signal of loading control band.

3.3.5 Cell imaging

Differential Interference Contrast (19)Total Internal Reflection (TIRF) and epi-fluoresence imaging was carried out on a dual-channel Olympus IX81 inverted microscope equipped with a 60×, oil immersion, 1.45 NA objective. Interference Reflection Microscopy imaging was performed using a 100×, oil immersion, 1.65 NA objective. Objective (x60) style TIRFM was performed on the Olympus IX81 with the Olympus TIR option. Images were captured using an air-cooled SensiCam QE CCD camera (Cooke Corp., Romulus, MI) driven by Metamorph (Molecular Devices/Meta Imaging, Downingtown, PA). Confocal imaging was performed with an inverted Olympus FV1000 equipped with a live cell chamber and a 60× 1.42 N.A. oil immersion objective. Migration of single cells was tracked for durations between 5 minutes to 2 hours; time-lapse images were taken with the intervals of 1 second (for morphology changes), 5 seconds (for rapid adhesion turnover) or 60 seconds (for cell migration and long lifetime adhesion turnover), as indicated.

3.3.6 Measurement of cell adhesion strength

A flow system designed to produce laminar shear stress on attached NBTII cells consisted of a flow cell, a dual syringe pump (Harvard Apparatus, Holliston, MA), 5% CO_2 percolated media reservoir, and a pulse dampener (Cole Parmer Instrument Company, Chicago, IL) as previously described in detail (20, 21). Briefly, a two-piece,

top and bottom plate, anodized aluminum flow cell (12 × 7.5 cm) was constructed with plastic inlet and outlet tubes. The Nunc SlideFlask (Thermo) on which NBT-II cells were plated was placed in the middle of the flow cell bottom plate with a 0.27-mm thick silicone gasket placed underneath it. This brought the coverslip to the same height as the top of the bottom plate. Shear stress was calculated using the following equation:

$$\tau_w = \frac{6\mu Q}{wh^2}$$

where μ is the viscosity of 0.0086 g.cm/s, Q is the flow rate in mL/s, w is the width of the flow channel (1.7 cm), and h is the height of the flow channel (0.027 cm). The applied shear stress ranged from 100 to 253 dynes/cm^2.

Cells were cultured for 4 hours on 10 μg/ml pre-coated collagen Nunc SlideFlask (Thermo) substrates; and labeled with 1:1000 Cell tracker orange (Invitrogen, Carlsbad, CA) for 10 minutes 30 minutes before flow experiments. All flow experiments were performed at 37 °C for 1 minute with PBS containing calcium and magnesium. In each experiment, multiple (10-20) images were taken showing cells in different regions of the flow chamber, before and after shear stress was applied. The cell attached to substrate before and after shear stress were counted, expressed as the percent of adherent cells remaining, and averaged over multiple experiments. Data were reported as mean ± SEM.

3.3.7 Traction force microscopy

Preparation of polyacrylamide substrates and experimental imaging has been described previously (22). Briefly, the fabrication of polyacrylamide substrate involves following three steps: 1) Silanization the glass substrate with 0.5% silane for 20 minutes,

2) Use 0.5% glutaraldehyde treat previous substrate for 40minutes, 3) polymerization with 6% polyacrylamide and 1% bis-acrylamide in 10 mM HEPES buffer with rhodamine-dextran beads and NHS-acrylate. Polymerization is initiated with the addition of 0.05g/ml APS. The elastic modulus of our substrate was measured to be approximately 48kPa (22). Elastic substrates after polymerization were stored at 4°C in PBS. Tractions were calculated using the method of Butler et al (2002) in which particle imaging velocimetry is employed to measure the displacement of small windows that contain a number of beads.

3.3.8 Data quantification and calculation

The movement of individual cells was analyzed with Metamorph software and ImageJ.

A. Speed and persistence of migration: Cell speed was measured with ImageJ using the Manual Tracking plug-in (http://rsbweb.nih.gov/ij/plugins/track/track.html). For cell migration persistence, we employed a conventional definition: the ratio of the net distanced traveled to the total distance traveled. The net distance traveled is the magnitude of the vector between the starting point and end point of the cell trajectory over an hour and the total distance traveled taken as the sum of net distances traveled over twelve 5 minutes intervals in that hour in order to capture the changes in direction that occur. Thus, the highest persistence would have a value of one, representing unidirectional migration.

49

B. Segmentation of adhesions in TIRF images: To identify focal adhesions (or other small adhesions) in each image of a time-lapse series, a set of segmentation methods were used (23). Each movie was cropped to only include one cell. Starting with the raw images from the TIRF movies, we used a high-pass filter to minimize background noise and the overall distribution of pixel intensities after high-pass filtering was used to select a threshold for adhesion detection. For all image sets examined, we selected a threshold of the mean plus two standard deviations of the high-pass filtered pixel intensities. We then applied the threshold and connected components labeling to identify each adhesion and removed any pixel objects identified less than three pixels. After identifying the adhesions, they were tracked through time using a previously published method (23) and a range of properties were collected. Adhesion properties were only calculated for adhesions where both a birth and death event was detected.

C. Lifetime of adhesions: ImageJ was used to measure changes in fluorescent intensity of individual adhesions over time in cells expressing fluorescent-tagged adhesion proteins. A perimeter was drawn around the punctate or wing adhesions at the point where intensity was a maximum; average pixel intensity was calculated from the pixel intensities within that perimeter as function of time. Background and photobleaching corrections were applied to obtain true intensities of the adhesions. Assembly and disassembly rates were plotted and calculated using Microsoft Excel (Microsoft Corporation) or Origin 6.1(OriginLab) using a previously published method (Huang et al., 2009) (Choi et al., 2008(24).

D. Quantification of collective adhesion profile: Multiple lines (n=4 for each cell, 12 cells in each group) were drawn along the cell migration direction from outside to the interior of the cell (line length=200 pixels) with the center of the line is positioned manually at leading edge. The fluorescent signal along each line was measured using PlotProfile function in ImageJ. The EGFP-Paxillin fluorescence intensity in different cells was not uniform. In order to better compare the profile of collective adhesion intensities between control and Gleevec-treated cells, background (S_{bgd}) was subtracted from the raw fluorescence intensity profile (for each pixel S(n))and then these profiles were normalized. We used following formulae to get the normalized relative signal intensity ($S_{rsi-Line}$(n)) for the n_{th} pixel (n=1 to 200) along the line:

$$S_{avg} = \frac{\sum_{n=1}^{200} S(n)}{200} - S_{bgd}$$

$$S_{rsi-Line}(n) = \frac{S(n) - S_{bgd}}{S_{avg}}$$

,where S_{avg} represents average pixel intensity averaged along the entire line.

3.4 RESULTS

3.4.1 Treatment with Gleevec induces a D-shaped morphology in NBTII cells

The morphology of a migrating cell is related to cell migration modes. NBTII is a rat-derived carcinoma cell line (25). A normal cultured NBTII cell shows typical epithelial morphology; however, when NBTII cells were cultured on type I collagen-coated plastic cell culture dishes for 4–12 h, they acquired a polarized shape and migrate individually, exhibiting an epithelial to mesenchymal transition (EMT) (26-29)). During our experiments, we observed that NBTII cells on collagen had medium-sized lamellae, multiple filopodia dynamically formed at the leading edge of the cell, and multiple retraction fibers formed at the rear end of the cell. (**Figure 3.1A, Supplemental Movie 3.1**). A number of retraction fibers can be observed at the trailing edge of the cell. **Figure 3.1B** shows NBTII cells cultured on type I collagen for 8 h and then treated with 20μM Gleevec, an inhibitor of the Abl family of NRTK (Novartis, Stein, Switzerland) for 30 minutes (30, 31)). Within 5 minutes of Gleevec addition, a profound change in cell morphology can be observed (**Supplemental Movie 3.2**). Cells began to form lamellipodial protrusions, which usually merged into a single, intact lamellium facing the migration direction (**Supplemental Movie 3.3**). This cell morphology may persist for over 8 hours. After Gleevec treatment, cells had markedly reduced numbers of both filopodia and retraction fibers. The actin and microtubule cytoskeleton of NBTII cells or Gleevec-treated NBTII cells differed somewhat (**Figure 3.1C** and **3.1D);** particularly noticeable were the number of f-actin rich retraction fibers in the control cells. Gleevec treated NBTII cells had about a 75% increase in migration speed compared with control

52

NBTII cells (**Figure 3.1E)** and maintained their direction significantly better than control

NBTII cells (**Figure 3.1F and Supplemental Movie 3.4).**
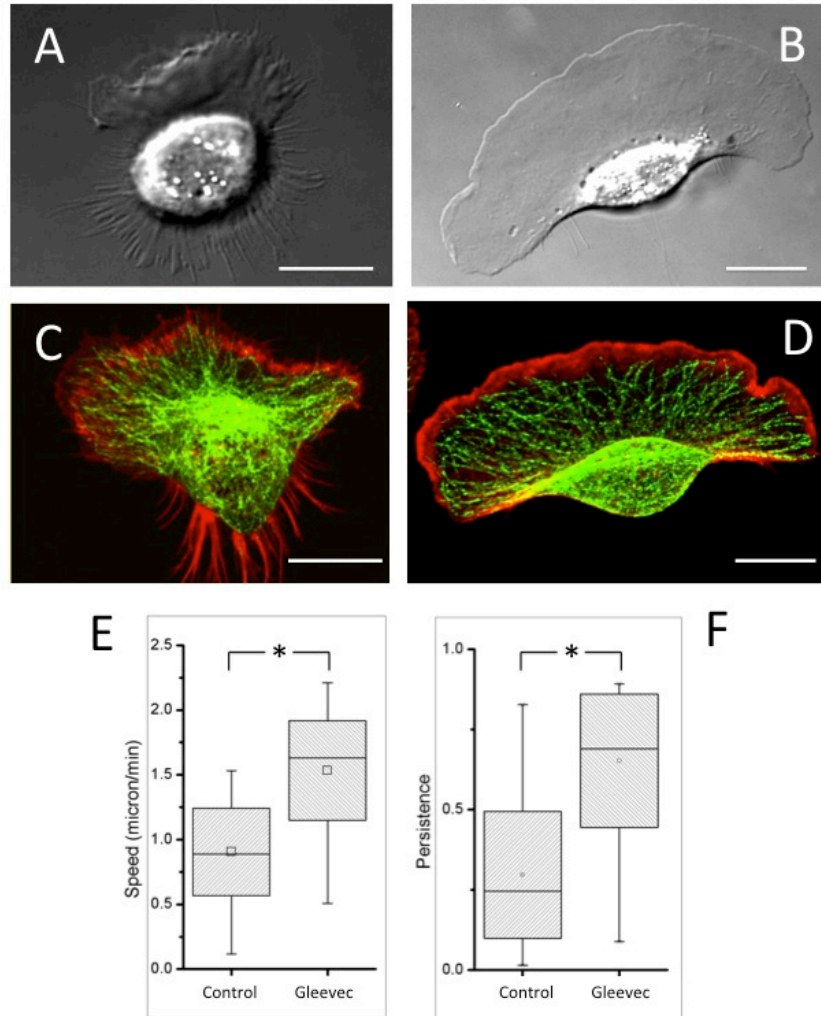
Figure 3.1. Transformation of NBT-II cells morphology and migratory phenotype after Gleevec treatment. A and B) Representative DIC images of NBT-II cells plated on 10 μg/ml collagen coated substrate. Control cell (A) and cell treated for 30 min with 20 μM Gleevec. (B) Note that a lamellipodial protrusion and a D- (or fan) shaped morphology occurs within 10 minutes of exposure to the Abl-family inhibitor. (C and D) Confocal fluorescent images of the f-actin (Rhodamine-phalloidin, Red) and microtubules (alpha-tubulin antibody, Green) in the control (C) and Gleevec-treated cells (D). (E and F) Box and whisker plots of the average cell migration speed (E) and directional persistence (F) for the control group (N=60) and NBT-II cells treated with 20 μM Gleevec (N=60). Standard deviations are indicated by the box sizes; maximum and minimum data values are indicated by the extent of the whiskers. The bar and the square inside the box are the median and mean value respectively. Gleevec-treated NBTII cells

53

migrate significantly faster and are more persistent in their directionality (* $p<0.001$, by students *t*-test). Scale bars are 20 μm.

Gleevec treatment induced a pronounced change in cell morphology when compared to control cells (**Figure 3.1 and Supplemental Movies 3.1, 3.2, 3.3**). To better determine the changes in cell morphology, we used four parameters as defined in **Figure 3.2B**: (1) *Aspect ratio*, the ratio of the widest dimension of the cell in the direction perpendicular to the direction of migration divided by the longest dimension of the cell in the direction of cell migration; (2) *Nuclear aspect ratio*, the aspect ratio of the cell nuclear region ; (3) *Area ratio*, the ratio of the total cell area to the nuclear area; and (4) *Retraction fiber length,* the population average of the sum of the length of all retraction fibers in one individual cell divided by the same parameter calculated for the control cells. This parameter is the product of the number of retraction fibers and their length and provides a quantitative measure over a population of cells. The results of our analysis revealed that cells treated with Gleevec had significantly increased aspect ratio, nuclear ratio, and area ratio, while having a reduced retraction fiber length ratio (**Figure 3.2A**). Interestingly, unlike most known mesenchymal migrating cells, which are typically elongated in the direction of migration, Gleevec treated cells were elongated in the direction perpendicular to their movement and showed visual similarity to fish or amphibian keratocytes (32-34) **(Figure 3.1B and Supplemental Movies 3.3, 3.4)**.
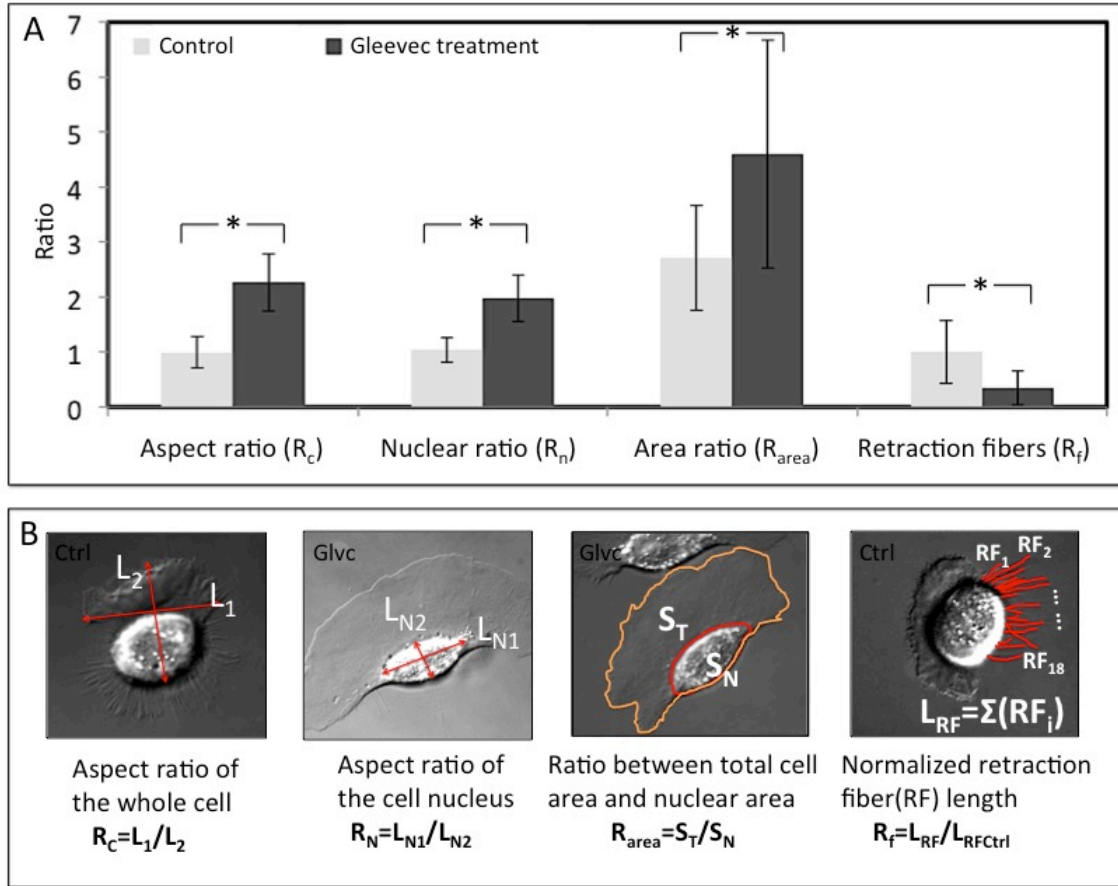
Figure 3.2. Detailed analysis of cell morphology changes after Gleevec treatment. A) Cell morphology parameters (see text) were analyzed and compared between NBT-II cells from the control group and the group treated with 20 μM Gleevec. B) Schematic figures depicting the calculation of each cell morphology parameter. The 1st and 4th cells from the left, shown in panel B, are samples of control NBT-II cells; while the 2nd and 3rd cells depict NBT-II cells that have been treated with Gleevec. Data are calculated from more than 50 cells for each group. Control and Gleecec treated cells are significantly different in all four parameters (* p<0.001, by student's *t*-test).

3.4.2 Both Gleevec concentration and substrate adhesiveness affect NBTII cell migration

To investigate the NBTII cell dose response for Gleevec concentration we determined migration speed and persistence for NBTII cells treated with different concentrations of Gleevec. Cells were plated on substrates coated with 10μg/ml collagen.

The concentration of Gleevec employed to inhibit Abl family kinase activity was in the range of 0.25μM to 50μM. The average cell migration speed reached a maximum (~2 μm/min), when a 20μM concentration of Gleevec was used. For lower Gleevec concentrations (0.25 μM, 1 μM), cells did not show a significant speed increase. The highest concentration of Gleevec (50μM) actually caused cell migration speed to decrease (**Figure 3.3A**). The ability of NBTII cells to migrate persistently in one direction was also highest after treatment with 20μM of Gleevec (**Figure 3.3B**).

To investigate how the substrate adhesiveness influences NBTII cell migration, we tested different concentrations of collagen for substrate coating. Substrate adhesiveness increases with collagen coating concentration. For these experiments we used control NBTII cells and cells treated with a 20μM concentration of Gleevec. For control NBTII cells, when the collagen coating concentration was increased from 1μg/ml to 100μg/ml, both the migration speed (**Figure 3.3C**) and persistence (**Figure 3.3D**) increased. For the Gleevec-treated NBTII cells, the speed of migration was greatest on the substrates with medium and higher adhesivity (10 and 100μg/ml collagen). The largest difference in speed and persistence between control and Gleevec treated NBTII cells occurred at a 20μM of Gleevec concentration on 10μg/ml of collagen coated substrates.
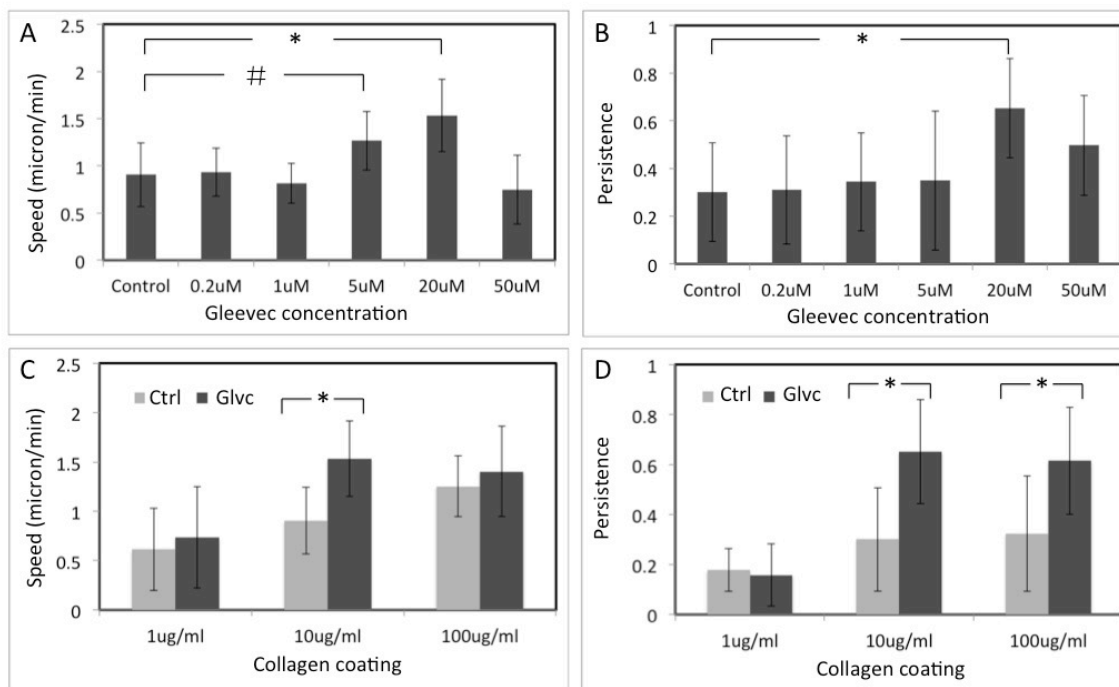
Figure 3.3. NBTII cell migration behavior depends on substrate adhesiveness and Gleevec concentration. A) and B) Graphs depicting the average cell migration speed (A) and persistence (B) of NBT-II cells from the control group (no inhibitor) and NBT-II cells treated with different concentrations of Abl family kinase inhibitor (Gleevec). Cells were cultured on 10 μg/ml collagen coated substrates. Cells treated with 20 μM Abl kinase inhibitor migrated faster and persistently. C) and D) Graphs depicting the average cell migration speed (C) and persistence (D) of NBT-II cells on substrates coated with 1 μg/ml, 10 μg/ml, and 100 μg/ml collagen. The average migration speed and persistence of control and Gleevec cells are presented with gray and black bars, respectively. Results are calculated from more than 30 cells in each group. The error bars indicate standard deviations. (* $p<0.001$, by students *t*-test; # $p<0.01$ by students t-test).

3.4.3 Gleevec treated NBTII cells are more adherent to their substrate than control cells

The highly spread lamella of Gleevec treated NBT II cells suggested that they had become more adhesive. Therefore, we investigated cell adhesion strength using a laminar flow system reported previously (20, 21). Basically, by varying the flow rate, the system generates various shear stresses on cells attached in the flow channel. When applied shear

57

stress overcomes the global cell adhesion strength, cells will detach from the channel and be removed by flow (**Figure 3.4A**). Images showing the cells attached before and after flow application were recorded and cell numbers were counted (**Materials and Methods, Supplemental Figure 3.1**). For our experiments, we tested 100 dynes/cm^2, 200 dynes/cm^2 and 253 dynes/cm^2 values of shear stress (**Supplemental Figure 3.1**). We found that a shear stress of 200 dynes/cm^2 is the most appropriate for estimation of the relative NBTII cell adhesion strength. A shear stress of the 100 dynes/cm^2 was too weak to affect cell attachment and a shear stress of 253 dynes/cm^2 quickly removed most of the attached cells. We applied 200 dynes/cm^2 shear stress for 1 min to the control and Gleevec-treated NBTII cells which were plated on 10μg/ml collagen for 4 hours. The fraction of the remaining adherent cells was significantly larger for the cells treated with Gleevec (**Figure 3.4A**). This result indicates that the global adhesion strength between cells and collagen substrates was increased after inhibition of Abl family kinases.

We further transfected NBTII cells with GFP-Paxillin to indicate adhesions and employed total internal reflection fluorescence microscopy (TIRFM) to monitor GFP-Paxillin localization on the ventral surface of the cell. Adhesions were automatically tracked and measured by an algorithm developed in a previous report (**Materials and Methods**) (35). Compared to control NBTII cells (**Figure 3.4B**), Gleevec treated cells (**Figure 3.4C**) had an increased number of adhesions at their leading edge and wings; in addition, the total adhesion number increased by ~25%(**Figure 3.4D**) and the total adhesion area increased by ~70% (**Figure 3.4E**). Gleevec treated cells had their average adhesion size increased by more than 20% (data not shown).
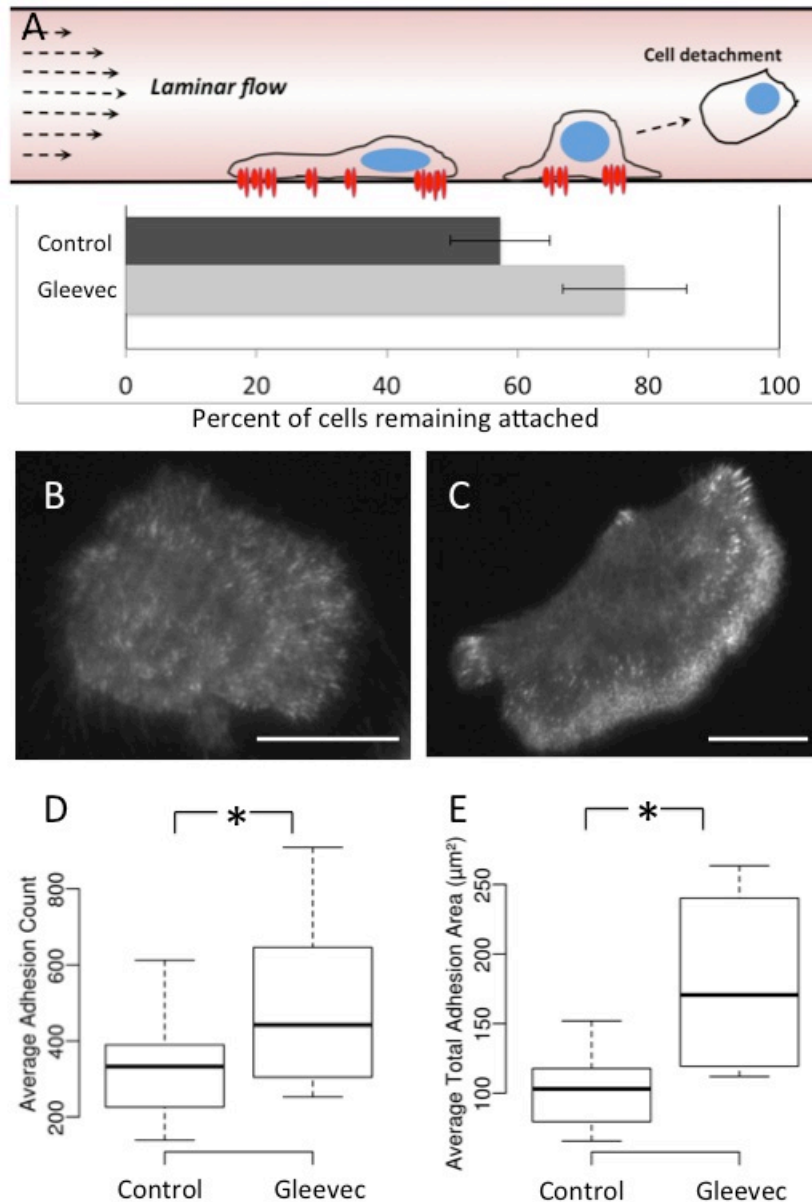
Figure 3.4. Gleevec treated cells are more adhesive than control cells. A) A schematic figure (top panel) showing the measurement of cell adhesion strength using a laminar flow system. As the laminar flow rate is increased, more cells detach. Cells were cultured for 4 hours on 10 μg/ml pre-coated collagen Nunc SlideFlask (Thermo) substrates. The fraction of adherent cells retained after exposure to shear stress of 200 dynes/cm^2 for 1 min (N = 5; n = 11–20 images per N) is shown in the horizontal bar graph. The group of cells treated with 20 μM of Gleevec has significantly higher number of remaining cells after laminar flow exposure (p<0.01). B) and C) are GFP-Paxillin TIRFM images for control NBT-II cells and Gleevec-treated NBT-II cells, respectively. Scale bars are 20 μm. D) and E) are the graphs depicting the average number of adhesions and average total area covered by adhesions in control and Gleevec-treated cells, respectively. Cells that have been treated with Gleevec have significantly larger total adhesion

area (p < 0.01, N>15 cells in each group) and average number of adhesions (p < 0.01, N>15 cells in each group).

3.4.4 Punctate adhesions are present at the leading edge of Gleevec treated D-shape NBT-II cells.

TIRFM and Interference Reflection Microscopy were combined to capture time-lapse images of adhesions in migrating NBTII cells. The darker regions in IRM image are usually considered regions which are closer to the substrate (36). In **Supplemental Figure 3.2A** and 3.**2B,** the dark regions in IRM image are generally co-localized with the GFP-Paxillin regions in the TIRFM image, indicating that those dark regions and dots are actually cell adhesions. The images of the leading edge of control and Gleevec treated NBTII cells are shown in **Figures 3.5A** to 3.**5D** and 3.**5E** to 3.**5H,** respectively. In IRM images, the small punctate adhesions were only observed in the leading edge of Gleevec-treated cells (**Figure 3.5E and 3.5F**) (**Supplemental Movie 3.6**), but not in control cells (**Figure 3.5A and 3.5B**) (**Supplemental Movie 3.5**). As shown in the TIRFM images, compared with control cells (**Figure 3.5C** and **3.5D**)(**Supplemental Movie 3.7**), D-shaped NBTII cells had a larger amount of dotted GFP-Paxillin at their leading edge (**Figure 3.5G** and **3.5H**) (**Supplemental Movie 3.8**). We measured the intensity of GFP-Paxillin along the sample lines indicated in **Figure 3.5C** and **3.5G.** For each cell, lines crossing the leading edge were summed together and normalized (**Materials and Methods**). We found that D-shaped NBTII cells had significantly increased intensity of GFP-paxillin fluorescence signal in the vicinity of the leading edge (**Figure 3.5I**). Adhesion turnover in the leading edge of a Gleevec treated cell was imaged and shown in **Supplemental Figure 3.2C** or **Supplemental Movie 3.8**. **Supplemental Figures 3.2D-**

3.2G are TIRFM images of EGFP-Paxillin in Gleevec-treated cells, showing a rim of punctate adhesions at the leading margin as a common feature. The size distribution of punctate adhesions in Gleevec-treated NBTII cells had a peak at ~350nm in diameter, and the average area of punctate was $0.1\mu m^2$. Many punctate adhesions are close to the diffraction limit so some may be even smaller in dimension. Observation of the TIRFM movies suggested that these punctate adhesions near the leading edge turned over very rapidly; indeed, intensity analysis (24) indicated an average lifetime of ~70s; by contrast, adhesions at the cell wings are much more stable with lifetimes in excess of 5 minutes (**Supplemental Figure 3.2H-3.2I**).
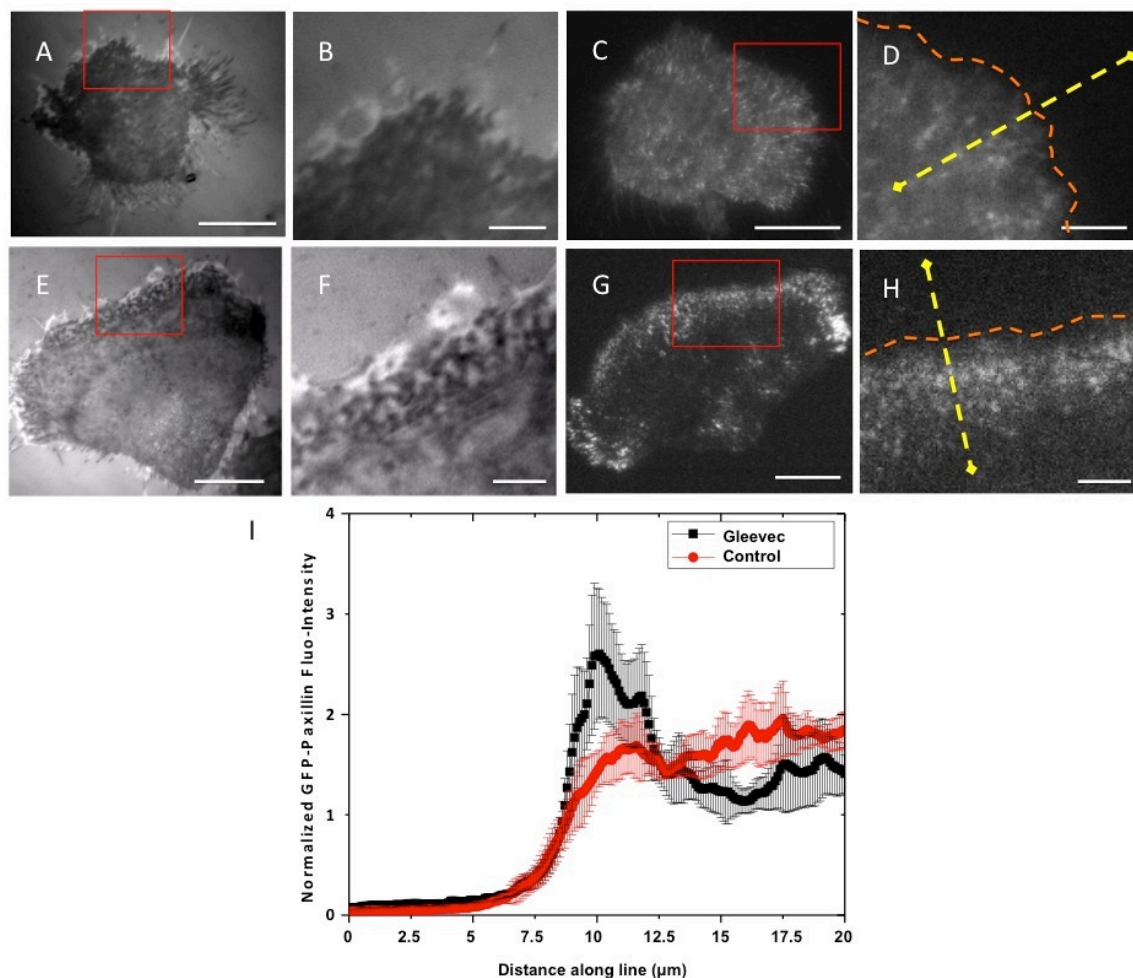
Figure 3.5. Punctuate adhesions are present at the leading edge of Gleevec treated NBT-II cells. Panel A) and E) are representative IRM images of a migrating control (A) and a Gleevec-treated (E) NBT-II cell, respectively. Dense, dynamic, punctuate adhesions are only observed at the leading edge of the Gleevec-treated cells. Red rectangles on (A) and (E) show the position where thee times magnified images (B) and (F) were taken. Panel C) and G) are representative TIRFM (Total Internal Reflection Fluorescence Microscopy) images of GFP-Paxillin expressed in control and Gleevec treated NBT-II cells, respectively. D) and H) Images resulting from amplifying the areas indicated by the red boxes in C) and G) by three times, respectively. Gleevec-treated cells form a band of GFP-Paxillin at the leading edge of the cell. The GFP-Paxillin fluorescent intensity is measured along yellow dotted lines (shown in Figure 5C and 5G) across the leading edge of the cell (4 lines for each cell). I) Multiple cells were used to calculate the distribution of normalized GFP-Paxillin intensity at the leading edge: control NBT-II cells (Black line, n=12), and D-shaped Gleevec treated NBT-II cells (red line, n=12), with the standard deviation shown as gray (for control cells) or pink bars (for Gleevec treated cells) (detailed calculations are described in Materials and Methods). Gleevec-treated cells NBT-II cells have

peak of GFP-Paxillin signal near the leading edge, while control NBT-II cells do not. Scale bars in panels A, C, E and G are 20 μm, and in B, D, F, H are 5 μm.

3.4.5 β1 integrin-containing cell adhesions are important for maintaining D-shape morphology and migration status

Next, we asked whether integrins were important for the Gleevec induced-phenotype. To competitively disrupt Integrin-collagen binding we employed two different agents: an RGD-containing peptide (Gly-Arg-Gly-Asp-Thr-Pro) (37) and direct β1 integrin blocking antibodies, because β1 integrin is known to bind type I collagen (38)((39, 40). We found that either 1μg/ml of β1 integrin blocking antibody or 100μg/ml RGD-containing peptide (G5646, SIGMA) quickly decreased cell migration speed (**Figure 3.6A**) and reverted the Gleevec-treated cell morphology approximately back to control NBTII cells (**Figure 3.6B-3.6D**).
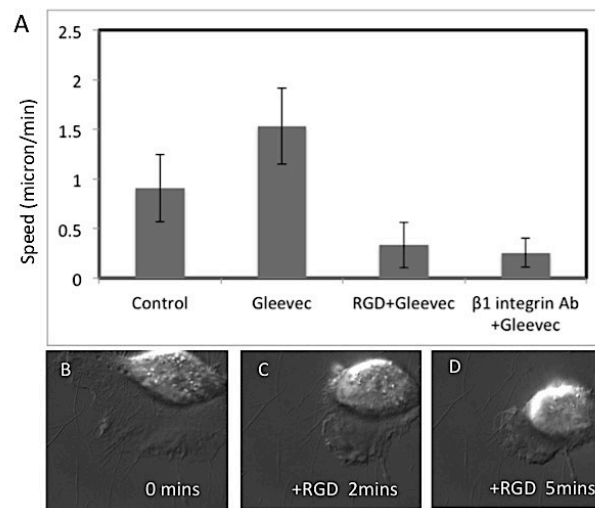

Figure 3.6. Blocking of integrin related adhesion dramatically inhibits the migration speed of Gleevec-treated NBT-II cells. A) Migration speed of Gleevec-treated cells incubated with either beta1-Integrin blocking antibody (1 μg/ml) or an RGD-containing peptide (100 μg/ml). Migration speed was measured 30 minutes after addition of beta1-Integrin blocking antibody or

RGD containing peptide (n>10 for each group). Panels B-D) are DIC images of an NBT-II cell treated with Gleevec (20 μM) migrating on a 10 μg/ml collagen-coated substrate, and then treated with 1 μg/ml RGD containing peptide. Images before addition of RGD containing, 2 minutes after and 5 minutes after addition of the RGD peptide are shown. Scale bars is 20 μm.

3.4.6. Gleevec induces changes in actin cytoskeleton, p-MLC localization and traction

The filamentous actin and active myosin were detected by fluorescent phalloidin and phosphorylated myosin light chain antibodies, respectively. The distribution of active myosin in control and Gleevec-treated NBTII cells differ markedly. In the case of the control cells, active myosin is localized around the cell nucleus, with little near the leading edge (**Figure 3.7A-C**). By contrast, active myosin predominantly localized near the trailing margin of the Gleevec-treated cells. Since the active myosin status is associated with cell contractility, we compared the traction distribution between the two groups utilizing an elastic substrate methodology (22, 41-45). **Figure 3.7G-H** show the color-coded magnitudes of the bead displacements mapping for control and Gleevec-treated cells, respectively. The white line drawn indicates the outline of the cell. The insets are the phase image of a control (**3.7G**) or a Gleevec-treated cell (**3.7H**). **Figure 3.7I-J** shows the calculated constrained traction map for control and Gleevec-treated cells with the insets showing magnified traction maps at the cell wing regions. Tractions are much higher in the wings of the Gleevec treated cells than control cells (**Figure 3.7J**) where immunofluorescence labeling by anti-p-MLC antibody indicates a concentrated region of active myosin proximate to the high traction regions (**Figure 3.7F**). The Gleevec-treated cells generated a remarkable almost four-fold greater total traction force than control NBTII cells (**Figure 3.7K**).
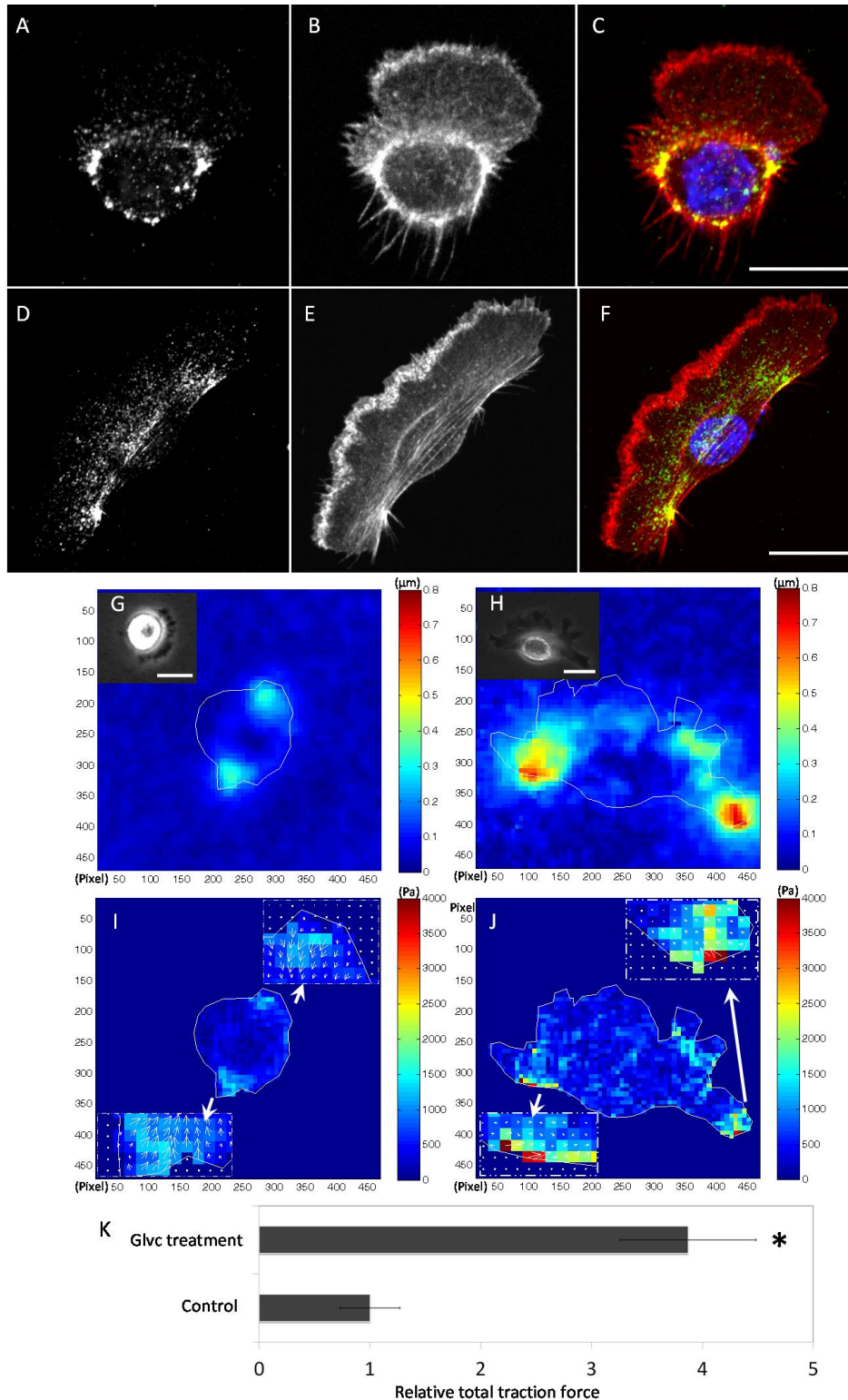
Figure 3.7. Changes in distribution of active myosin and traction forces after Gleevec treatment. Control NBT-II cells (A-C) or Gleevec-treated cells (D-F) that have been fixed, permeabilized and stained for phosphorylated myosin II light chain (p-MLC) to visualize active myosin localization (A and D) and Rhodamine-phalloidin to visualize the actin cytoskeleton (B

and E). (C and F) Overlay images indicate the colocalization of actin bundles and p-MLC (red). The nucleus of the cell is stained with DAPI (blue). Bar= 20 μm. (G to J) Elastic substrate traction mapping of a control NBT-II cell (G and I) and Gleevec-treated NBT-II cell (H-J). (G and H) are the bead displacement maps and (I and J) are the traction maps where color bars indicate relative values (see Methods). The inset images in G and H are the phase image of the control cell and the Gleevec-treated cell. The white lines in G and H are outline of each cell. The inset images of figure I and J are the tractions magnified from indicated cell wings. Panel K is a calculation of the total cell traction force generated by cells (Materials and Methods). The value is normalized to total traction forces from control cells. The bar graph indicates NBTII cells treated with Gleevec generate considerably more total traction force than control NBTII cells. Error bars are standard deviation. Bar= 20 μm. 8 cells were examined for each case.

3.4.7. Effects of RhoA family GTPases on D-shaped NBTII cell migration

The rapid response of NBTII cells to Gleevec suggests that the inhibition of the Abl-family kinases is altering active signaling pathways (8, 46) as opposed to affecting transcriptional regulation. Because of the importance of RhoA GTPase in cell shape and migration (47-49), we measured its activity before and after Gleevec treatment. Using a RhoA activity pull down assay, we found that RhoA activity significantly increased when Abl-family kinases were inhibited (**Figure 3.8A**). Cells treated with Gleevec for one hour have nearly doubled RhoA activity (**Figure 3.8B**).
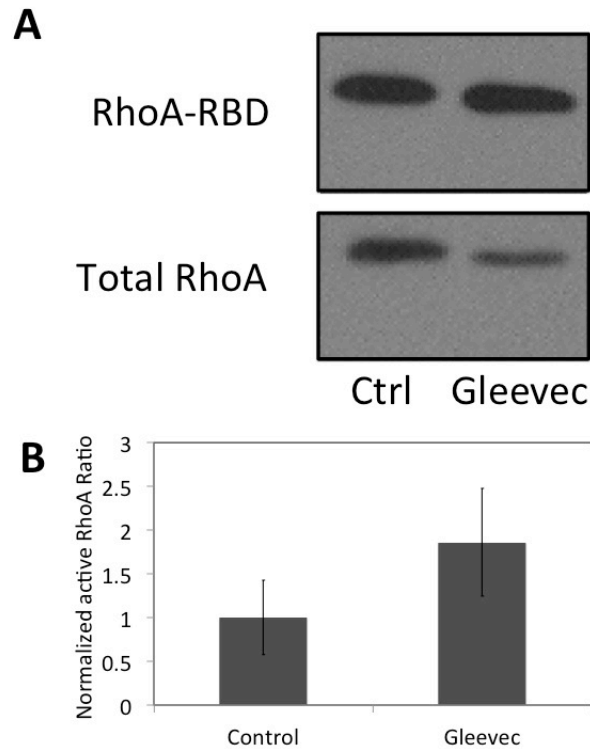
Figure 3.8. Abl-family kinase inhibition increases RhoA activity. A) A RhoGTPase pull-down assay before and after Gleevec treatment (20 μM). NBT-II cells were cultured on a 10 μg/ml collagen-coated substrate. B) A bar graph quantifying the results from the pull-down assay. (n=4 experiments).

Because of the significant increase in active RhoA in Gleevec-treated cells, we asked whether RhoA and its downstream effector ROCK were important in the Gleevec-induced phenotype by introducing the RhoA inhibitor (C3) and the Rho kinase inhibitor (Y27632) to NBTII cells previously treated with Gleevec (**Figure 3.9A-C,** respectively**)**. We found that adding either C3 (**Figure 3.9B**) or Y27632 (**Figure 3.9C**) to Gleevec-treated cells resulted in significantly increased numbers of retraction fibers and more rounded nuclei compared to cells treated with Gleevec only (**Figure 3.9A**). In addition, both of these reagents reduced migration speed (**Figure 3.9D**) and persistence (**Figure 3.9E**). The nuclear aspect ratio and total retraction fiber length were calculated and

compared to cells treated with Gleevec only or control cells (**Figure 3.9F-G**). C3 or Y27632 treated cells in the presence of Gleevec exhibit similar nuclear aspect ratios and retraction fiber parameters as the control group. In addition, the whole cell aspect and area ratios for the Gleevec + C3 treatment group or for the Gleevec + Y27632 group are comparable to the Gleevec only group (**Supplemental Figure 3.3A-B**). We also observed that while Gleevec + C3 or Gleevec + Y27632 treated cells produce extended lamellae, these lamellae often fragmented during migration. Because C3 and Y27632 in effect rescue the control phenotype, these results indicate that RhoA and its downstream effector ROCK are required for the Gleevec- induced NBTII cell phenotype.
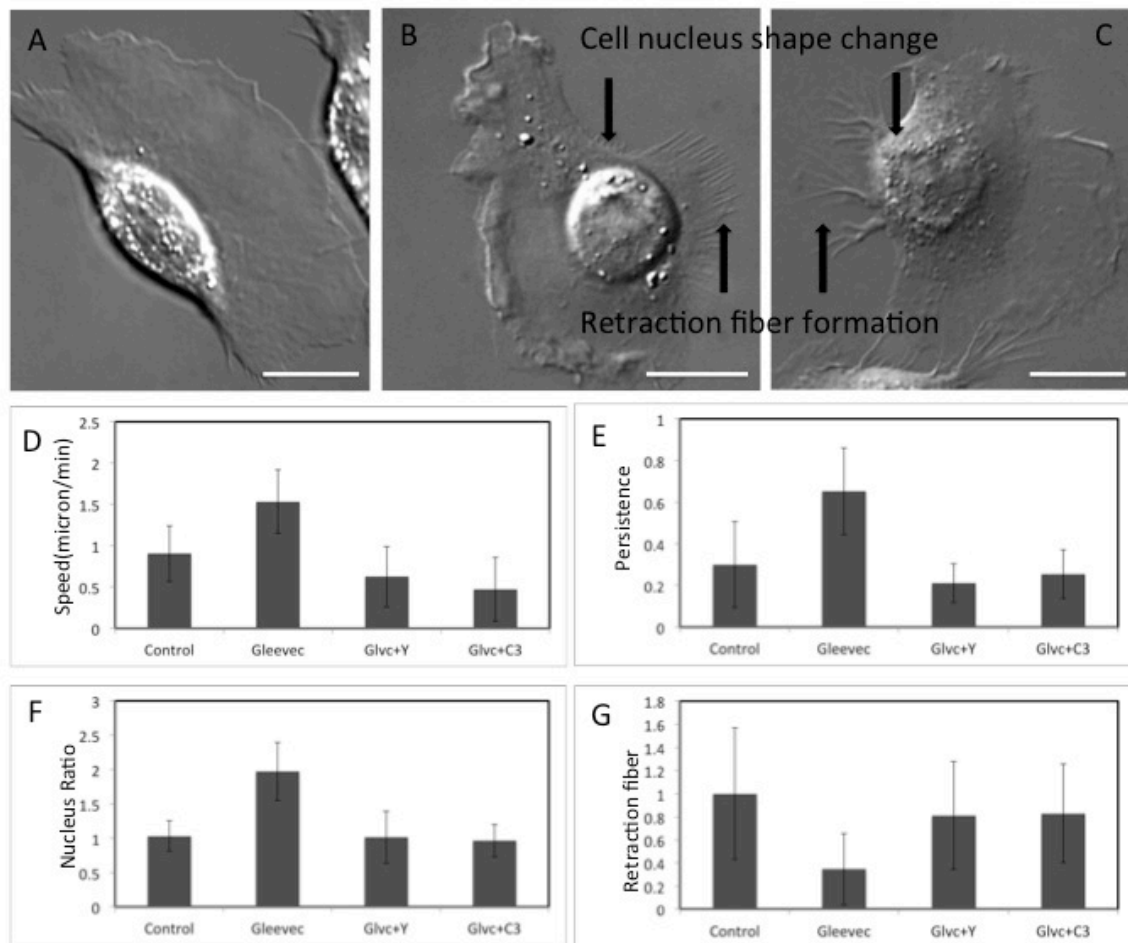
Figure 3.9. RhoA/ROCK activity is important for the Gleevec phenotype. A), B) and C) are DIC images of NBT-II cell migration status in the presence of 20uM Gleevec only, both 20uM Gleevec and ROCK inhibitor(5uM Y-27632), or both 20uM Gleevec and RhoA inhibitor (C3, 1ug/ml), respectively. These panels show that RhoA inhibition after Gleevec treatment increases the number of retraction fibers and produces more rounded nuclei. Scale bars are 20 μm. Panels D) to G) are cell migration speed, cell migration persistence, nuclear aspect ratio and cell retraction fiber ratio, respectively. In each figure, the four bars represent the control group, the 20uM Gleevec treated group, the 5uM Y-27632 + 20uM Gleevec treated group, and the 1ug/ml C3 + 20uM Gleevec treated group, respectively. Error bars indicate standard deviations. At least 15 cells were measured for each group.

3.5 DISCUSSION

Here, we show that inhibition of Abl family kinase activity with Gleevec produced a rapid and remarkable change in cell morphology and migration in which cells spread out a thin, extended lamella and migrated faster and with more persistence with some similarities to keratocyte migration (32, 34). In addition, this rapidly spreading, very thin lamella is similar to the rapid and extensive, "pancake" spreading of fibroblasts derived from Abl null mice (15). Associated with the Gleevec phenotype was an increase in RhoA activity, increased global cell adhesion strength, a pronounced change in adhesion patterns and an increase in total traction applied to the substrate.

3.5.1 Mechanism of the Gleevec-induced change in morphology and migration

Abl family kinases inhibit cell adhesion formation: Abl family kinases have been reported to be located at cell adhesions (7, 50). They are correctly positioned to regulate the reorganization of the cytoskeleton at sites of membrane protrusion and at focal adhesions where integrins are engaged. In 10T1/2 fibroblasts, during the initial 20-30 minutes of fibronectin stimulation, when c-Abl activity is the highest, the nuclear pool of c-Abl re-localizes transiently to focal adhesions (7, 50). This transient re-localization also occurs in NIH3T3 cells, where a fraction of the cellular Abl associates with the focal adhesion proteins, paxillin and Grb2 (51, 52). Abl family kinases have also been reported to reduce initial cell attachment to the substrate. On fibronectin, fibroblasts derived from Abl-null mouse embryos spread faster than their wild-type counterparts, while restoration of Abl expression in the Abl-null fibroblasts reduced the rate of spreading (15). Kain and

70

Klemke provided evidence that Abl family kinases negatively regulate cell migration by uncoupling CAS-Crk complexes (13). Li and Pendergast recently reported that Arg could disrupt CrkII-C3G complex formation to reduce β1-integrin related adhesion formation (17). These reports indicate that Abl family kinases negatively regulate cell adhesion, thus supporting our observations that Abl family kinase inhibition results in a more adhesive and motile phenotype.

RhoA involvement in the Gleevec-induced phenotype: Concomitant with the adhesion increase induced by Gleevec treatment, there is an increase RhoA activity. Since Bradley and Koleske reported that Abl family kinases could function through the activation of p190RhoGAP to reduce RhoA activity (53), it is possible that the Gleevec action occurs by inhibition of the Abl-mediated activation of this RhoGAP. In any event, the increase in RhoA activity correlates with the increase in total traction force applied to the substrate; the spatial disposition of active myosin II indicates contractile activity parallel to the long axis of the cell and enhanced traction in the wings of the treated cell. Moreover, ROCK inhibition abrogates the Gleevec phenotype suggesting the pathway Abl inhibition→increase in RhoA activity→increase in ROCK activity→increase in pMLC→increase in contractility and traction.

3.5.2 Changes in the adhesive behavior of the Gleevec treated NBTII cells

The D-shaped NBTII cells have a band of punctate dot-like adhesions in the vicinity of their leading edge that appear different from known adhesions in mesenchymal-type migrating cells. The area of these adhesions is quite small (~0.10 μm^2) compared to normal focal adhesions (~ 1μm^2), and their turnover as estimated from

observation of TIRFM movies is ~ 1 min, compared to >5 min for focal adhesions. These punctate adhesions are similar in size to nascent focal adhesions (54-56); but they rarely (<1%) matured to larger adhesions as many nascent adhesions do (56).

Our results taken as a whole indicate Abl family kinases play an important role in the regulation of cell adhesion and migration in that their inhibition produces a profound change in adhesions, morphology and cell migration. A fully integrated, quantitative view of inhibition of how these ubiquitous kinases produce these changes remains a challenge for the future.
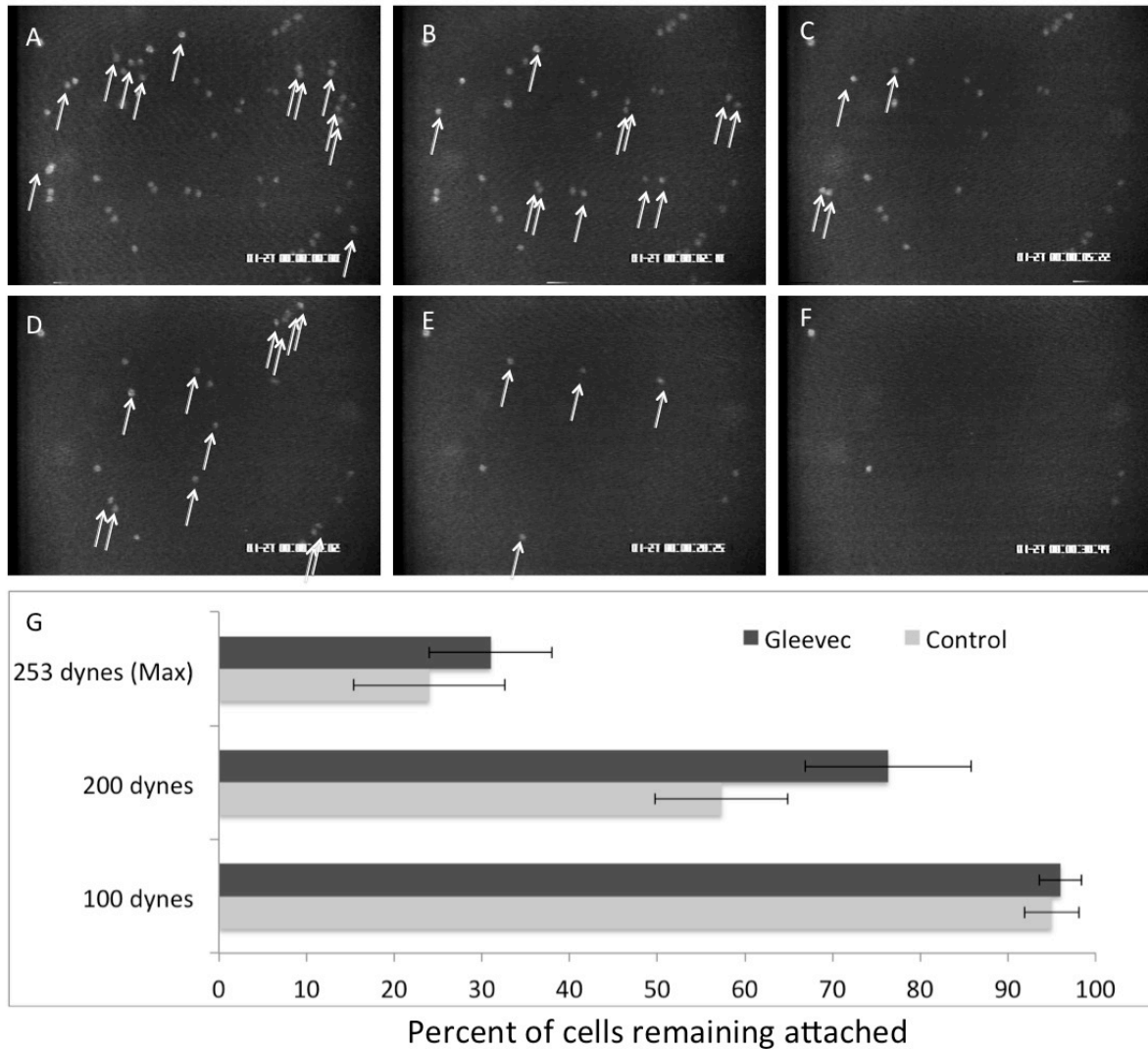
Supplemental Figure 3.1. Optimizing the laminar shear stress flow system for cell adhesion strength measurements.

Panel A to F shows the adherent NBTII cells under laminar shear stress flow system with a 253 dynes/cm^2 laminar force applied for 30 seconds. Cells are labeled with Cell Tracker Orange (Invitrogen). Images are same cells at different time points (before, 2s, 5s, 10s, 20s, 30s) which are indicated at bottom right of each images. Arrows in each image point out the cells detached by the shear stress as a function of time of shear stress application. G) Bar graph showing fraction of adherent cells retained after exposure to different laminar shear stresses for 1 min (N = 5 experiments; n = 11–20 images per N for 200 dynes/cm^2; N=1 experiment, n=3 images per N for 100 dynes/cm^2 and 253 dynes/cm^2 groups).
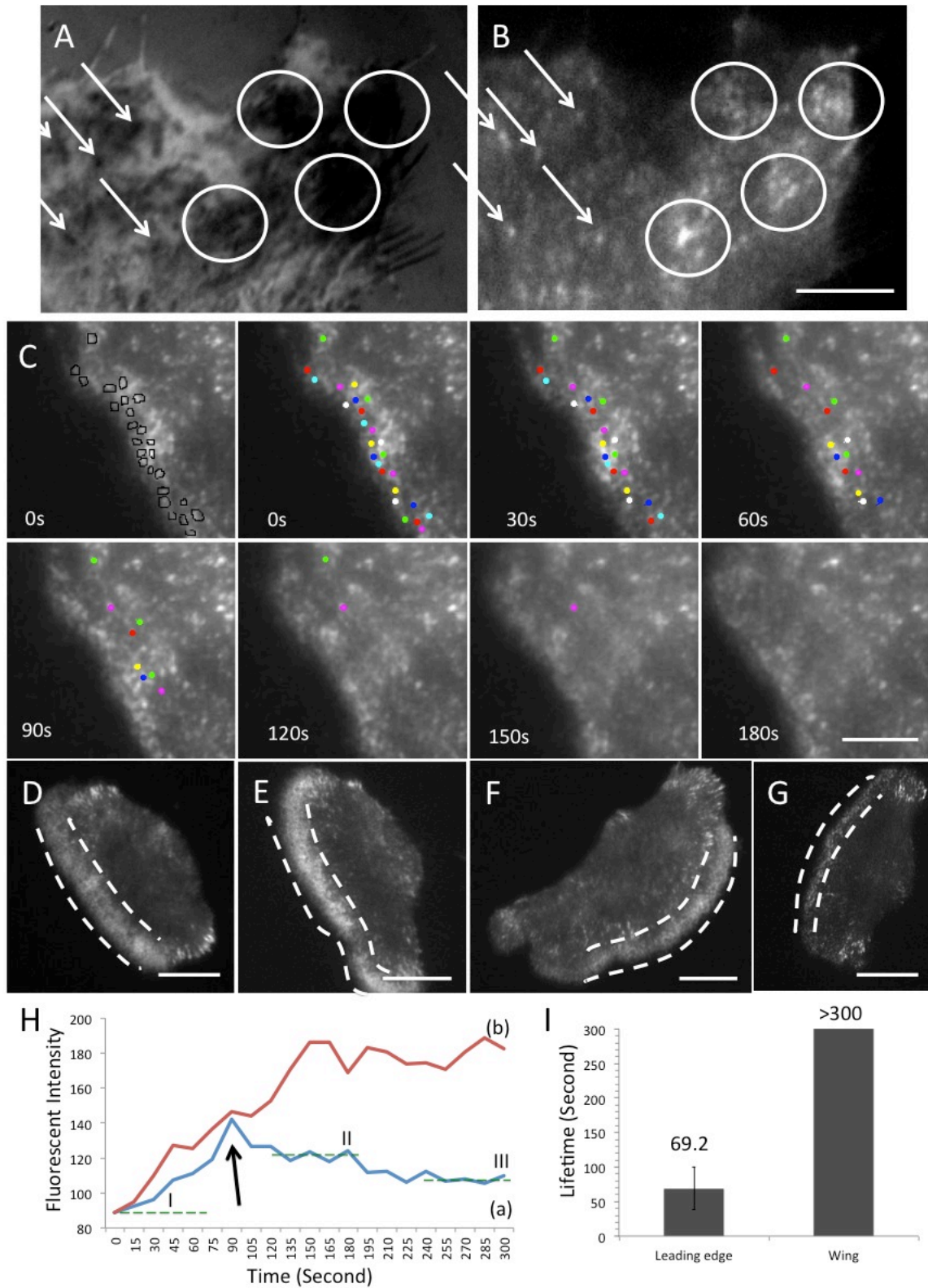
Supplemental Figure 3.2. Cell adhesions in Gleevec-treated NBTII cells

Panel A) and B) are IRM images and TIRFM images for the same region in a fixed NBT-II cells. The dark dots (marked by arrows) and dark regions (marked by circles) in the IRM image were

usually colocalized with the bright EGFP-Paxillin signal in TRIFM image, indicating these were cell-substrate adhesions. Panel C are the time-lapse images showing adhesion turnover at the leading edge of a Gleevec treated NBTII cells. To better illustrate adhesion turnover, punctate adhesions at cell leading edge (at time 0) were marked with black line and then labeled with colored dots correspondingly. Adhesions at time 0, and after 30, 60, 90, 120, 150 and 180 seconds were shown. Colored dots indicate the previous adhesion is still remaining at this time. Most of the adhesions disassembled after 120 seconds. Panel D to G are representative TIRFM images of EGFP-paxillin in Gleevec- treated NBTII cells, showing a rim of dense, punctate adhesions (adhesions in-between dotted lines) at the leading edge of the cells. Panel H is a temporal fluorescence intensity profile (see Materials and Methods) of EGFP-paxillin in a representative punctate adhesion at cell leading edge (a) or an adhesion at the side wings (b). Dotted lines I, II, III indicate the whole image fluorescent background, the cell leading edge fluorescent background, and the cell body fluorescent background respectively. The initial peak in the fluorescence intensity profile (marked by arrow) results from the formation of punctate adhesions. The lifetime is taken as time between liftoff from leading edge background (II) to when the intensity drops back to the cell body background (III). For the punctate adhesions at the leading edge the assembly and disassembly occurs quickly, with an average lifetime of ~70s (Panel I). By contrast, adhesions at the wings often gradually mature into strong and more stable adhesions with an average lifetime above 5mins (Panel I). Scale bars in panels B and C are 5 μm, and in D, E, F, G are 20 μm. Data are mean ± standard deviations measured from 6-10 individual adhesions in 5-7 cells from independent experiments.
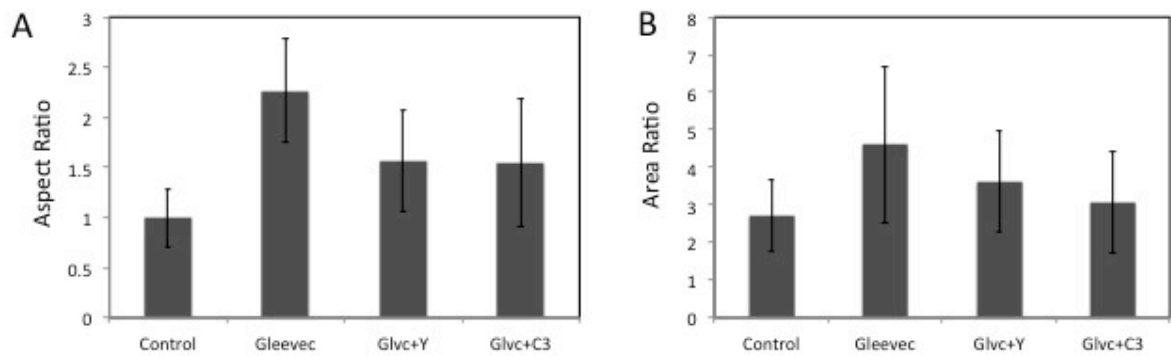
Supplemental Figure 3.3. RhoA/ROCK activity afffect cell morphology

Panel A) and B) are whole cell aspect ratio and cell area ratio. In each figure, four groups are control group, 20uM Gleevec treated group, 5uM Y-27632 + 20uM Gleevec treated group, and 1ug/ml C3 + 20uM Gleevec treated group, respectively. Error bars indicate standard deviations. At least 15 cells were measured for each group.

3.7 REFERENCES

1. Ridley AJ, Schwartz MA, Burridge K, Firtel RA, Ginsberg MH, Borisy G, Parsons JT, and Horwitz AR. (2003). Cell migration: integrating signals from front to back. *Science* 302(5651): p. 1704-1709

2. Webb DJ, Zhang H, and Horwitz AF. (2005). Cell migration: an overview. *Methods Mol Biol* 294: p. 3-11

3. Franz CM, Jones GE, and Ridley AJ. (2002). Cell migration in development and disease. *Dev Cell* 2(2): p. 153-8

4. Schwartzberg PL, Stall AM, Hardin JD, Bowdish KS, Humaran T, Boast S, Harbison ML, Robertson EJ, and Goff SP. (1991). Mice homozygous for the ablm1 mutation show poor viability and depletion of selected B and T cell populations. *Cell* 65(7): p. 1165-75

5. Li B, Boast S, de los Santos K, Schieren I, Quiroz M, Teitelbaum SL, Tondravi MM, and Goff SP. (2000). Mice deficient in Abl are osteoporotic and have defects in osteoblast maturation. *Nat Genet* 24(3): p. 304-8

6. Tybulewicz VL, Crawford CE, Jackson PK, Bronson RT, and Mulligan RC. (1991). Neonatal lethality and lymphopenia in mice with a homozygous disruption of the c-abl proto-oncogene. *Cell* 65(7): p. 1153-63

7. Zhu JY and Wang JYJ. (2004). Death by Abl: a matter of location. *Current Topics in Developmental Biology, Vol 59* 59: p. 165-+

8. Bradley WD and Koleske AJ. (2009). Regulation of cell migration and morphogenesis by Abl-family kinases: emerging mechanisms and physiological contexts. *J Cell Sci* 122(Pt 19): p. 3441-54

9. Woodring PJ, Hunter T, and Wang JY. (2003). Regulation of F-actin-dependent processes by the Abl family of tyrosine kinases. *J Cell Sci* 116(Pt 13): p. 2613-26

10. Stradal T, Courtney KD, Rottner K, Hahne P, Small JV, and Pendergast AM. (2001). The Abl interactor proteins localize to sites of actin polymerization at the tips of lamellipodia and filopodia. *Curr Biol* 11(11): p. 891-5

11. Woodring PJ, Meisenhelder J, Johnson SA, Zhou GL, Field J, Shah K, Bladt F, Pawson T, Niki M, Pandolfi PP, Wang JY, and Hunter T. (2004). c-Abl phosphorylates Dok1 to promote filopodia during cell spreading. *J Cell Biol* 165(4): p. 493-503

12. Radha V, Rajanna A, Mitra A, Rangaraj N, and Swarup G. (2007). C3G is required for c-Abl-induced filopodia and its overexpression promotes filopodia formation. *Exp Cell Res* 313(11): p. 2476-92

13.   Kain KH and Klemke RL. (2001). Inhibition of cell migration by Abl family tyrosine kinases through uncoupling of Crk-CAS complexes. *J Biol Chem* 276(19): p. 16185-92

14.   Jin H and Wang JY. (2007). Abl tyrosine kinase promotes dorsal ruffles but restrains lamellipodia extension during cell spreading on fibronectin. *Mol Biol Cell* 18(10): p. 4143-54

15.   Woodring PJ, Litwack ED, O'Leary DD, Lucero GR, Wang JY, and Hunter T. (2002). Modulation of the F-actin cytoskeleton by c-Abl tyrosine kinase in cell spreading and neurite extension. *J Cell Biol* 156(5): p. 879-92

16.   Peacock JG, Couch BA, and Koleske AJ. (2010). The Abl and Arg non-receptor tyrosine kinases regulate different zones of stress fiber, focal adhesion, and contractile network localization in spreading fibroblasts. *Cytoskeleton (Hoboken)* 67(10): p. 666-75

17.   Li R and Pendergast AM. (2011). Arg kinase regulates epithelial cell polarity by targeting beta1-integrin and small GTPase pathways. *Curr Biol* 21(18): p. 1534-42

18.   Guilluy C, Swaminathan V, Garcia-Mata R, O'Brien ET, Superfine R, and Burridge K. (2011). The Rho GEFs LARG and GEF-H1 regulate the mechanical response to force on integrins. *Nat Cell Biol* 13(6): p. 722-7

19.   Radice GP. (1980). Locomotion and cell-substratum contacts of Xenopus epidermal cells in vitro and in situ. *J Cell Sci* 44: p. 201-23

20.   Truskey GA and Proulx TL. (1993). Relationship between 3t3 Cell Spreading and the Strength of Adhesion on Glass and Silane Surfaces. *Biomaterials* 14(4): p. 243-254

21.   Chan BP, Reichert WM, and Truskey GA. (2004). Effect of streptavidin RGD mutant on the adhesion of endothelial cells. *Biotechnology Progress* 20(2): p. 566-575

22.   Damljanovic V, Lagerholm BC, and Jacobson K. (2005). Bulk and micropatterned conjugation of extracellular matrix proteins to characterized polyacrylamide substrates for cell mechanotransduction assays. *Biotechniques* 39(6): p. 847-851

23.   Berginski ME, Vitriol EA, Hahn KM, and Gomez SM. (2011). High-resolution quantification of focal adhesion spatiotemporal dynamics in living cells. *PLoS One* 6(7): p. e22025

24.   Webb DJ, Parsons JT, and Horwitz AF. (2002). Adhesion assembly, disassembly and turnover in migrating cells -- over and over and over again. *Nat Cell Biol* 4(4): p. E97-100

25.   Toyoshima K, Ito N, Hiasa Y, Kamamoto Y, and Makiura S. (1971). Tissue culture of urinary bladder tumor induced in a rat by N-butyl-N-(-4-hydroxybutyl)nitrosamine: establishment of cell line, Nara Bladder Tumor II. *J Natl Cancer Inst* 47(5): p. 979-85

26.   Tucker GC, Boyer B, Valles AM, and Thiery JP. (1991). Combined effects of extracellular matrix and growth factors on NBT-II rat bladder carcinoma cell dispersion. *J Cell Sci* 100 (Pt 2): p. 371-80

27.   Valles AM, Boyer B, Badet J, Tucker GC, Barritault D, and Thiery JP. (1990). Acidic fibroblast growth factor is a modulator of epithelial plasticity in a rat bladder carcinoma cell line. *Proc Natl Acad Sci U S A* 87(3): p. 1124-8

28.   Tucker GC, Boyer B, Gavrilovic J, Emonard H, and Thiery JP. (1990). Collagen-mediated dispersion of NBT-II rat bladder carcinoma cells. *Cancer Res* 50(1): p. 129-37

29.   Huang C, Rajfur Z, Borchers C, Schaller MD, and Jacobson K. (2003). JNK phosphorylates paxillin and regulates cell migration. *Nature* 424(6945): p. 219-23

30.   Druker BJ, Tamura S, Buchdunger E, Ohno S, Segal GM, Fanning S, Zimmermann J, and Lydon NB. (1996). Effects of a selective inhibitor of the Abl tyrosine kinase on the growth of Bcr-Abl positive cells. *Nat Med* 2(5): p. 561-6

31.   Schindler T, Bornmann W, Pellicena P, Miller WT, Clarkson B, and Kuriyan J. (2000). Structural mechanism for STI-571 inhibition of abelson tyrosine kinase. *Science* 289(5486): p. 1938-42

32.   Lee J, Ishihara A, Theriot JA, and Jacobson K. (1993). Principles of locomotion for simple-shaped cells. *Nature* 362(6416): p. 167-71

33.   Lee J and Jacobson K. (1997). The composition and dynamics of cell-substratum adhesions in locomoting fish keratocytes. *J Cell Sci* 110 (Pt 22): p. 2833-44

34.   Keren K, Pincus Z, Allen GM, Barnhart EL, Marriott G, Mogilner A, and Theriot JA. (2008). Mechanism of shape determination in motile cells. *Nature* 453(7194): p. 475-80

35.   Wu C, Asokan SB, Berginski ME, Haynes EM, Sharpless NE, Griffith JD, Gomez SM, and Bear JE. (2012). Arp2/3 is critical for lamellipodia and response to extracellular matrix cues but is dispensable for chemotaxis. *Cell* 148(5): p. 973-87

36.   Izzard CS and Lochner LR. (1976). Cell-to-substrate contacts in living fibroblasts: an interference reflexion study with an evaluation of the technique. *J Cell Sci* 21(1): p. 129-59

37. Dedhar S, Ruoslahti E, and Pierschbacher MD. (1987). A cell surface receptor complex for collagen type I recognizes the Arg-Gly-Asp sequence. *J Cell Biol* 104(3): p. 585-93

38. Gullberg D, Tingstrom A, Thuresson AC, Olsson L, Terracio L, Borg TK, and Rubin K. (1990). Beta 1 integrin-mediated collagen gel contraction is stimulated by PDGF. *Exp Cell Res* 186(2): p. 264-72

39. Jokinen J, Dadu E, Nykvist P, Kapyla J, White DJ, Ivaska J, Vehvilainen P, Reunanen H, Larjava H, Hakkinen L, and Heino J. (2004). Integrin-mediated cell adhesion to type I collagen fibrils. *J Biol Chem* 279(30): p. 31956-63

40. Krieger M SM, Matsudaira PT, Lodish HF, Darnell JE, Zipursky L, Kaiser C, Berk A, ed. *Molecular cell biology (fifth ed.)*. 5th ed. 2004, *New York: W.H. Freeman and CO.* .

41. Trepat X, Wasserman MR, Angelini TE, Millet E, Weitz DA, Butler JP, and Fredberg JJ. (2009). Physical forces during collective cell migration. *Nature Phys* 5: p. 426

42. Angelini TE, Hannezo E, Trepat X, Fredberg JJ, and Weitz DA. (2010). Cell migration driven by cooperative substrate deformation patterns. *Physical Review Letters* 104(16): p. 168104

43. Butler JP, Tolic-Norrelykke IM, Fabry B, and Fredberg JJ. (2002). Traction fields, moments, and strain energy that cells exert on their surroundings. *American Journal of Physiology-Cell Physiology* 282(3): p. C595-C605

44. Lee J, Leonard M, Oliver T, Ishihara A, and Jacobson K. (1994). Traction forces generated by locomoting keratocytes. *J Cell Biol* 127(6 Pt 2): p. 1957-64

45. Oliver T, Dembo M, and Jacobson K. (1999). Separation of propulsive and adhesive traction stresses in locomoting keratocytes. *The Journal of Cell Biology* 145(3): p. 589-604

46. Hubbard SR. (2002). Protein tyrosine kinases: autoregulation and small-molecule inhibition. *Curr Opin Struct Biol* 12(6): p. 735-41

47. Hall A. (1998). Rho GTPases and the actin cytoskeleton. *Science* 279(5350): p. 509-14

48. Sanz-Moreno V and Marshall CJ. (2009). Rho-GTPase signaling drives melanoma cell plasticity. *Cell Cycle* 8(10): p. 1484-7

49. Machacek M, Hodgson L, Welch C, Elliott H, Pertz O, Nalbant P, Abell A, Johnson GL, Hahn KM, and Danuser G. (2009). Coordination of Rho GTPase activities during cell protrusion. *Nature* 461(7260): p. 99-103

50. Lewis JM, Baskaran R, Taagepera S, Schwartz MA, and Wang JYJ. (1996). Integrin regulation of c-Abl tyrosine kinase activity and cytoplasmic-nuclear transport. *Proc Natl Acad Sci U S A* 93(26): p. 15174-15179

51. Lewis JM and Schwartz MA. (1998). Integrins regulate the association and phosphorylation of paxillin by c-Abl. *J Biol Chem* 273(23): p. 14225-30

52. Renshaw MW, Lewis JM, and Schwartz MA. (2000). The c-Abl tyrosine kinase contributes to the transient activation of MAP kinase in cells plated on fibronectin. *Oncogene* 19(28): p. 3216-9

53. Bradley WD, Hernandez SE, Settleman J, and Koleske AJ. (2006). Integrin signaling through Arg activates p190RhoGAP by promoting its binding to p120RasGAP and recruitment to the membrane. *Mol Biol Cell* 17(11): p. 4827-36

54. Beningo KA, Dembo M, Kaverina I, Small JV, and Wang YL. (2001). Nascent focal adhesions are responsible for the generation of strong propulsive forces in migrating fibroblasts. *J Cell Biol* 153(4): p. 881-8

55. Choi CK, Zareno J, Digman MA, Gratton E, and Horwitz AR. (2011). Cross-correlated fluctuation analysis reveals phosphorylation-regulated paxillin-FAK complexes in nascent adhesions. *Biophys J* 100(3): p. 583-92

56. Choi CK, Vicente-Manzanares M, Zareno J, Whitmore LA, Mogilner A, and Horwitz AR. (2008). Actin and alpha-actinin orchestrate the assembly and maturation of nascent adhesions in a myosin II motor-independent manner. *Nat Cell Biol* 10(9): p. 1039-50

CHAPTER 4

Mechanism of Chromophore Assisted Laser Inactivation Employing Fluorescent Proteins [1]

4.1 SUMMARY

Chromophore Assisted Laser Inactivation (CALI) is a technique that uses irradiation of chromophores proximate to a target protein to inactivate function. Previously, EGFP mediated CALI has been used to inactivate EGFP-fusion proteins in a spatio-temporally defined manner within cells but the mechanism of inactivation is unknown (1, 2). To help elucidate the mechanism of protein inactivation mediated by fluorescent protein CALI ([FP]-CALI), the activities of purified Glutathione-S-transferase-FP (GST-EXFP) fusions were measured after laser irradiation in vitro. Singlet oxygen and free radical quenchers as well as the removal of oxygen inhibited CALI, indicating the involvement of a reactive oxygen species (ROS). At higher concentrations of protein, turbidity after CALI increased significantly indicating cross-linking of proximate fusion proteins suggesting that damage of residues on the surface

the protein, distant from the active site, results in inactivation. Control experiments removed sample heating as a possible cause of these effects. Different FP mutants fused to GST vary in their CALI efficiency in the order EGFP>EYFP>ECFP, while a GST construct that binds FlAsH results in significantly higher CALI efficiency than any of the XFPs tested. It is likely that the hierarchy of XFP effectiveness reflects the balance between ROS that are trapped within the XFP structure and cause fluorophore and chromophore bleaching and those that escape to effect CALI of proximate proteins.

4.2 INTRODUCTION

CALI (Chromophore Assisted Laser Inactivation) is a technique that uses irradiation of chromophores proximate to a target molecule to inactivate functions of that molecule. Since the inactivating light can be limited to small regions within a single cell and the inactivation can be accomplished in less than 1 s, the technique offers an important spatially and temporally controlled loss-of-function tool in cell and developmental biology that complements genetic and other loss-of-function methods (3). CALI was introduced for cell biological purposes using the dye malachite green as a chromophore by Jay and co-workers (4-6). More recently, the technique has been extended to fluorophores including EGFP (enhanced green fluorescent protein) 1, FlAsH (Fluorescein-based Arsenical Hairpin binder) (7), ReAsH (Resorufin-based Arsenical Hairpin binder) (8), and SLF' (synthetic ligand for mutant FKBP12 that is conjugated to fluorescein) (9), all of which produced successful loss of function of the labeled targets. Work employing EGFP as a CALI reagent was based on earlier work (10) which showed, in vitro, that GFP could be used as a CALI fluorophore. GFP is not nearly as effective as fluorescein or malachite green (10) in producing damaging radicals but, if the fluorescent fusion protein faithfully represents the native protein, then the localization of the CALI effect is ensured. The fact that interesting phenotypes have been obtained by CALI raises the issue of photochemical mechanism.

In this study, we investigated the mechanism of EGFP-CALI, how the proximity of the fluorophore to the target affected CALI, how different, commonly used XFPs compared in CALI efficiency, and how these XFPs compared in effectiveness to CALI

85

employing FlAsH. Our studies were done in vitro using various GST-XFP fusion proteins.

4.3 MATERIALS & METHODS

4.3.1 Creation of Proteins

4.3.1.1 Creation of GST-EXFP fusion proteins

The expression plasmids for the GST fusion proteins were derived from the parent vector pGEX4T3 (GE Healthcare). pGEX-4T3 and pEXFP vectors were digested with the restriction enzymes Xho I and Not I (New England Biolabs). The XmaI - Not I restriction fragment of pEXFP (Clontech) containing the fluorescent protein gene was ligated into into Xma I – Not I digested pGEX4T3 using T4 Ligase (Invitrogen). The resulting GST-EXFP fusion proteins contain the poly peptide linker LVPRGSPNSRVPVAT harboring a thrombin cleavage site. Single pass primer extension DNA sequencing was performed by ACGT inc. using the GEX 5' and GEX 3' sequencing primers.

4.3.1.2 Creation of GST – Tetracysteine fusion protein

Iproof High-Fidelity DNA polymerase (Biorad) was used for all PCR reactions. The GST-tetra cysteine fusion (GST-TC) was created through PCR amplification of the 3' portion of the GST gene between the BstBI and NotI restriction sites in pGEX-4T3. The 3 ' mutagenic primer replaced Aspartate 232 and Serine 233 with the tetra cysteine

motif CysCysProGlyCysCys. The PCR product and the vector pGEX4T3 were sequentially digested with BstBI and Not I. The restriction digest products were purified by agarose gel electrophoresis, ligated, and transformed into E.coli XL 10 (Stratagene). Subsequent clones were screened by the absence of an XhoI restriction site that is removed upon mutagenesis. Clones without an Xho I restriction sites were sequenced (ACGT inc).

4.3.2 Protein Expression and Activity Measurement

4.3.2.1 Expression of GST-Fusion Proteins

Tryptone and yeast extract were purchased from Fisher Scientific. Plasmids harboring the GST fusion proteins were transformed into E. coli BL21 (Stratagene). Starter cultures of 50 ml LB media (10 g Tryptone, 5 g Yeast Extract and 10 g NaCl / l) containing 100 mg/l ampicillin were inoculated from single bacterial colony and incubated at 37 C and shaking at 250 RPM until the optical density at 600 nm reached 0.4 to 0.6. 10 ml of the starter culture was used to inoculate 2.8 l Fernbach flasks containing 500 ml 2xYT media (16 g tryptone, 10 g yeast extract, and 5 g NaCl / l) and 100 mg/ml ampicillin. Cells were grown at 37 C, 250 RPM to an O.D. of 0.8 to 1.0 and then induced by adding IPTG at a final concentration of 1 mM. The temperature was lowered to 30 C and the cells were grown an additional 12 – 14 hours shaking at 250 RPM. Cells were collected by centrifugation and stored at – 80 C until use.

4.3.2.2 Purification and Characterization of GST fusion proteins

Frozen bacterial cells were resuspended in 4 volumes (4 ml / gram wet cell paste) 50 mM Tris-HCl pH 7.4 300 mM NaCl containing 4 mg / ml lysozyme, 0.05 mg/ml DNase,0.05 mg/ml RNase (Sigma Aldrich) and COMplete EDTA free protease inhibitor cocktail (Roche) (1 tablet / 25 ml). Cells were stirred on ice 30 min followed by sonication for 30 seconds at 50 % duty cycle and 60% power (Branson Model 450 sonifier). Cells were then stirred an additional 30 min. Cell debris was removed by centrifugation at 10000 RPM for 30 min in a Beckman J2-21 centrifuge equipped with a JA-20 rotor. The supernatant was loaded onto a 3 ml GSTrap affinity column (GE Healthcare) equilibrated in 50 mM Tris HCl pH 7.4 300 mM NaCl and then washed with 9 ml of equilibration buffer. The pure GST fusion protein was eluted with buffer containing 10 mM reduced glutathione (GSH). Fractions containing an XFP (or GST activity in the case of GST-TC) were pooled and concentrated using an Amicon Ultra centrifugal concentrators with a 10000 MW cutoff. Excess GSH was removed from the samples by passing over a G25 column equilibrated in 0.1 M KPi pH 7.4. Protein samples were either used immediately or frozen in liquid nitrogen after the addition of glycerol at a final concentration of 20%. Frozen stocks were stored at – 80 C until use.

4.3.2.3 Enzyme Activity Measurement

Enzyme activity was measured using a well characterized GST catalyzed reaction of GSH and 1-chloro-2,4-dinitrobenzene (CDNB) whose product has an increased absorbance at 340 nm (11). A stock solution of CDNB was prepared in absolute ethanol at a final concentration of 40 mM and a 0.1 M GSH stock solution was prepared in 0.1 M

KPi pH 6.5. Reactions were carried out in 0.1 M potassium phosphate buffer, pH 6.5, 1 mM CDNB, 5 mM GSH. Kinetic traces were obtained by monitoring the absorbance increase at 340 nm. A background rate of reaction was recorded for 1 min prior to the addition of GST fusion protein. Reactions were initiated by the addition of an appropriate amount of the GST fusion protein and the pseudo first order rate was determined from the initial slope of the kinetic traces. The extent of fluorescent protein chromophore maturation was estimated by measuring protein concentration using the BCA protein assay (Pierce) and comparing these values to the values obtained from the published chromophore extinction coefficients (Clonetech).

4.3.3 Chromophore Assisted Laser Inactivation Setup

An unfocused continuous wave argon-ion laser (Stabilite 2017, Spectra-Physics, Mountain View, CA) was used to irradiate FP-GST at the following wavelengths: 488nm for EGFP and FlaSH, 514nm for EYFP, and 457.9 for ECFP. Laser power output was verified using a power meter (Coherent FieldMate with PM3Q head, Santa Clara, CA). The laser light was directed onto a chamber consisting of a Teflon plate into which a hole 10 mm deep and 5 mm in diameter had been milled (Figure S-1). This plate was placed on an x-y translation stage and the chamber was centered under the beam. In separate experiments, the temperature increase in the chamber during illumination was monitored at regular time intervals (1min) using a thermistor TA-29 (Warner Instruments, Hamden CT) connected to temperature controller TC-344B (Warner Instruments, Hamden CT).

Prior to irradiation, the GST activity of the sample was assayed as a baseline for CALI efficiency measurements. The UV-Vis absorbance spectrum, and the fluorescence intensity at the emission maximum of the FP GST enzyme activity were measured. After illumination for a determined amount of time, the GST activity, absorbance and fluorescence were again measured as described above to determine the amount of CALI as well as the extent of chromophore and fluorophore bleaching. Typical UV-vis absorbance spectra before and after CALI are shown in (Figure 1B insets). The amount of CALI as a percentage is defined as:

$$CALI = [1-(A_{illumin}/A_{control})] \times 100 \qquad\qquad Eqn.\ 1$$

where Aillumin denotes enzymatic activity of the illuminated sample and Acontrol is the enzymatic activity before illumination. To determine the possible temperature effect on the activity of GST-EGFP, a 100 μL sample of EGFP-GST was incubated for 5 minutes at temperatures ranging from 37 to 55 C and then assayed for GST activity and chromophore integrity.

Oxygen Depletion and Singlet Oxygen Quenchers: Oxygen was reduced in the GST samples by incubating with 2mM Na2S2O4 (Kodak, Cat. 1066513) solution in KPi buffer pH 7.4 for 10 minutes prior to irradiation. Oxygen was also reduced in the GST-FP samples by incubating with OxyFluor (Oxyrase, Inc, Mansfield, Ohio) and 10mM lactic acid in KPi (pH 7.4) for 30 minutes. A drop of mineral oil (~ 50 μl) was layered on top of the sample chamber to prevent oxygen exchange with the environment before and during

90

irradiation. The chamber was then flushed with Argon and sealed with a coverslip. The oxygen level in the buffer was measured using a calibrated Clark-type O2 mini-electrode (12). The sample was carefully removed to avoid the top layer of oil. The singlet oxygen quencher sodium azide (10mM, and 100 mM; Sigma), and GSH (10mM, 40mM, Fisher) were incubated with samples containing GST-XFP for 15 minutes prior to illumination.

4.4 RESULTS & DISCUSSION

4.4.1 Spatial selectivity of FP CALI

To assess the importance of the proximity of the fluorophore to the target protein, experiments were conducted in the presence and absence of thrombin which will specifically cleave the fusion in the linker region between GST and EGFP. Fig 4.1 A (left panel) shows pre and post irradiation kinetic traces for GST-EGFP (top) and a thrombin cleaved GST ::: EGFP (bottom). The CALI effect is evident only when the fusion protein remains intact thereby maintaining the EGFP and GST in close proximity. When the fusion protein is cleaved, EGFP is bleached but no inactivation occurs.
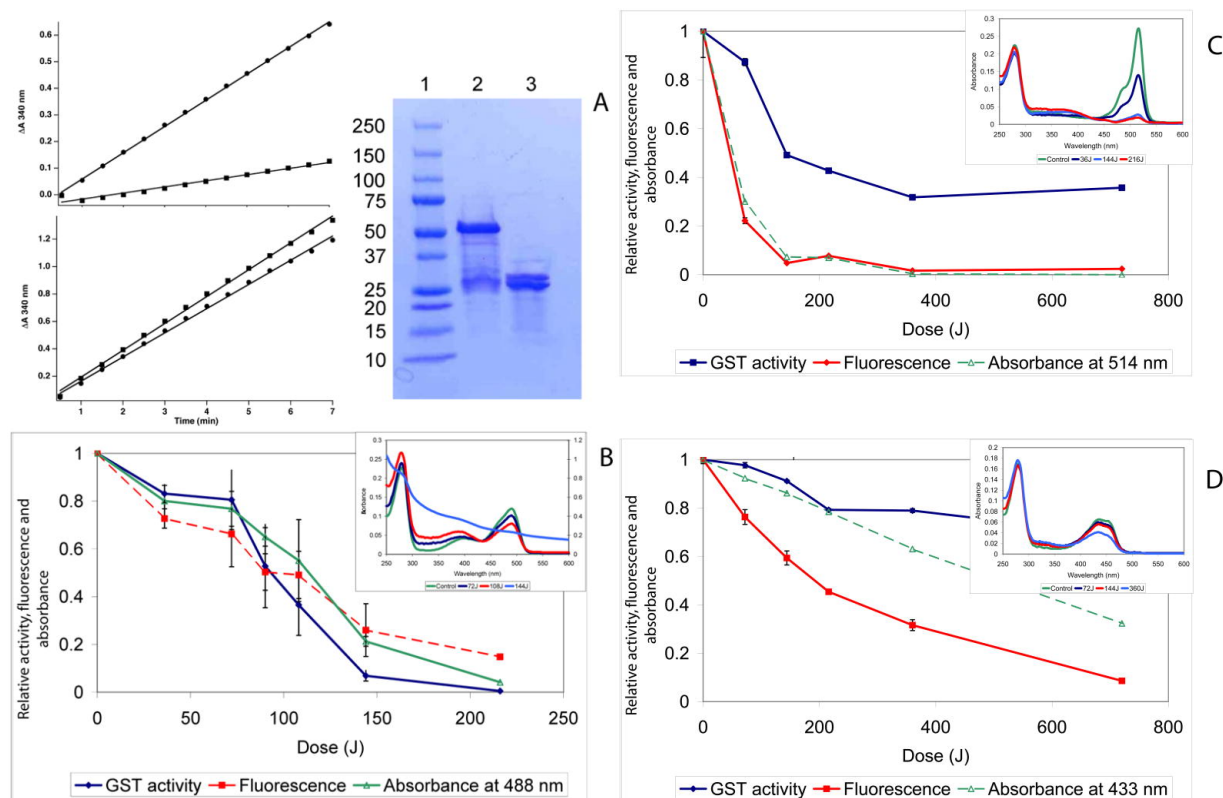
Figure 4.1. The CALI effect and fluorophore and chromophore photobleaching depend on the illumination dose.

(A) Kinetic traces of CDNB turnover. Top Left: GST-EGFP Before irradiation (circles) and after irradiation (squares). Bottom Left: GST-EGFP + 0.1U thrombin, before irradiation (circles) after irradiation (squares). Right SDS PAGE: Lane 1. Standards 2: GST-EGFP 3: GST:EGFP + 0.1 U Thrombin. (B, C &D) Relative activity (diamonds), fluorescence (rectangles) and peak absorbance (open triangles) remaining after irradiation decrease with increasing irradiation dose (obtained by increasing time at constant laser power) for purified XFP-GST. (B) ~ 25μM concentrations of EGFP-GST illuminated with 1200 mW at 488 nm. (C) a 27.5 μM concentration of EYFP-GST illuminated with 1200 mW at 514 nm. (D) a 29.1 μM concentration of ECFP-GST illuminated with 400 mW at 457.9 nm. Data points were collected in two (ECFP and EYFP) or three (EGFP) separate experiments and every point is the result of triplicate determinations. Error bars are standard deviations of such measurements. (In the case of EYFP and ECFP, determinations on the same day yielded error bars within the dimension of points on the graph.) All measurements (activity, blue; fluorescence, red and absorbance, green) were normalized to the initial values of non-illuminated sample to give relative values on the ordinate.

4.4.2 CALI dose-response characteristics for XFP-GST

Figure 4.1 B, C, and D show that bleaching and inactivation depends on the illumination dose (intensity [irradiance] X time) for GST-EXFP fusions. The insets show representative absorption spectra at various exciting light doses and show that only the chromophore bleaches leaving UV absorption of the fusion protein intact. Comparison of the results for GST-EGFP, GST- EYFP and GST- ECFP are instructive and yields some unexpected observations. The dependence on light dose for fluorophore and chromophore bleaching is different for each XFP. For EGFP and EYFP fusions, the fluorophore and chromophore bleaching exhibit similar dependencies on dose suggesting they are closely related processes. For EYFP-GST, the dependence on dose is almost exactly similar for fluorophore and chromophore bleaching and both bleaching processes show perfect reciprocity between excitation flux and time of excitation (Figure S4.2). However, the ECFP chromophore is considerably more resistant to bleaching while the bleaching of the fluorescence occurs at lower illumination doses (compare Figure 4.1D to 4.1B and 4.1C).

The relationship between bleaching and CALI also depends on the XFP employed. First, when the chromophore is bleached, CALI is no longer effective as expected. In the case of EGFP-GST CALI, chromophore and fluorophore bleaching are parallel processes (Figure 4.1B), all tending towards completion, suggesting a common intermediate, most likely singlet oxygen (see below). By contrast, CALI of ECFP-GST and EYFP-GST is not complete and plateaus to non-zero values of inhibition as a function of dose (Figure 4.1C,D). The magnitude of this effect depends on the laser

power employed. When similar doses of illumination to EGFP-GST are delivered with 600 mW of power but for longer durations, CALI is similarly not complete; compare Figure S4.3A (the same as Figure 4.1B for convenience) and S4.3B. One possibility for apparent protection of the enzyme at high light doses is that in the case of EYFP and ECFP, the chromophore is much more sensitive to the ROS produced during irradiation; thus, bleaching occurs before a significant amount of ROS can escape the β-barrel, thereby lowering the efficiency of inactivation. Another possibility is that a fraction of these fusions is protected from CALI, presumably by structural factors inherent in the fusion protein.

For EXFP fusions to be effective CALI reagents the inactivation needs to be specific and act on the target of interest in the presence of other cellular proteins. In Figure S4.4, we show that similar characteristics for CALI are obtained when EGFP-GST is irradiated in bacterial cell lysates. This is important because such lysates will be a more realistic approximation to CALI in the protein rich cytosol of cells.

It was initially surprising that the CALI effect exhibited a strong dependence on the concentration of the XFP-GST tested. This dependence is shown for EGFP-GST, EYFP-GST and for ECFP-GST in Figure 4.2. This suggests that protein concentration dependent factors such as light-induced oligomerization or micro-aggregation play an important role in the mechanism of inactivation. This can be clearly seen in the absorption spectra of EGFP-GST in Figure 1B. At high dose, the spectra is typical of that dominated by light scattering and the samples become visibly turbid. To compare the

relative CALI efficiencies of the XFPs and FlAsH, we employed concentrations in which

aggregation was limited. These results are summarized in Table 4.1 and are normalized

to the number of photons absorbed. The study shows that the order of CALI

effectiveness per absorbed photon is FlAsH>EGFP>EYFP>ECFP.

TABLE 4.1

Table I. Relative CALI efficiencies of purified FP-GST variants and FlAsH-labeled GST

Probe	λexc (nm)	Dose (Joules)	CALI inactivation (%)	Relative CALI efficiency	Relative CALI efficiency per absorbed
EGFP	488	144	94	1	1
ECFP	457.9	144	9	0.1	0.27
EYFP	514	144	51	0.5	0.34
FlAsH	488	36	80	6.6	2.43

Data in column 4 are averaged experimental values as defined by Eqn 1. Values in column 5 were obtained by defining EGFP % CALI as 1 and correcting for dose. Final numbers in column 6 were obtained by correcting the values in column 5 by a factor that reflects the product of the difference in the number of photons for an excitation dose at a given wavelength (e.g. there are more photons in a 144J dose at 488 nm than at 457.9 nm by a factor of 1.07) and the difference in the extinction coefficient for each CALI reagent at the excitation wavelength.
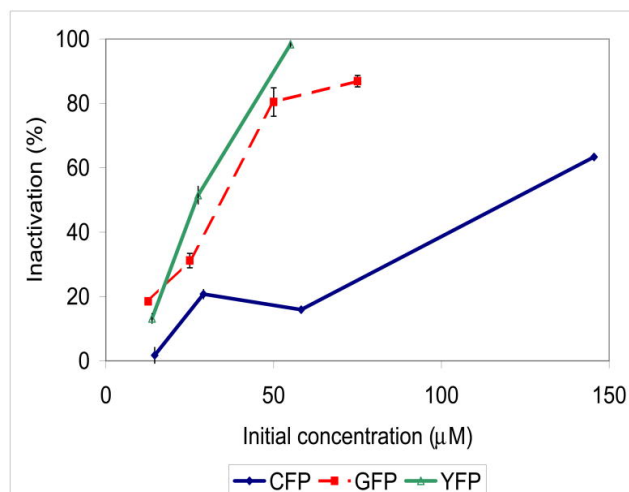
Figure 4.2. CALI effect of FP-GST depends on the concentration of illuminated sample.
EGFP-GST (rectangles, 90J dose) and YFP-GST (open triangles, 144J dose) show similar dependency of CALI effect on illuminated sample concentration while CFP-GST (diamonds, 216J dose), require much higher concentrations of the sample to show similar CALI effect. Inactivation is defined in Equation 1. Error bars are standard deviations of triplicate determinations at each concentration.

4.4.3 Mechanism of EGFP-CALI

4.4.3.1 CALI depends on oxygen and ROS:

The FP-CALI and FlaSH-CALI process depends on both light and oxygen. Figure 3A shows a summary of the effects of adding ROS scavengers. We employed the oxygen scavenger, Na2S2O4, to demonstrate that oxygen is required for the CALI process; we also removed oxygen using Oxy-Flour with similar effect. It is likely that the predominant ROS is singlet oxygen as shown by the efficient quenching of CALI by NaN3, which increases going from 10 mM to 100 mM NaN3. In addition the general ROS trap, glutathione which is also present in the cytoplasm abrogates the CALI process. Interestingly, NaN3 had little effect on absorbance (Figure 4.3B) and fluorescence photobleaching of EGFP (data not shown). However, it is clear that CALI of EGFP-GST

was inhibited because the light scattering signature is lost from the spectrum in the presence of NaN3. (The absorbance increase in the spectral region below 280 nm is due to specific absorption of NaN3 and not a light scattering effect as determined by absorbance measurements of pure NaN3 in solution (data not shown)). This effect may be explained by the accessibility of the chromophore to the inhibitor. Upon irradiation and interaction with molecular oxygen, the chromophore is exposed to a locally high concentration of ROS; unless the inhibitor can diffuse freely through the structure of the protein, inhibition of bleaching is apparently less efficient. This also strongly suggests that it is the ROS that escape the β-barrel structure that cause the CALI effect and it is these species that can be quenched by azide. Similar, though not identical, inhibition effects are seen for EYFP- and ECFP-GST CALI experiments (Figure S4.5).

4.4.3.2 CALI is accompanied by cross-linking and breakdown

SDS PAGE was employed at the end of the experiment to assess the integrity of the EGFP-GST as shown in Figure 4.3B (inset) after maximum dose. The gel reveals evidence of small amounts of both higher and lower MW components. The former suggests ROS induced cross-linking (13) while the latter band at ~ 25KDa reveals a photoinduced cleavage, possibly between EGFP and GST.
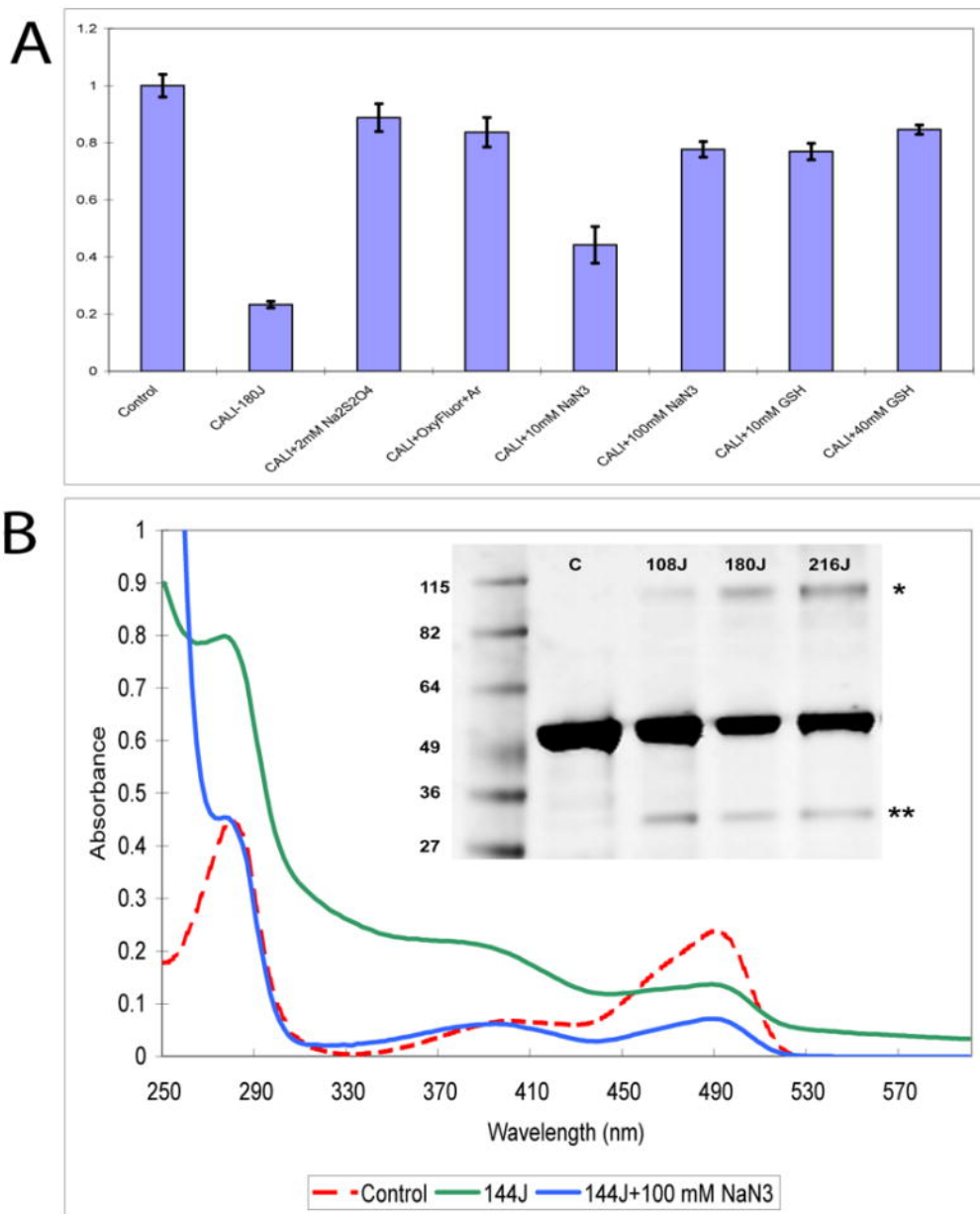
Figure 4.3. Effect of inhibitors on the CALI effect and chromophore bleaching

(A) EGFP-GST CALI effect depends on the presence of oxygen. GST activity diminishes after illumination with 180J dose (middle bar) but removal of oxygen from solution by addition of 2.5 mM of sodium dithionate (Na2SO4) or OxyFluor prevents inactivation of GST by light. Addition of 10 mM and 100 mM of sodium azide (NaN3) partially decreases the inactivation of EGFP-GST after illumination with 180 J dose of light and its effect increases with the concentration implicating singlet oxygen in CALI inactivation of EGFP-GST. When introduced into solution at 10 mM and 40 mM (not shown) concentrations, GSH—a general ROS inhibitor, commonly present in cells, almost fully protects the enzymatic activity of EGFP-GST against CALI. (B) Absorbance spectra of EGFP-GST show formation of crosslinked photoproducts after

98

illumination with 144J dose of light (green line, compare to control, red line). Addition of 100mM NaN3 prevents the formation of such aggregates but it does not prevents the chromophore photobleaching. This indicates that ROS are responsible for formation of crosslinked aggregates. Inset: SDS PAGE analysis of EGFP-GST after illumination with different doses of light. Main band, centered around 53 kD, represents EGFP-GST construct. High molecular weight (>100 kD) bands with increased amount of protein show after illumination of the sample with increasing doses of laser light. These bands are probably crosslinked photoproduct. Minor amounts of degradation (presumably, photocleavage) indicated by lower molecular weight bands (~ 30 kD).

4.4.3.3 CALI is not due to thermal effects

The temperature increase at the end of a given irradiation was monitored and a substantial temperature increase (to~ 45 C) occurred due to the absorption of XFP but no appreciable increase was recorded in buffer alone. This is shown in Figure S4.6A. However, the GST part of the fusion protein remains enzymatically active when incubated at temperatures up to 50 C for 5 min (Figure S4.6B), which is similar to the heating observed during irradiation. During this same incubation, the fluorophore and chromophore were similarly stable (Figure S4.6B). Above 50 C, enzyme activity dropped rapidly presumably due the thermal denaturation of the GST but molecular integrity of the fusion was retained as shown by SDS-PAGE analysis (Figure S4.6C) as would be expected. GST-ECFP and GST-EYP were also tested and remained stable at temperatures <50 C (data not shown). Therefore, we conclude that the inhibition of CALI activity is due to light-mediated damage and is not due to thermal effects.

4.5 DISCUSSION

Overall, we have shown that the XFP-CALI effect involves light and oxygen. Bleaching and CALI follow parallel courses for GST-EGFP but not in the case of GST-ECFP or GST-EYFP where some of the fusion protein is effectively protected against CALI at higher irradiation doses (Figure 4.1). Post CALI SDS gels followed show that EGFP-GST remains largely intact after irradiation (Figure 4.3B, inset), although a small amount of aggregation and cleavage occurs. At higher concentrations of protein, crosslinking and aggregation, as evidenced by the spectra in Figure 3B as well as the dependence of inactivation on protein concentration, presumably play a role in the mechanism of inactivation. Indeed, our results conform to general patterns of singlet oxygen damage inflicted on proteins: breakage of the protein backbone is relatively unlikely but aggregation via singlet oxygen mediated cross-linking is a common damage mode (13-15).

The effectiveness of an XFP as a CALI reagent appears to involve a complex interplay of various factors as depicted in Figure 4.4. First, there are factors intrinsic to the XFP itself including the type of chromophore, its maturation and its stability. Next, one needs to consider the particular fusion, the inactivating light dose and the presence of molecular oxygen. Finally, mechanistic factors will be important: the spatial disposition of the chromophore and the target protein (some orientations may not favor inactivation mediated by ROS), the relative amounts of ROS released from the XFP vs. ROS trapped inside the XFP which will cause bleaching, and, the propensity for intramolecular as

100

contrasted to cross-linking damage inflicted on the target protein. In general, the mechanism of fluorescent protein CALI will be multifactorial so that, at this juncture, case by case empirical studies will be required before rational design principles can be developed.

Factors Influencing the Effectiveness of CALI

FUSION PROTEIN
- XFP type
- Maturation of chromophore
- XFP stability

CALI CONDITIONS
- Dose (laser power + time)
- [XFP-fusion]
- Presence of O_2

MECHANISMS OF CALI
- Spatial disposition of chromophore + target protein
- Issue of CALI + Bleaching: ROS escape from barrel vs. bleaching
- Intra molecular CALI vs. surface modifications and cross-linking of proximate proteins
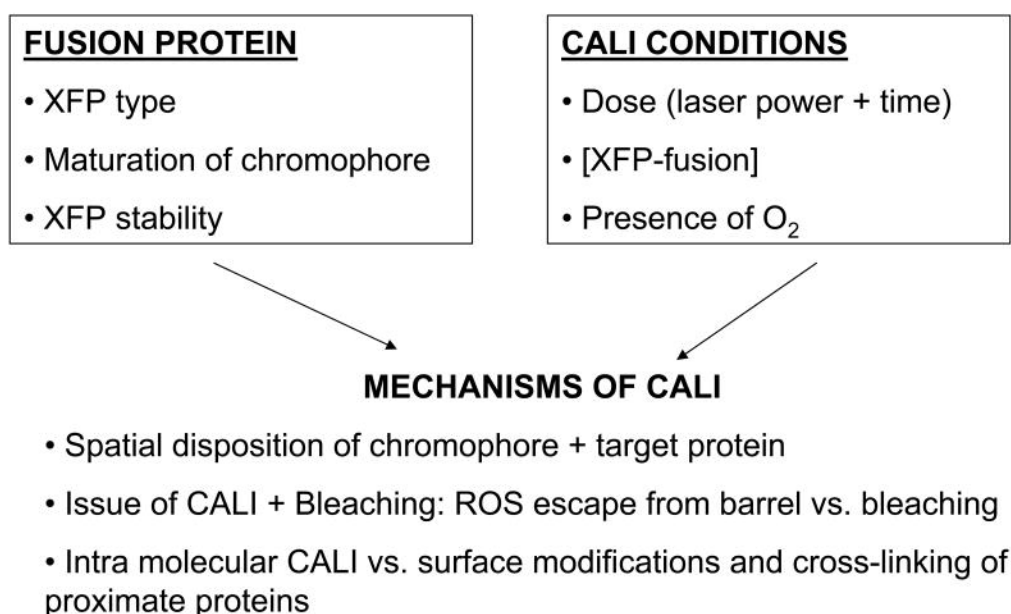
Figure 4.4 Factors influencing the effectiveness of XFP-CALI

It is likely that both the photobleaching and the CALI effect proceed from the triplet state obtained via intersystem crossing after excitation (see, for example, 3). However the quantum yields for photobleaching and CALI are much smaller than that for emission. Thus when a pulse of light is absorbed by the chromophore, a large burst of emitted photons accompanies the absorption as well as a much smaller burst of ROS, albeit with time delays. It is likely that the major ROS produced by light interaction with

101

EGFP, at least, will be singlet oxygen (3, 16, 17). If the photoproducts escape the XFP, they will form a cloud whose dimension is defined by the excitation intensity, the mobility of the ROS and the density of reactive sites proximate to the ROS generator. We suppose that the effectiveness of CALI will depend on the ratio of escaped ROS to those trapped in the barrel where they can bleach the fluorophore and chromophore; bleaching the chromophore will effectively terminate CALI. Xanthene-based dyes would be expected to be more effective CALI reagents since they have a higher intrinsic quantum yield for the production of ROS and the ROS produced have little structural impediment to reaching reactive amino acid residues. Thus, the increased effectiveness of FlAsH as compared to the XFPs (Table 4.1) could be expected. Indeed, the first studies done on the effectiveness of GFP for CALI in vitro were done by Surrey et al. (10) who showed that the irradiation dose for a given inactivation of β-galactosidase was roughly 6000X and 70X higher than that required for fluorescein and malachite green tagged antibodies, respectively. Rajfur et al performed the first EGFP-CALI studies in cells (1) and showed that when EGFP-alpha-actinin was locally inactivated, detachment of the actin filaments linked to integrins through alpha-actinin occurred. The local irradiation dose was estimated to be approximately 200X that used for ReAsH studies (105 kJ/cm^2) (8).

The order of CALI effectiveness is FlAsH>EGFP>EYFP>ECFP normalized to equal number of photons absorbed, with FlAsH being considerably more effective. Being a good sensitizer is a double-edged sword, however, because it generally means that the probes are quite bleachable. This hampers localization by fluorescence imaging and

means that CALI is being effected while the target protein is being localized in the image. In this respect, some XFPs, such as EGFP, will have an advantage in that the CALI regime is separated from the imaging regime in terms of the irradiation dose required for each operation.

We have discussed desirable characteristics for a CALI chromophore elsewhere (3) and several improvements could be anticipated. First, for the XFPs, high throughput screens (18) can be designed to screen many FP mutants for an optimal compromise between CALI and facile imaging. Second small, highly specific, dyes may be designed to bear both a CALI chromophore and a spectrally distinct fluorophore for imaging the location of the target protein without excessive bleaching. Recently, an optimization of CALI chromophores was accomplished based on the Halo reagent (19).
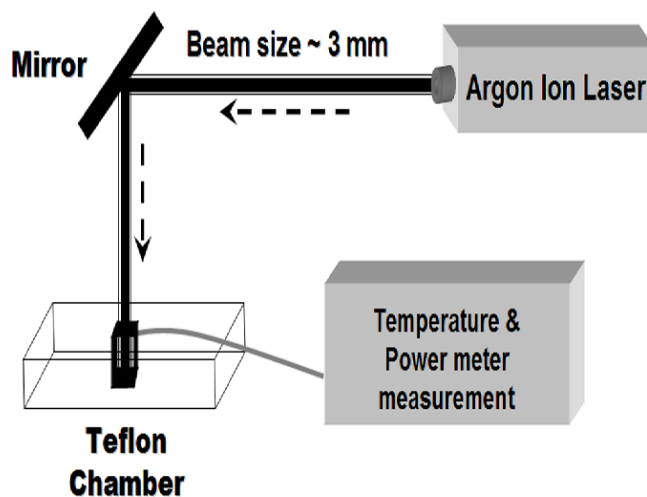
Figure S4.1 Experimental setup

Schematic showing the experimental setup for in vitro EGFP-CALI. An unfocused beam from a continuous wave (cw) Argon ion laser is reflected off a mirror into a single well of a Teflon chamber containing FP-GST sample. Each individual well of the sample chamber has 5 mm diameter, close to the laser beam diameter (3 mm) to insure irradiation of the entire sample volume (100 μl).
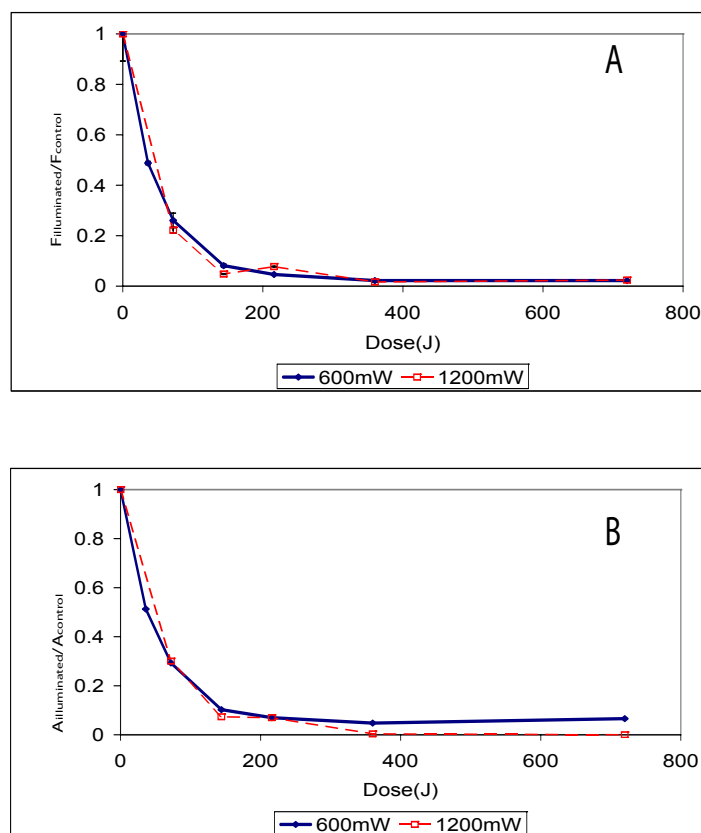
Figure S4.2 Reciprocity in flux and time of irradiation for EYFP-GST.
EYFP fluorescence (A) and chromophore (B) photobleaching depends on the illumination dose only, with laser beam power and time of illumination being reciprocal (1200 mW and 600mW at 514 nm). The results are presented as a ratio of sample fluorescence signal after illumination ($F_{illuminated}$) and before illumination ($F_{control}$). Correspondingly, chromophore photobleaching is measured as ratio of sample absorbance at 514 nm after illumination ($A_{illuminated}$) and before illumination ($A_{control}$).
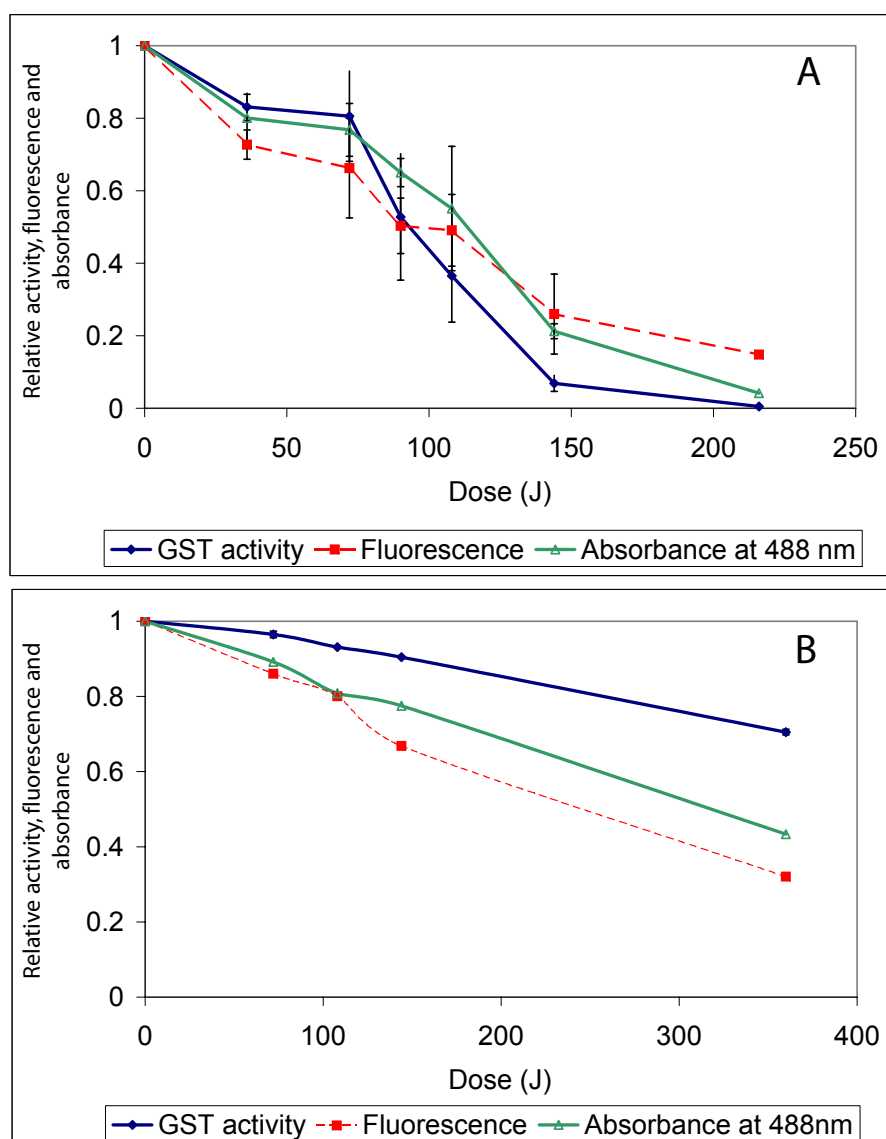
Figure S4.3 CALI depends on the power that is used to deliver a given dose.
Both the CALI and fluorophore and chromophore photobleaching is more pronounced at similar doses when GST-EGFP is illuminated with 1200 mW (A) than with 600 mW (B) at 488 nm laser power. Figure S-3A is reproduced from text figure 1B for reader convenience. All measurements (activity, blue; fluorescence, red and absorbance, green) were normalized to the initial values of non-illuminated sample to give relative values on the ordinate.
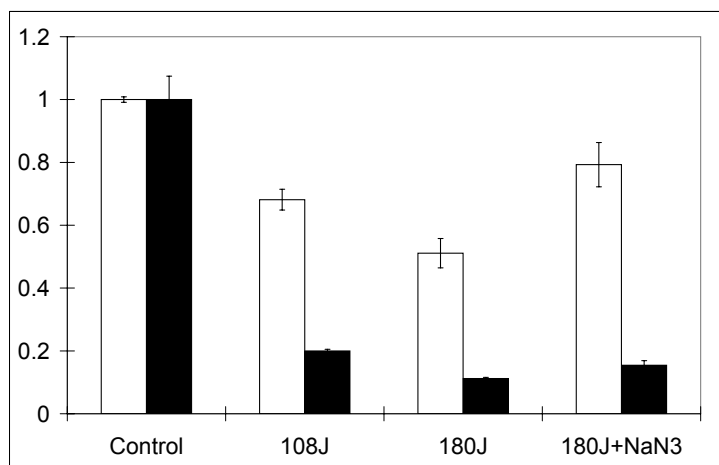
Figure S4.4 CALI of EGFP-GST in bacterial cell lysates.

GST-EGFP activity (open bars) and EGFP fluorescence (full bars) decrease with increasing illumination dose, showing the same trend as purified protein. The presence of NaN3 diminishes CALI effect while the decrease in fluorescence remains comparable to that without NaN3. Concentration of GST-EGFP in lysate is estimated to be ~ 12μM based on enzyme activity. All measurements (activity, open bars) and fluorescence (filled bars) were normalized to the initial values of non-illuminated sample (control) to give relative values on the ordinate.
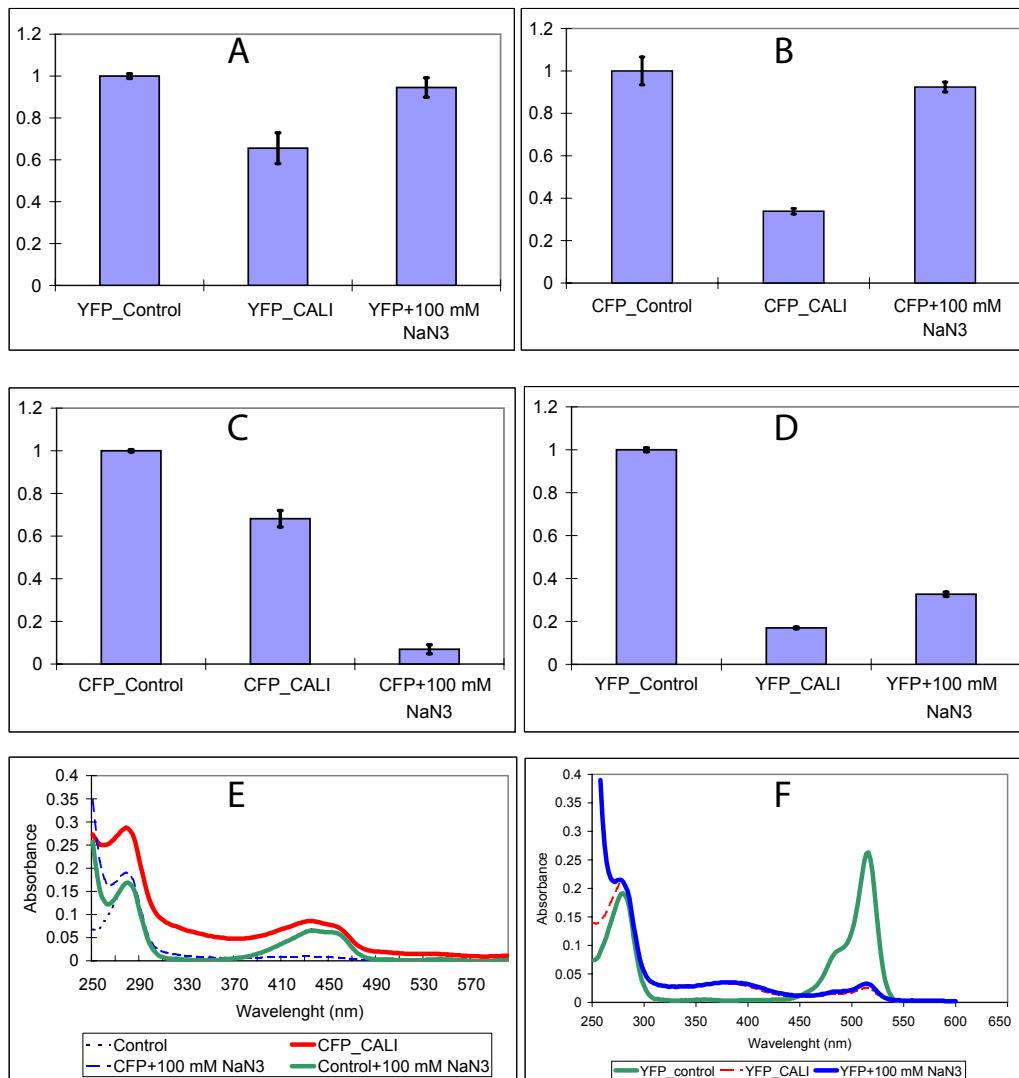
Figure S4.5 Effect of singlet oxygen quencher sodium azide on ECFP & EYFP-mediated CALI.

A and B: Enzymatic activity of GST–EYFP decreases after 144J dose illumination with 514 nm laser light. Enzymatic activity of GST-EYFP is protected from CALI inactivation in the presence of 100mM NaN3 (panel A). A similar effect is observed for GST-ECFP (216J of 457.9nm laser light) (panel B). C and D: Fluorophore bleaching in the presence and absence of sodium azide for GST- ECFP and GST-EYFP, respectively. For A-D, all measurements were normalized to the initial values of non-illuminated sample (control) to give relative values on the ordinate. E and F: Absorbance spectra of GST-ECFP (panel E) and GST- EYFP (panel F) show the chromophore photobleaching in the presence and absence of sodium azide. These results are similar to those of GST-EGFP (Figure 3B) where CALI of GST activity is inhibited in the presence of azide yet the bleaching of the chromophore /fluorophore is relatively unaffected.
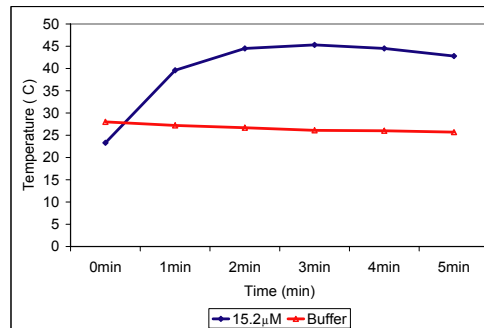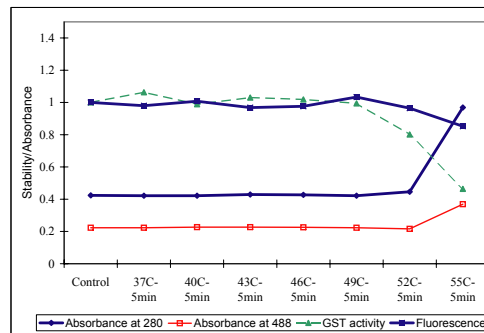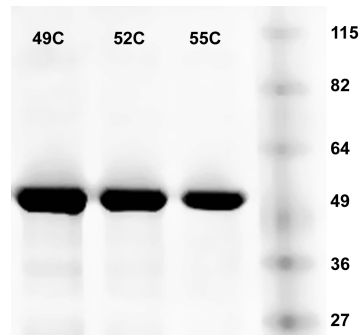
Figure S4.6 CALI is not due to laser heating-induced thermal denaturation of GST.
(A) Laser illumination of 15.2 µM of EGFP-GST increases the sample temperature (blue diamonds) but not of buffer alone (red triangles). (B) EGFP- GST activity (triangles), as well as the chromophore (empty squares) and the fluorophore (full squares) are thermally stable up to 50 C. (C) SDS PAGE analysis of EGFP-GST shows no crosslinking or degradation products after incubating EGFP-GST at different temperatures, 49 C, 52 C and 55 C for 5 min demonstrating that molecular integrity of EGFP-GST is retained after laser illumination.

4.7 REFERENCES

1. Rajfur Z, Roy P, Otey C, Romer L, and Jacobson K. (2002). Dissecting the link between stress fibres and focal adhesions by CALI with EGFP fusion proteins. *Nat Cell Biol* 4(4): p. 286-93

2. Vitriol EA, Uetrecht AC, Shen F, Jacobson K, and Bear JE. (2007). Enhanced EGFP-chromophore-assisted laser inactivation using deficient cells rescued with functional EGFP-fusion proteins. *Proc Natl Acad Sci U S A* 104(16): p. 6702-7

3. Jacobson K, Rajfur Z, Vitriol E, and Hahn K. (2008). Chromophore-assisted laser inactivation in cell biology. *Trends Cell Biol* 18(9): p. 443-50

4. Jay DG. (1988). Selective destruction of protein function by chromophore-assisted laser inactivation. *Proc Natl Acad Sci U S A* 85(15): p. 5454-8

5. Linden KG, Liao JC, and Jay DG. (1992). Spatial specificity of chromophore assisted laser inactivation of protein function. *Biophys J* 61(4): p. 956-62

6. Liao JC, Roider J, and Jay DG. (1994). Chromophore-assisted laser inactivation of proteins is mediated by the photogeneration of free radicals. *Proc Natl Acad Sci U S A* 91(7): p. 2659-63

7. Marek KW and Davis GW. (2002). Transgenically encoded protein photoinactivation (FlAsH-FALI): acute inactivation of synaptotagmin I. *Neuron* 36(5): p. 805-13

8. Tour O, Meijer RM, Zacharias DA, Adams SR, and Tsien RY. (2003). Genetically targeted chromophore-assisted light inactivation. *Nat Biotechnol* 21(12): p. 1505-8

9. Marks KM, Braun PD, and Nolan GP. (2004). A general approach for chemical labeling and rapid, spatially controlled protein inactivation. *Proc Natl Acad Sci U S A* 101(27): p. 9982-7

10. Surrey T, Elowitz MB, Wolf PE, Yang F, Nedelec F, Shokat K, and Leibler S. (1998). Chromophore-assisted light inactivation and self-organization of microtubules and motors. *Proc Natl Acad Sci U S A* 95(8): p. 4293-8

11. Mannervik B and Danielson UH. (1988). Glutathione transferases--structure and catalytic activity. *CRC Crit Rev Biochem* 23(3): p. 283-337

12. Holmuhamedov EL, Jovanovic S, Dzeja PP, Jovanovic A, and Terzic A. (1998). Mitochondrial ATP-sensitive K+ channels modulate cardiac mitochondrial function. *Am J Physiol* 275(5 Pt 2): p. H1567-76

13. Davies MJ. (2003). Singlet oxygen-mediated damage to proteins and its consequences. *Biochem Biophys Res Commun* 305(3): p. 761-70

14. Lepock JR, Thompson JE, and Kruuv J. (1978). Photoinduced crosslinking of membrane proteins by fluorescein isothiocyanate. *Biochem Biophys Res Commun* 85: p. 344-350

15. Yan P, Xiong Y, Chen B, Negash S, Squier TC, and Mayer MU. (2006). Fluorophore-assisted light inactivation of calmodulin involves singlet-oxygen mediated cross-linking and methionine oxidation. *Biochemistry* 45(15): p. 4736-48

16. Greenbaum L, Rothmann C, Lavie R, and Malik Z. (2000). Green fluorescent protein photobleaching: a model for protein damage by endogenous and exogenous singlet oxygen. *Biol Chem* 381(12): p. 1251-8

17. Jimenez-Banzo A, Nonell S, Hofkens J, and Flors C. (2008). Singlet oxygen photosensitization by EGFP and its chromophore HBDI. *Biophys J* 94(1): p. 168-72

18. Shaner NC, Campbell RE, Steinbach PA, Giepmans BN, Palmer AE, and Tsien RY. (2004). Improved monomeric red, orange and yellow fluorescent proteins derived from Discosoma sp. red fluorescent protein. *Nat Biotechnol* 22(12): p. 1567-72

19. Lee J, Yu P, Xiao X, and Kodadek T. (2008). A general system for evaluating the efficiency of chromophore-assisted light inactivation (CALI) of proteins reveals Ru(II) tris-bipyridyl as an unusually efficient "warhead". *Mol Biosyst* 4(1): p. 59-65

CHAPTER 5

Use of microfabrication to measure local cell-substrate adhesion:
An FET *(Field Effect Transistor)* cell adhesion sensor [1]

5.1 SUMMARY

The regulation of cell substratum adhesion is central to cell migration but there is no real measure of the strengths of local adhesion bonds to the substratum at different points under the cell. We are testing the use of micron scale Bio-Field Effect Transistors (BioFET) to sense the presence of cell adhesions under individual migrating cells. Feasibility tests have begun with charged beads and extracellular matrix proteins. Charges from the bead or ECM protein coating juxtaposed to the BioFET gate will modulate the source to drain current. In live cell adhesion experiments, the attachment of the cell to the gate produces a significant signal change that can be partially restored using Trypsin/EDTA to detach the cells. The signal change is based on the charge density of the cell surface and its proximity to the gate interface. Further studies will establish the feasibility of this method to detect local cell adhesion followed by the use of the technique as a basis to estimate adhesion forces using spatially resolved mechanical methods provided by, for example, AFM.

5.2 INTRODUCTION

The regulation of cell substratum adhesion is central to cell migration. A textbook paradigm for cell migration, based on fibroblasts and epithelial cells, is that a cycle exists whereby first cells make adhesions at their leading edge, which forms a base for internal contractile forces to pull up the trailing. The latter process requires that cells break adhesions at their trailing edge by mechanically pulling them up and/or enzymatically releasing them (1). Adhesions in these cell types include focal adhesions and their precursors, about which much is known (2) and close adhesions about which far less is known although these adhesions are prevalent in fast moving cells (3). Conventional wisdom is that focal adhesions form much stronger bonds to the substrate than do close contacts. Although much is being learned about the regulation and function of focal adhesions in fibroblasts (1, 4, 5), virtually nothing is known about the strength of individual adhesions to the substrate. Yet the strength of adhesions will dictate how efficiently internal contractile forces can be delivered to the substrate to generate tractions which serve to move the cell and/or remodel the surrounding extracellular matrix. Thus, knowledge of the strengths of adhesions will play a key role in our understanding of how cells migrate. Indeed, such knowledge will be important in generating complete understanding of the metastatic phenotype in which benign tumor cells lose positional control and migrate to distal sites to seed new tumors.

Various methods have been developed to measure relative adhesion of cells to substrates. These include mechanical methods including centrifugal force (6) or fluid flow (7) to detach cells from their substrates. Some instrumentally sophisticated technologies for

cell-based assays have emerged including optophoresis-based cell analysis in an optical field (8), acoustic field-based detection (9), optical biosensors (10), piezoelectric approaches such as Quartz Crystal Microbalance (QCM) (11), and electrical detection based on cell–substrate impedance measurements, such as ECIS or RT-CES systems (12, 13, 14). These techniques are either based on cell population averages or individual cells as units with no subcellular resolution of adhesion strength.

Thus, a barrier to cell migration investigations is that there is no real measure of local adhesion strength. To address this void in our knowledge, we collaborated with Professor Veena Misra at North Carolina State University. In this Chapter, we report our development of individually addressable open gate field effect transistors that can sense the presence of adhesive regions under single cells attached to the substrate, based on a chemical ion sensor pioneered by Dr. Misra (15). The concept of the device is similar to the BioFET pioneered by Fromherz lab, which has been used for detection of neuron action potentials (16).

5.3 MATERIALS & METHODS

5.3.1 Cells, Staining and Microscopy

NIH 3T3 cells and NBT-II cells were acquired from the ATCC (Manassas, VA). NIH 3T3 cells and NBT-II cells was maintained in high glucose DMEM and DMEM/F-12 medium (Gibco, Grand Island, NY) respectively; both medium contain 10% FBS, 100 units/ml penicillin and 100 µg/ml streptomycin.

The EGFP-Paxillin-β was generated by subcloning DNA fragments expressing wild-type paxillin and wild type vinculin into a pEGFP-C vector (Clontech, Mountain View, CA). NBT-II cells were transfected using the Lipofectamine Plus transfection reagent (Invitrogen, Carlsbad, CA) according to the manufacturer's protocol.

For immuno-staining, NBTII cells were fixed by using paraformaldehyde solution [4 % (w/v) in PBS, pH 7.4] for 20 minutes at 25°C. Cells were then permeabilized with PBS containing 0.05 % Triton-X-100 for 5 minutes at 25°C. Fluorescence labeling was carried out by treating with primary antibodies, washing with medium and then treating with fluorescent secondary antibodies followed by washing.

Epi-fluoresence imaging was carried out on a dual-channel Olympus IX81 inverted microscope equipped with a 60×, oil immersion, 1.45 NA objective. Interference Reflection Microscopy (IRM) imaging was performed using a 100×, oil immersion, 1.65 NA objective. Images were captured using an air-cooled SensiCam QE CCD camera (Cooke Corp., Romulus, MI) driven by Metamorph (Molecular Devices/Meta Imaging, Downingtown, PA).

5.3.2 Mask design

Fabrication of the 3D structure on a silicon wafer includes doping, forming an insulator level SiO2, coating metal for contact, and finally covering the insulator on the top. We used five mask layers (in the MoleFlash mask set), which are: (i) Zero, (ii) Active, (iii) Contact, (iv) Metal, and (v) Glass. The Zero level is used for making lithography alignments at the wafer level. Each level after that is primarily aligned to the preceding level. There are

secondary alignment marks to align to any of the previous levels. Dr. Smita Sarkar, our collaborator in Dr. Misra's lab, designed this mask, and I participated in the design.

5.3.3 FET fabrication: Process Flow

An overview of the processing steps involved in each of the mask levels of the MoleFlash mask set is provided here, and illustrated in figure 5.1.

1. Zero Layer:

Lithography alignment marks are made at the wafer level by etching them into Si. The sequence of steps in this layer involved, starting from blanket Si (100) n-type(phosphorous-doped) polished wafers, is: (i) JTBaker wafer cleaning. (ii) photolithography to pattern the alignment marks (pre-coat hard bake, photoresist spin-coat, pre-exposure soft bake, exposure, develop, and post-develop hard bake). (iii) "de-scum" using plasma asher, a type of cleaning, to improve resist edge profile. (iv) wet etch Zero layer Si using poly etch. (v) strip photoresist.

2. Active Layer:

The P+ source-drain regions are defined by ion implantation of boron atoms using patterned wet oxide layer as mask. The sequence of steps is: (i) JTBaker clean. (ii) wet oxide (~ 100 nm) growth for ion implant mask. (iii) photolithography to pattern oxide as mask for ion implantation including wafer backside photoresist coat. (iv) descum. (iv) wet oxide etch using buffered oxide etch (BOE) to open up source drain regions. (v) strip photoresist. (vi)

JTBaker clean. (vii) ion (boron, or phosphorus) implantation. (viii) wet oxide etch to completely remove mask oxide layer (both front and back).

3. Contact Layer:

Isolation (field) oxide is grown and gate region and source-drain regions are opened up by patterning the oxide using the contact layer mask. The thermal oxidation step also serves as an implant anneal to activate the source-drain dopants. The sequence of steps is: (i) JTBaker wafer cleaning. (ii) field (wet) oxide growth. (iii) photolithography. (iv) descum. (v) wet oxide etch to open up gate region and source-drain regions. (vi) strip photoresist.

4. Metal Layer:

Metal contacts to source-drain regions are formed by lift-off processing of the sputtered metal. The metal typically used is tungsten (W). The sequence of steps is: (i) JTBaker wafer cleaning. (ii) photolithography for metal lift-off. (iii) descum. (iv) source-drain remnant oxide etch (BOE). (v) back-door etch using 1% hydrofluoric acid (HF). (vi) metal deposition (W sputtering or aluminum/titanium evaporation). (vii) lift-off processing.

5. Glass Layer:

Low temperature oxide (LTO) is deposited as passivation layer using low pressure chemical vapor deposition (LPCVD) process, and holes to gate region and end of the metal lines to source-drain regions by patterning the oxide using the contact layer mask. The sequence of steps is: (i) LTO (~ 400 nm) deposition. (ii) photolithography. (iii) descum. (iv) wet oxide etch to open up the holes to gate region and metal contact pads. (v) resist strip.
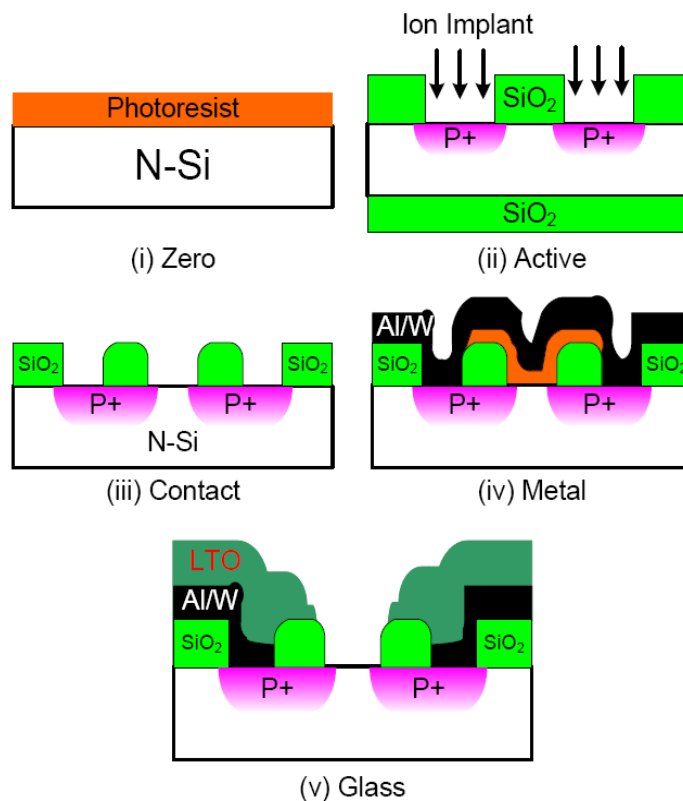
Figure 5.1. Schematic figure for fabrication of 5 layers. FET process flow (MoleFlash mask levels): cross-sectional view of FET active area. The figure corresponding for each level shows the critical step at that level. The final cross-sectional view of the FET device is shown in (v). (reprinted with permission from 15).

5.3.4 Electrical analyses

The electrical analyses were performed using a CHI 600 electrochemical analyzer and an HP 4155B semiconductor parameter analyzer. A silver wire was used as the counter/reference electrode. PBS (PH 7.4) (Gibco) and DMEM (Gibco) are used as electrolytes in the measurement.

5.4 RESULTS

5.4.1 Fabrication of BioFET.

The fabrication of our BioFET was processed according to the steps described in methods 5.3.2 and 5.3.3. Figure 5.2 shows the structure of our final fabricated BioFETs. Each BioFET contains five layers, as described above. Figure 5.2 left panel is an EM images of the device. The parameters for each structure are marked and indicated in the figure. The upper panel on the right is a 10X interference reflection microscope image showing the whole FET device; the lower panel is a 40X interference reflection microscope image focusing on one side of the device, including active layer, contact layer, metal layer and the 5μm gate region.

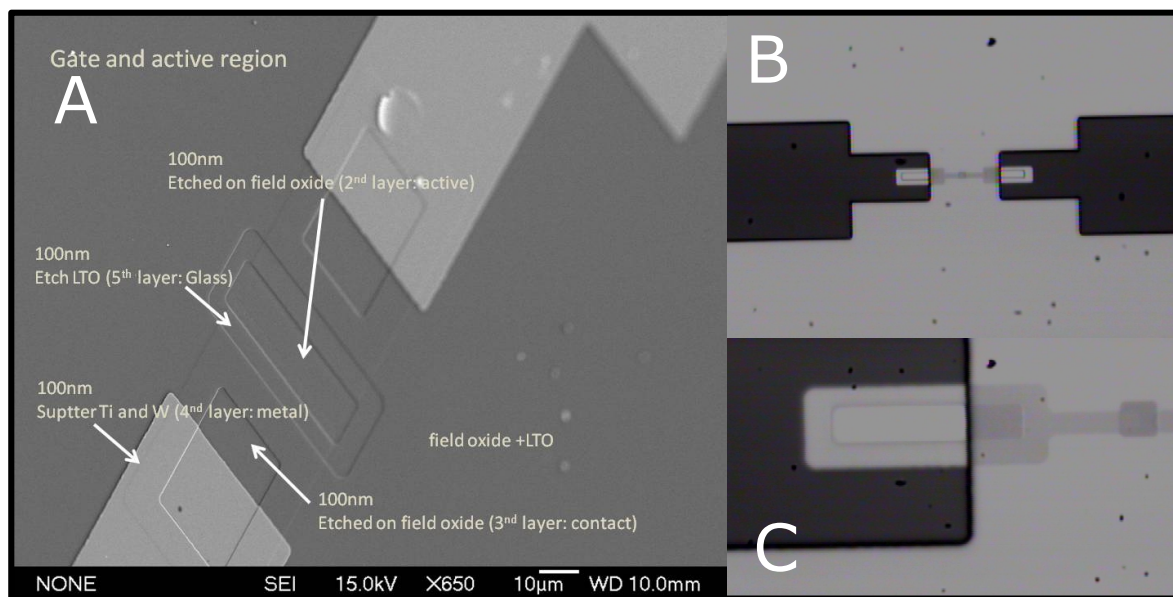**Figure 5.2. Fabrication and structure of our BioFETs.** In fabrication, each bioFET contains five layers, which are shown in SEM images (panel A). The device in panel A has a gate size of 10μm x 50 μm. Panel B and C are 10x and 40x interference reflection microscopy images showing the 5μm gate FET device. In the images, the grayscale reflects thickness of each layer and different material in each layer.

5.4.2 Performance testing of the BioFETs

After the fabrication of BioFETs, we tested their electrical behavior and compared it with a conventional solid state FET. This step is essential mainly because of following reasons:

a) The gate of a normal solid state FET is usually covered with metal and the voltage is applied directly to the gate. However, in our open-gated-BioFET, there is no metal on the gate. The gate voltage is applied from the silver wire, which is immersed in the electrolyte on the top of the gate such that the silver wire has no direct contact to the gate.

b) All of the cell experiments require cell culture medium which is the gate electrolyte in our BioFET experiments. Thus, understanding of device electrical behavior under these buffers is important.

In order to confirm whether our fabricated BioFETs behave similar to a normal FET, we tested the Id-Vd (current from source to drain (Id) against the voltage applied between source and drain (Vd) , under a specified gate voltage) characteristic curves of our open gate FET and compared them to the solid state FET in a similar range of gate voltages, as shown in figure 5.3. We found they have similar Id-Vd curve patterns but fabricated BioFETs have lower source to drain currents.
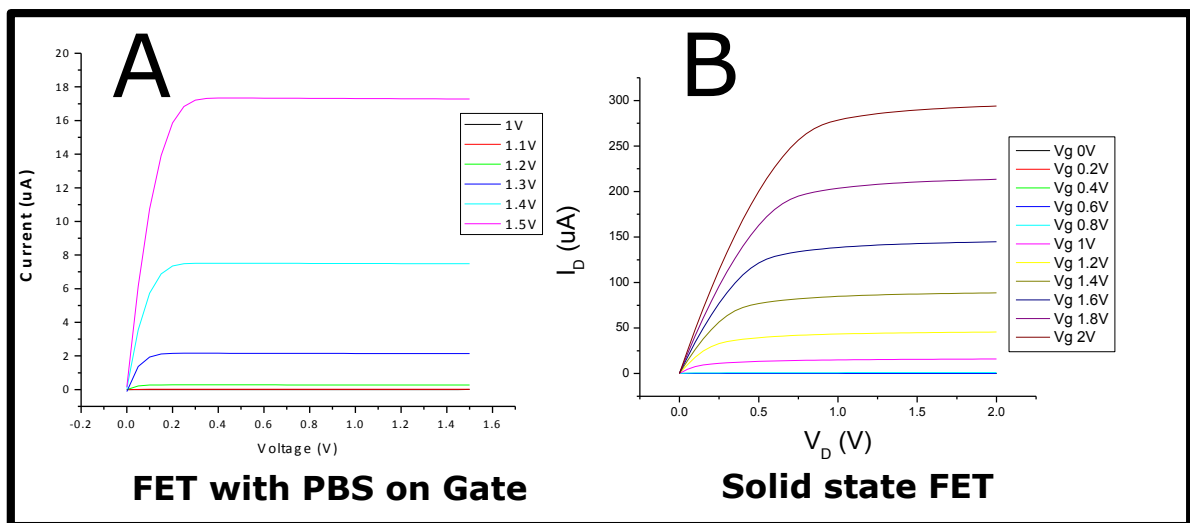
Figure 5.3. Comparison between solid state FET and our BioFET. Standard FETs are solid state devices, which have direct metal-gate contact and can only be used in none conductive environments such as vacuum or air but not in electrolyte solutions. Our bioFETs have a different gate structure than solid state FETs. Cell studies require aqueous as environment, here, gate oxide isolate the FET gate region from the electrolyte solution. A) Id-Vd curve of our 5μm gate BioFET in PBS (ph7.4). Id-Vd curve patterns of our fabricated BioFETs shows typical FET characteristics, in the range of 1.1v-1.5V; an increase of 100mV induced more than a 150% I_d current increase. B) Id-Vg curve of a standard solid state FET.

5.4.3 Charged beads on FET devices

In order to study the effect of charge on the bioFET characteristics, we first applied Dynal beads M-280 Streptavidin (Invitrogen) to the device as a cell mimic. Dynal beads are small in diameter (2.8μm) while containing strong negative charges (-50mV) on their surface providing a similar negative surface potential cells. After adding charged beads to the gate, the signal from device changed by more than 60%, indicating the potential of this device for live cell measurements.

5.4.4 3T3 cell adhesion detected by BioFET

Next, we tested whether cell adhesion can be detected by BioFETs. 10^4 3T3 cells were plated on the BioFET gate ($0.5cm^2$), and cultured for 24 hours in a 37-degree incubator. The source to drain current (Id) was tested under different gate voltage to get the Id-Vg curve. Id-Vg curves were measured before and after cell attachment. A schematically figure for the device and measurement setup is shown in Figure 5.4A. Figure 5.4B is the IRM image indicating the structure of the device. Figure 5.4C shows the 3T3 cells labeled with cytoskeleton marker showing that one cell is on the top of our BioFET gate. Figure 5.4D is the overlay of the cell and BioFET. (The fixation and Rhodamine-phalloidin labeling for actin-cytoskeleton was done after BioFET measurement). Figure 5.4E shows the Id-Vg curve before and after cell attachment on an nFET (negative channel Field Effect Transistor). A clear difference can be observed. Figure 5.4F shows the Id-Vg curve before and after cell attachment in same conditions but on a pFET (possitive channel Field Effect Transistor). The nFET uses electrons as the charge carrier in the channel; thus, the negative charge on the cell surface results in a signal decrease (shift downwards of Id-Vg). The pFET uses holes as the charge carrier in the channel; thus, the negative charge on the cell surface results in a signal increase (shift upwards of Id-Vg curve). Comparing with previous panel, we can see the pFET is less sensitive than the nFET in detecting cell attachment. Figure 5.4G shows source to drain current (Id) against time after the 3T3 cells were cultured overnight. Then PBS w/o Mg2+ and Ca2+ was used to wash 3T3 cells and when cells were maintained at 37C in PBS for 30mins, a significant Id signal decrease was observed, which indicates weakening of cell-substrate adhesions. Use of trypsin treatment for 30mins further decreased the signal to a lower state, which indicates nearly total detachment of the cells.
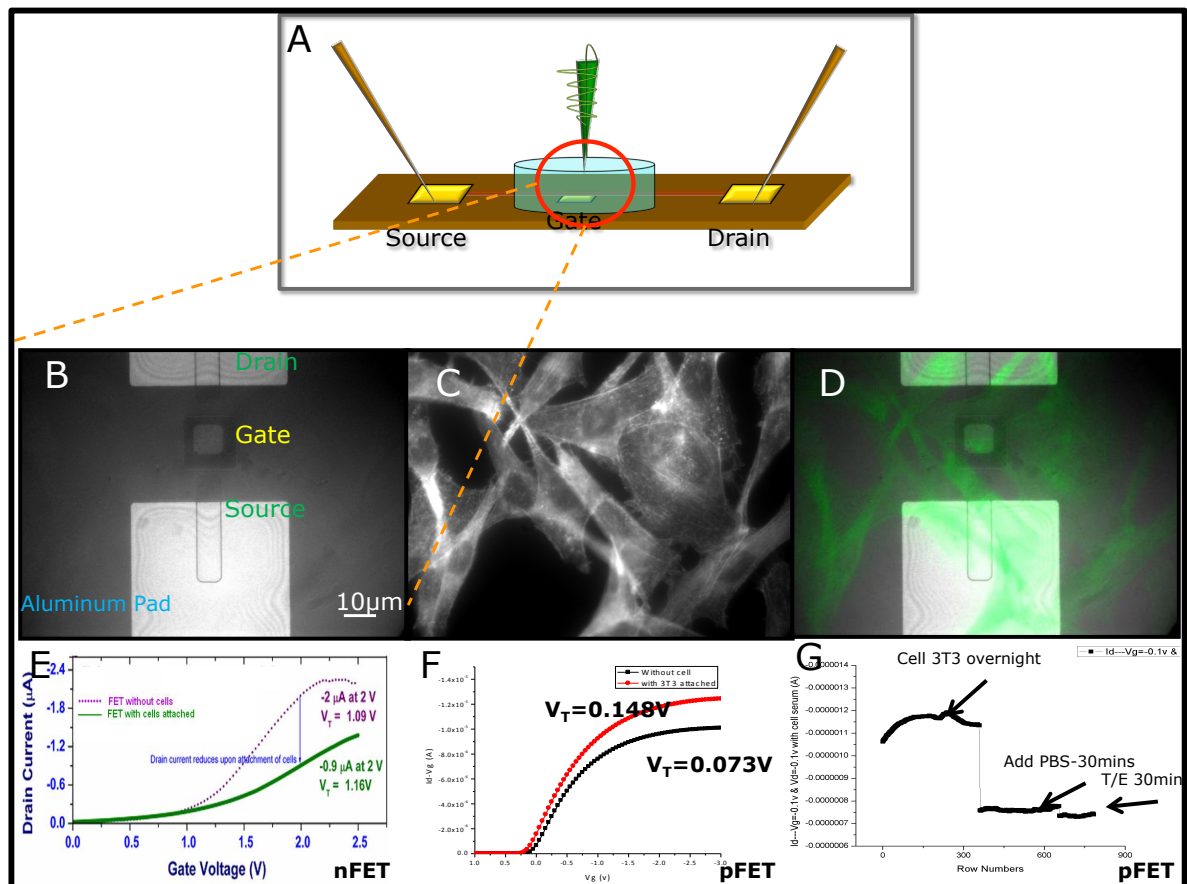
Figure 5.4 3T3 cell adhesion can be detected by BioFET. Panel A is the schematic figure for our device and setup of experiment. Panel B is the IRM image showing the structure of the BioFET including: gate, source and drain structures which are marked in the panel correspondingly. Panel C is the EPI fluorescent image showing Rhodamine-phalloidin labeled actin cytoskeleton of 3T3 cells. Panel D is the overlay of panel B and C showing 3T3 cells attachment on the gate. Panel E and F show the Id-Vg curves before and after cell adhesion for n-FET and p-FET respectively. Panel G measures the Id current against time, first Id values was measured during cells in culture; next Id was measured after cell had been washed with PBS for 3 times and kept in PBS for 30mins; lastly, when cells were treated with trypsin for 30mins and Id was again measured.

5.5 DISCUSSION AND FUTURE DIRECTIONS

In the above study, we demonstrated that both charged beads and cell adhesion can be detected by our BioFET. However, more development is required as discussed below.

One of the barriers is the complexity of components in culture media, especially, various proteins in the serum. During cell culture, proteins in the serum nonspecifically absorb to the FET gate, producing a time-dependent signal change (16). This prohibits long time study of cell adhesion/migration behavior using this device. In our tests, we found use DMEM without serum can reduce the protein absorption. Thus, we used BioFETs precoated with fibronectin (5μg/ml) and DMEM w/o serum in a later studies of cell adhesion. Serum free medium reduced the nonspecific protein absorption, while the fibronectin coating induced a quick cell spreading which also minimizes the attachment time (data not shown).

Secondly, cleaning and reuse of the device resulted in a changed surface condition and unstable signals; moreover, the electrical characteristics differ from device to device. Therefore, at this juncture, devices really cannot be reused reliably.

To obtain sub-cellular adhesion resolution, we developed individually addressable multi-gate BioFET devices with different gate sizes (Figure 5.5). This device has an array of gates that can be measured individually. Therefore we would be able to measure subcellular adhesion via BioFET signal changes in each device that is under a cell.
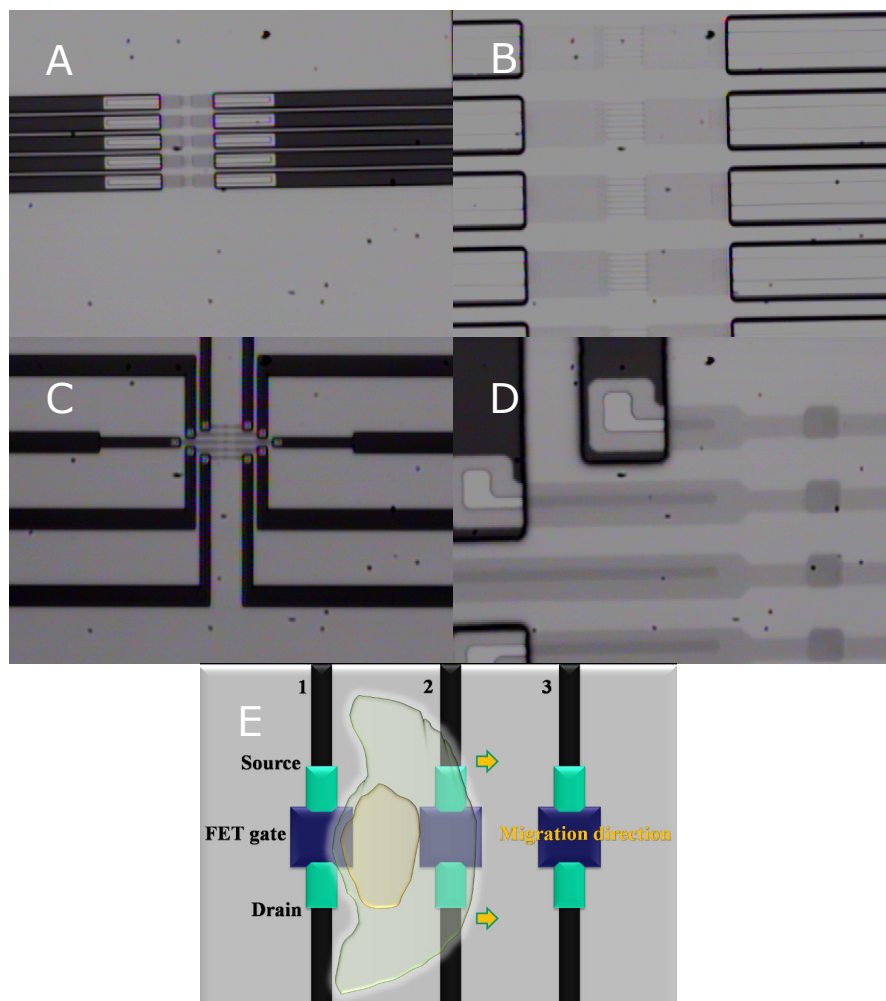
Figure 5.5 Multigate BioFET. Each gate is individually addressable. The device in upper panel A and B is the same device that has multiple 2μm width gate channels imaged at 10x and 40x using interference reflection microscopy. The device in lower panel C and D is another device that has a gate size of 5μm imaged at 10x and 40x using interference reflection microscopy. Panel E is a schematic figure showing a cell migrating on a 20μm multigate BioFET, so that adhesions in different subcellular regions can be measured.

Thirdly, our BioFET measures basically proximity and charge of the ventral surface of the cell to the substratum. The longer-term goal is to translate this proximity into a measure of adhesion strength (Figure 5.6B). The way we proposed is to employ atomic force microscopy (AFM) in manner similar what has been done when the AFM is employed as a single molecule force spectrometer (17, 18). The basic idea will be to coat the AFM

cantilever with receptors (integrins) such as would be found on the cell surface and employ cantilevers with areas similar to what is in contact with the FET. The cantilever would be lowered to the point where the FET signal is modulated to a value similar to what is measured in the cell experiment. The cantilever would then be withdrawn to the point where contact is broken whereupon the force would suddenly decrease. The force-extension curve would then give a measure of adhesion strength at that rate of cantilever withdrawal.

5.6 REFERENCES

1. Ridley, A. J., M. A. Schwartz, et al. (2003). Cell migration: integrating signals from front to back. *Science* 302(5651): 1704-9.

2. Zaidel-Bar, R., S. Itzkovitz, et al. (2007). Functional atlas of the integrin adhesome. *Nat Cell Biol* 9(8): 858-67.

3. Lee, J. and K. Jacobson (1997). The composition and dynamics of cell-substratum adhesions in locomoting fish keratocytes. *J Cell Sci* 110 (Pt 22): 2833-44.

4. Burridge, K. and M. Chrzanowska-Wodnicka (1996). Focal adhesions, contractility, and signaling. *Annu Rev Cell Dev Biol* 12: 463-518.

5. Juliano, R. L. (2002). Signal transduction by cell adhesion receptors and the cytoskeleton: functions of integrins, cadherins, selectins, and immunoglobulin-superfamily members. *Annu Rev Pharmacol Toxicol* 42: 283-323.

6. 6 Channavajjala, L. S., A. Eidsath, et al. (1997). A simple method for measurement of cell- substrate attachment forces: application to HIV-1 Tat. *J Cell Sci* 110 (Pt 2): 249-56.

7. Decave, E., D. Garrivier, et al. (2002). Shear flow-induced detachment kinetics of Dictyostelium discoideum cells from solid substrate. *Biophys J* 82(5): 2383-95.

8. Soo, H., J. Kohrumel, et al. (2003). Detection of cancer using near-infrared moving optical gradient fields. *Annual Meeting of American Society of Clinical Oncology* 2003(Chicago, IL.).

9. Cooper, M. A., F. N. Dultsev, et al. (2001). Direct and sensitive detection of a human virus by rupture event scanning. *Nat Biotechnol* 19(9): 833-7.

10. Biran, I., D. M. Rissin, et al. (2003). Optical imaging fiber-based live bacterial cell array biosensor. *Anal Biochem* 315(1): 106-13.

11. Wegener, J., A. Janshoff, et al. (1999). Cell adhesion monitoring using a quartz crystal microbalance: comparative analysis of different mammalian cell lines. *Eur Biophys J* 28(1): 26-37.

12. Giaever, I. and C. R. Keese (1984). Monitoring fibroblast behavior in tissue culture with an applied electric field. *Proc Natl Acad Sci U S A* 81(12): 3761-4.

13. Smith, T. J., H. S. Wang, et al. (1994). Prostaglandin E2 elicits a morphological change in cultured orbital fibroblasts from patients with Graves ophthalmopathy. *Proc Natl Acad Sci U S A* 91(11): 5094-8.

14. Yu, N., J. M. Atienza, et al. (2006). Real-time monitoring of morphological changes in living cells by electronic cell sensor arrays: an approach to study G protein-coupled receptors. *Anal Chem* 78(1): 35-43.

15. Gowda, S., Q. Mathur, et al. (2006). Hybrid Silicon/Molecular FETs: A Study of the Interaction of Redox-Active Molecules With Silicon MOSFETs. *IEEE Transactions on Nanotechnology* 5(3): 258-264.

16. Fromherz, P., A. Offenhausser, et al. (1991). A Neuron-Silicon Junction: A Retzius Cell of the Leech on an Insulated-Gate Field-Effect Transistor. *Science* 252: 1290-1293.

17. Clausen-Schaumann, H., M. Seitz, et al. (2000). Force spectroscopy with single bio-molecules. *Curr Opin Chem Biol* 4(5): 524-30.

18. Rabbi, M. and P. E. Marszalek (2008). Probing polysaccharide and protein mechanics by atomic force microscopy. *Single-Molecule Techniques A Laboratory Manual (Cold Spring Harbor Laboratory Press)*: 371-394.

CHAPTER 6

Conclusions and Outlook

In this dissertation, we report our study on Abl family inhibitor induced shape and migration changes in rat bladder tumor cells, a study on the mechanism of protein inactivation mediated by fluorescent protein CALI, and the progress towards a Field Effect Transistor based detector of local cell adhesion. Some of the work I participated in is not included in this thesis, such as a study on smurf1-mediated talin head ubiquitylation and cell migration (Huang C, Rajfur Z, Yousefi N, Chen Z, Jacobson K, Ginsberg MH. *Nat Cell Biol.* 2009,11(5):624-30), and an unpublished study on keratocyte traction force mapping.

In this conclusion, I would like to discuss a little bit more about fast migrating cells and the impact of our study on NBT-II cell migration, and then raise some potential future directions.

6.1 SURPRISING SIMILARITIES BETWEEN TWO FAST MIGRATING CELLS

In Chapter 3, we reported the formation of special "fan shape" (or "canoe shape") morphology and fast migration of Gleevec-treated NBT-II cells. The "fan shape" (or "canoe shape") was originally employed to describe the migration of keratocytes. What

are the similarities between Gleevec-treated NBT-II cells and keratocytes. Keratocytes are employed as a model system for the study of cell migration, because:

(i) They usually form a large and intact fan-shaped lamellipodium during migration, which facilitates investigations of lamellipodium structure and formation;

(ii) They usually move with nearly constant speed and direction. This characteristic makes them a versatile tool in the study of cytoskeletal dynamics and migration, including cell adhesion, cell traction force, actin polymerization / treadmilling, etc.

Keratocyte migration is distinct in that it is neither an amoeboid nor mesenchymal migration. It maintains its unique fan shape during migration, which is not seen in any other type of migrating cells (1-3). The transition between other cell migration phenotypes to a keratocyte phenotype has never been found (4). This is surprising considering that most of other migration types are actually switchable; for example, the switch between mesenchymal and amoeboid has been observed during the process of cancer cell metastasis (4,5).

One of the novelties in this thesis work is the discovery of fan-shaped migrating NBT-II cells after Gleevec-treatment, which, to our knowledge, is the first report of a non-keratocyte cell migrating with a consistent fan shape. As shown in Figure 6.1, Gleevec treated NBT-II cells (panel A) and fish keratocyte (panel B) have very similar fan shape during migration. Both cells form large and intact lamellipodium. Both cells are elongated perpendicular to the direction of migration (with aspect ratio close to 2*)

---

* the aspect ratio was defined in Chapter 3

(Figure 3.2A in Chapter 3); while control NBT-II cells or most of other types of migrating cells are mostly roundish or elongated along the direction of migration of the cell (aspect ratio close to or smaller than 1) (Figure 3.2A in Chapter 3). Phosphorylated myosin II patterns in fish keratocytes and canoe shape NBT-II cells are similar, shown in panel C and D, respectively. And panel F and G compares the traction pattern of canoe shape NBT-II (E) and keratocytes (F). Both the phosphorylated myosin II or traction pattern indicates similarity between Gleevec induced NBT-II cells and keratocytes.
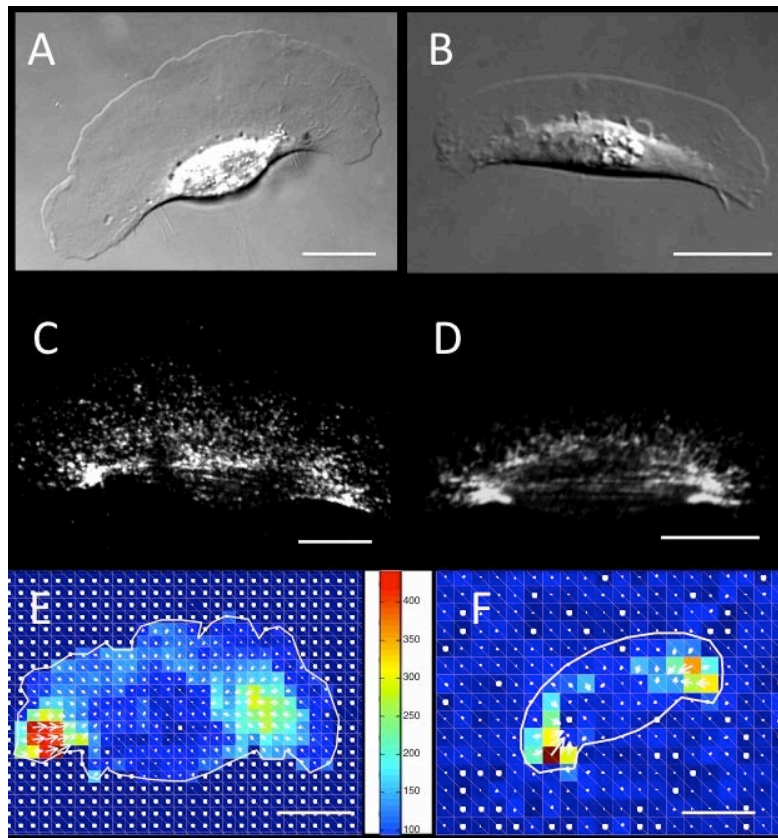

Figure 6.1 Comparison between fan-shape NBT-II cells and fish keratocytes
Panel A and B are DIC images for fan-shape NBT-II cells and keratocytes respectively. C and D show the antibody labeling of phosphorylated myosin II in fan-shaped NBT-II cells and keratocytes, respectively. E and F are elastic substrate traction mapping of fan-shaped NBT-II and keratocytes, respectively. Colors from blue to red indicate relative cell traction stress (unit, Pa). Scale bars are 20μm.

6.2 FUTURE DIRECTIONS

Combining our knowledge in fan-shaped NBT-II cells and fish keratocytes, we suggest following four points for future research:

1. The balance between cell traction and cell adhesion in fast migrating cells.

Cell migration speed is based on a delicate balance between the cell traction force and cell adhesion (rather than the absolute magnitude of either). Take fish epidermal keratocytes as an example: on one hand, cells on low adhesive substrate are usually smaller in size and aspect ratio, and migrate slower than on medium adhesive substrate; on the other hand, cells on high adhesive substrate actually don't migrate faster than on medium substrate, but migrate slower due to insufficient retraction. Treatment of calyculinA to cells on high adhesive substrates can activate myosin contraction and increase cell migration speed (6). In Gleevec-treated NBT-II cells, we found there is an increase in integrin-mediated adhesion coupled with increases in the size and number of discrete adhesions. Moreover, Gleevec-treated cells have greater RhoA activity which, via myosin activation, led to an increase in the magnitude of total traction force applied to the substrate. The balance between adhesion strength and cell traction in part determines the migration status of the cell and we suggest this is an important parameter in the study of all types of cell migration.

2. Nascent adhesions at leading edge of fast migrating cells.

In fish keratocytes, a band of grey area at the leading edge of the lamellipodium can be observed in interference reflection microscopy (IRM). These regions are defined

132

as close contacts (Figure 2.3A in Chapter 2). Those close contact areas at the rim of leading edge were found enriched in β1-integrin and talin, with paxillin and FAK but without vinculin (1). Close contacts are mediated by integrins. Forward movement of keratocyte lamellae can be halted by adding RGD peptide or an anti-integrin mAb.

In Gleevec-treated NBT-II cells, TIRFM image of EGFP-paxillin show a rim of punctate adhesions at the leading margin of the fan-shaped lamellipodium as a common feature (Figure 3.5E,F in Chapter 3). The size distribution of punctate adhesions in Gleevec-treated NBTII cells had a peak at ~350nm in diameter, and the average area of punctate was about $0.1\mu m^2$. These punctate adhesions turned over very rapidly with an average lifetime of ~70s. Our study shows those punctate adhesions contain paxillin but no vinculin. Similar to keratocyte migration, lamellar protrusion in Gleevec-treated NBT-II cells can be halted by RGD peptide or anti-integrin mAb.

In sum, punctate adhesions and close contacts both locate to the leading edge of the lamellipodium. They both contain integrins,both are distributed in a band shape and both exhibit fast turnover. Since it is difficult to study close adhesion in fish keratocytes due to multiple reasons (will be discussed later), the study of nascent adhesions in NBT-II cells could be very revealing.

3. Microtubule function in cell migration.

In keratocytes, microtubules (MT) and intermediate filaments do not penetrate the thin, actin-rich lamellipodium but are confined to the perinuclear region. Depolymerization of MT in keratocytes does not significantly affect their migration (Figure 6.2A).

In contrast, microtubules in Gleevec treated NBT-II cells can penetrate into lamellipodium, and actually play an important role in both maintaining cell nuclear-shape and lamellipodium (Figure 6.2B) since depolymerization of MT with Nocodazole in NBT-II cells results in reduced lamellipodium size, less migration speed and persistence, and relaxation of cell nucleus. Thus, investigation of the role of MTs in fan-shaped NBT-II is a worth future direction.
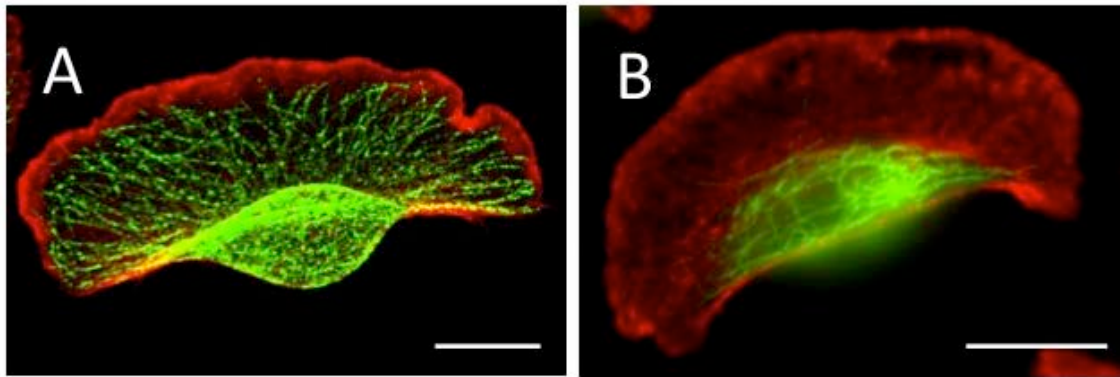

Figure 6.2 Actin and microtubule cytoskeleton of gleevec treated fan-shape NBT-II cells and fish keratocytes. Confocal fluorescent images of the f-actin (Rhodamine-phalloidin, Red) and microtubules (alpha-tubulin antibody, Green) in the fan shape NBT-II cell (A) and fish keratocyte (B). Scale bars are 20μm.

4. Technical advantages of NBT-II cells in comparison to keratocytes.

There are some well-known technical difficulties in conducting research with keratocytes:

(a) Keratocytes are terminally differentiated primary cells that must be freshly isolated. The yield is small, with only hundreds of cells harvested from one fish scale. This prevents keratocytes from being used in some biochemical analyses, which require a much larger numbers of cells.

(b) Keratocytes are difficult to transfect or microinject. Although electroporation has recently been used for keratocyte transfection (7), a very small proportion (less than 1%) expresses the target protein.

(c) Keratocyte itself is a very good model for cell migration research. However, the direct linkage between keratocyte migration and cancer cell migration is still unknown.

(d) Genetically encoded biosensors provide real-time spatial and temporal activity information for many regulatory signaling proteins/kinases in crawling cells (8,9). Although the application of these biosensors in this model would likely be very informative, no biosensors have been successfully used in migrating keratocytes.

The technical problems restrict the scope of keratocyte-based research, while NBT-II cells have none of those problems. NBT-II cells are rat bladder cancer cell line. They can be easily transfected and have good expression level of target proteins (We successfully expressed the Rho and Rac1 biosensor in NBT-II cells so that Rho-family biosensors can be employed to study migration of these cells.) NBT-II cells are easier to microinject than keratocytes. Lastly, NBT-II is a well-known migrating cancer cell line

(10) so that the observation of a special migration phenotype raises the question whether other cancer cells may undergo similar migration under certain circumstances.

6.3 REFERENCES

1.   J Lee, Ishihara A, Theriot JA, and Jacobson K. Principles of locomotion for simple-shaped cells. *Nature* 362(6416): p. 167-71, 1993.

2.   TM Svitkina, Verkhovsky AB, McQuade KM, and Borisy GG. Analysis of the actin-myosin II system in fish epidermal keratocytes: mechanism of cell body translocation. *J Cell Biol* 139(2): p. 397-415., 1997.

3.   K Keren, Yam PT, Kinkhabwala A, Mogilner A, and Theriot JA. Intracellular fluid flow in rapidly moving cells. *Nat Cell Biol* 11(10): p. 1219-24, 2009.

4.   Friedl, P. and K. Wolf (2010). "Plasticity of cell migration: a multiscale tuning model." *J Cell Biol* 188(1): 11-19.

5.   Pankova, K., D. Rosel, et al. (2010). "The molecular mechanisms of transition between mesenchymal and amoeboid invasiveness in tumor cells." *Cell Mol Life Sci* 67(1): 63-71.

6.   Barnhart, E. L., K. C. Lee, et al. (2011). "An adhesion-dependent switch between mechanisms that determine motile cell shape." *PLoS Biol* 9(5): e1001059.

7.   CA Wilson, Tsuchida MA, Allen GM, Barnhart EL, Applegate KT, Yam PT, Ji L, Keren K, Danuser G, and Theriot JA. Myosin II contributes to cell-scale actin network treadmilling through network disassembly. *Nature* 465(7296): p. 373-7, 2010.

8.   Machacek, M., L. Hodgson, et al. (2009). "Coordination of Rho GTPase activities during cell protrusion." *Nature* 461(7260): 99-103.

9.   Wu, Y. I., D. Frey, et al. (2009). "A genetically encoded photoactivatable Rac controls the motility of living cells." *Nature* 461(7260): 104-108.

10.   Huang C, Z Rajfur, C Borchers, MD Schaller, and K Jacobson (2003) *JNK phosphorylates paxillin and regulates cell migration.* Nature. 424(6945): p. 219-23.